Analysis and development of particle based heat transport models for use in nanoscale structures.

Anil Mathew Asokan

University of Leeds
School of Electronic and Electrical Engineering
September 2007

Submitted in accordance with the requirements for the degree of Doctor of Philosophy.

The candidate confirms that the work submitted is his own and that appropriate credit has been given where reference has been made to the work of others.

Acknowledgments

First and foremost, I would like to acknowledge the invaluable insight, advice, encouragement and general help from Dr. Robert Kelsall, without whom the work would not have been possible.

Support from other academic members of the Institute of Microwaves & Photonics has to be acknowledged; Dr. Leon Lever, Alex Valavanis and Toufik Sadi especially. My thanks extends to other members, too numerous to mention, who have listened to my ramblings, answered my questions and generally put up with me for the 4 years it has taken to complete this. My thanks to Dr. Greg Horler who helped to motivate me.

Thanks to all the people who have helped proof read my thesis and everything I have ever written especially Amber Dowell and Che Bishop. I have to thank my house mates Rich Sage and Andrew Kilner, for their programming help and technical support, without whom any little bit of sanity I have left would have been lost a long time ago.

The Monte Carlo element of this work was also aided greatly by the use of the freely-available Mersenne Twister library for generation of the required random numbers.

The Cannon Collins trust must be mentioned due to their monetary contribution to my fees and the University of Leeds for providing the rest.

Finally, I have to thank my family, who have been incredible in supporting me despite the oceans in between us.

Abstract

Thermal management is one of the main issues which must be overcome in order to maintain the continued reduction of feature sizes in silicon microelectronics. The new materials and device architectures which are used to achieve better performance have had a detrimental effect on thermal management due to higher thermal resistances and additional thermal interfaces. Current thermal models, based on diffusive continuum flow, are inaccurate at nanoscale dimensions and a model which considers the microscopic nature of heat generation and heat tansport must be used.

On the microscale, heat transport can be described by the Boltzmann transport equation for phonons. The complexity and quantity of the phonon anharmonic interactions make a direct numerical solution difficult without numerous approximations. The Monte Carlo technique has been established as an accurate approach to the modelling of charge transport in semiconductors and the application of this method to phonon transport is a logical choice.

There has been little reported work on Monte Carlo simulations of phonon transport. This thesis examines previous work on non-momentum conservation Monte Carlo simulations, exposing the shortcomings of this approach and attempting to rectify them with algorithmic changes as well as the use of relaxation times calculated using second and third order elastic constants. These changes result in an improvement of the equilibrium simulation as well as producing more realistic thermal gradients for both large and small temperature differences at steady state. The improved techniques are applied to nanowire geometries and found to provide the correct trends.

The work is extended further to produce a momentum conservation Monte Carlo simulation and used to simulate the anharmonic three-phonon processes (both absorption and emission type) for acoustic phonon modes in silicon. Phonon-phonon absorption events are performed by selecting a partner phonon from within the same real space cell that satisfies momentum and energy conservation. In previous derivations of analytical approximations for phonon lifetimes and thermal conductivities, it has been difficult to determine the relative contribution of Normal and Umklapp processes in phonon-phonon interactions; this information can be extracted directly from the Monte Carlo simulation. Some success is achieved with this method at low temperatures and it is shown that with higher computational power, this simulation could provide a very accurate model for heat transport.

Contents

List of Figures

List of Tables

List of symbols

BTE	Boltzmann Transport Equation
CPU	Central Processing Unit
LA	Longitudinal Acoustic
MC	Monte Carlo
MD	Molecular Dynamics
N-process	Normal process
TA	Transverse Acoustic
U-process	Umklapp process
κ	Thermal conductivity
ϵ	Classical deformation tensor
η	Second order deformation tensor
σ	Second rank stress tensor
Γ	Centre of the Brillouin zone
ω	Phonon frequency
τ	Phonon relaxation times
a	Annihilation operator
$a^\dagger$	Creation operator
c	Elastic constant
D	Density of states

e	Atomic polarisation
E	Energy
f	Distribution function
$\mathbf{G}$	Lattice vector
H	Hamiltionian
$\mathbf{M}$	Phonon transition matrix element
n	Phonon distribution
N	Phonon population
p	Polarisation of phonon branch
q	Wavevector
Q	Net heat flux
S	Scaling factor
t	Time
T	Temperature
u	Atomic displacement
v_g	Phonon group velocity
V	Volume
W	Elastic potential energy

Chapter 1

Introduction

Semiconductor device manufacture and its continuously increasing improvement in accordance with Moore's Law has brought about rapid technological advancement to modern society. State of the art integrated microchips can have tens of millions of transistors on an area the size of a postage stamp and transistor switching speeds are increasing. These two factors inevitably lead to challenges in thermal management.

1.1 Heating in semiconductor devices

Moore's law states that the most cost efficient number of transistors on an integrated circuit doubles every 24 months [12]. There has been a corresponding Moore's law for power dissipation in chips as shown in figure 1.1. Thermal management is one of the main obstacles in the continued reduction of feature size in microelectronics. The International Technology Roadmap for Semiconductors (ITRS) [13] states that this reduction has led to increased power dissipation, larger temperature cycles and increased thermal gradients, all of which reduce reliability. Heat generation has increased exponentially, to the current values of approximately 100 Watts per chip and should the trend continue, it will reach catastrophically high levels of dissipation in the next few years [14].

The continued quest to improve performance has led to the use of smaller devices with higher electric fields, as well as development of new technology like strained silicon with silicon germanium layers [15], silicon on insulator and the use of III-V materials in multilayer devices such as heterostructure field effect transistors [13]. These techniques and technologies are having detrimental effects on the thermal management in devices due to phonon confinement, boundary conditions and other such thermal effects.

Computer central processing units (CPUs) are a good example of the current trend in microprocessors, where a chip of only 1cm^2 dissipates about 60 Watts of heat and is cooled by a fan much larger than the chip itself. This has led to a large investment in cooling technology, with computer manufacturers looking at liquid cooling,[1] on-board refrigeration [18] and in extreme cases, liquid nitrogen cooling [19, 20]. Thermoelectric components are increasingly employed in integrated circuits for thermal monitoring [21]. Furthermore devices such as semiconductor lasers, which generate large amounts of heat [22], are finding increased use in optoelectronics.

1.2 Semiconductor device modelling

Semiconductor device modelling is standard industry practice. Simulation is required for many processes from very-large-scale integrated circuits (VLSI) design through to individual device design. The modelling techniques used range from simple circuit approximations to models that include a more realistic portrayal of the underlying physical processes. The latter are more suited to simulations of individual devices or structures, as is the focus of this work.

The classic approach to modelling charge transport in semiconductors uses the Boltzmann transport equation (BTE) [23]. The BTE describes the change in a distribution

---

[1] Liquids used in immersion cooling have traditionally been oils that are not specifically designed for this purpose such as motor oil or other silicon lubricants which have high thermal and low electrical conductivity [16]. Recently, with the increased demand for coolants, more specialised liquids are being manufactured such as Fluorinert [17].

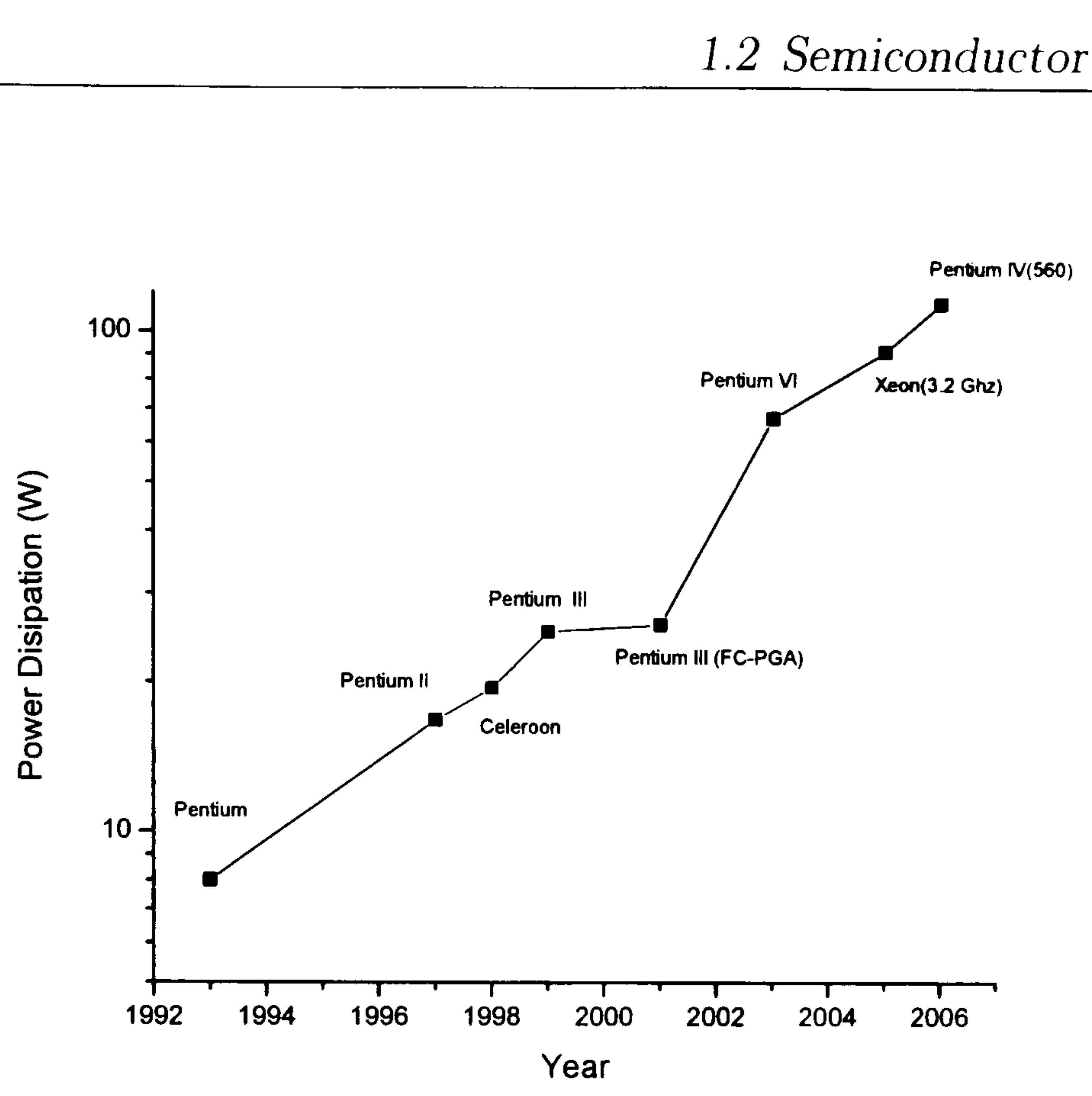

Figure 1.1: The increasing power dissipation in modern CPUs [1].

function of the charged particle with time, and thus can describe accurately both equilibrium and non-equilibrium effects in a semiconductor structure.

Heating effects have steadily become a more important part of device and charge transport simulation [24,25]. The isothermal approximation, where the temperature of the device is a constant throughout the material, is becoming increasingly erroneous in modern semiconductor devices. Thermally self-consistent solutions are increasingly being used for the change in distribution caused by the thermal state of the lattice [26]. These models have traditionally used heat diffusion to describe the transport of heat. Such heat transport models are applicable to devices where there is an assumption of local thermal equilibrium.

As semiconductor structures become more complex, a more accurate method for describing electrothermal effects will be required. One example is in high density nanoelectronics, where the length scales of the device components are in the region of the phonon mean free path. This means that a homogeneous phonon distribution can no longer be assumed, affecting the electron transport characteristics. In high power devices the heat generated can lead to critical failure or hot spots which cannot easily be predicted with traditional methods. There is an increased use of optoelectronics in which semiconductor lasers generate large quantities of heat. Quantum cascade lasers (QCLs) use electron-phonon interactions to achieve population inversion [27, 28]; here it is important to have an accurate representation of heat tranport.

A more accurate way to simulate heat transport is to use the BTE for phonons. The formulation of this is discussed in section 2.3. This method has been used with charge carriers for some time [23,29]. Using proven techniques from carrier transport solutions, a more detailed model for heat transport can be developed.

There is no known fully analytical solution to the BTE for non-trivial systems. Instead, a numerical integration is used which requires simplistic assumptions. In the case of heat transport, this can mean simplifying the dispersion relation or using simple parameters to emulate geometrical effects and lattice defects. Reduced feature sizes have meant that more complex models are being employed in order to cater for quantum and other effects. This results in longer computational times.

1.3 Thermal simulation solutions

A number of attempts to create a reasonable model of heat transport have been reported using analytical (integration of the Boltzmann transport equation), stochastic (Monte Carlo) and molecular dynamics methods. Work has been done in modelling of heat transport for many years [30, 31], but until recently, due to the lack of computational power, the models used have been very simplistic. Though these solutions have produced results by these models that match experiment well, the simplicity of these models means they do not apply well to the complex structures seen in modern semiconductor devices.

Much of modern theory of thermal conduction in non-metallic solids comes from the work of Peierls [31]. He formulated the theory that thermal resistance is due to the anharmonicity of the inter-atomic forces. This effect is manifest as phonon-phonon scattering.

1.3.1 Analytical solutions

The relaxation time approximation has received much attention [11,32–35]. This is a calculation based on the scattering probability for a phonon. The relaxation time can be determined for a phonon and used to calculate thermal conductivity, accommodating geometric and temperature variation in a specific structure. These relaxation times can be used to calculate thermal conductivity from a simplistic derivative of the Boltzmann transport equation. A review of this work is included in section 3.2. The relaxation time approximation has been adapted to other solutions [36–38], though the calculations to derive them have previously used very simplistic approximations. A new formulation for the relaxation times is discussed in chapter 3.

1.3.2 Boltzmann transport equation based models.

Most of the transport theory in solids employs the Boltzmann transport equation. The BTE treats phonons as classical particles, solving for the density of excitations at a point in time [26]. The wave nature of the excitation is neglected as are interference phenomena. The BTE describes the time evolution of the phonon distribution function employing scattering rates calculated from the state of the phonon distribution.

Narumanchi [39] has developed a comprehensive solution for heat transport using the BTE with the relaxation time approximation as a basis. He uses a finite volume method to solve the two-dimensional BTE from a volumetric energy density expression.

Narumanchi states that heat transport cannot accurately be modelled without inclusion of optical phonons, and that acoustic to optical scattering adds an additional thermal resistance due to the low mobility of the optical branches. He uses this to make a simple approximation, reducing the optical phonon modes to a single mode. Phonons in this mode are static. He then uses this dispersion relation to recalculate the relaxation times for the acoustic modes. His BTE solution has been applied to a number of device structures [40] and seems to have improved agreement with experiment over the analytical techniques discussed above.

The quantum BTE [41] has been suggested as a way to solve the phonon distribution which includes wave information, however this technique is difficult to solve and is rarely used even in carrier transport methods [26]. No known attempt has been made to apply this to the phonon equation.

1.3.3 Molecular dynamics solutions

Molecular dynamics (MD) simulation involves the integration over time of Newton's equations of motion for an ensemble of atoms using interatomic potentials. This method requires no knowledge of heat transport, which means it is useful for investigating fundamental heat transfer mechanisms and can be used to investigate material interface boundaries. MD methods solve the equations of motion governing the trajectories of all the molecules in the system, then extract the desired information. The major limitation of this technique is that for structures larger then a few nanometers, it is extremely computationally expensive [2].

This method, though effective, is not easily included into a coupled electrothermal solution. Electrons cannot be included in this model due to its atomistic nature. The model, being entirely classical, will have each vibrational mode excited equally and will only be applicable to materials above the Debye temperature.

Chen [2] describes the use of MD solutions extensively. Chen states there are two methods for MD simulations: the equilibrium simulation, which can be used for transport properties such as thermal conductivity, and the non equilibrium method, which can be used for the transport process itself. The most common MD simulation uses the Green-Kubo approach in which the heat is analysed using a "direct method" [26] by imposing a temperature gradient over the system and determining the thermal conductivity using Fourier's Law. The Green-Kubo formula relates the autocorrelation of the heat flux changes of a system to transport properties.

1.3.4 Monte Carlo solution

The Monte Carlo method is a way to solve the BTE for phonons without using a complex expressions which will require large approximations. This method allows the simulation of the time evolution of a phonon distribution and all the effects that act upon it.

Until recently, the computational power required to perform Monte Carlo (MC) simulations of heat transport has not been available: as a result there have been few attempts at a solution of this sort. Mazumder [36] produced a solution using simple MC techniques. His solution is the starting point for the MC solutions discussed in chapter 4.

Mazumder's MC method tracks a population of "particles" in a semiconductor structure to emulate a real system. Each particle represents a single phonon or a number of phonons, and the ensemble evolves according to stochastically determined scattering events. These scattering events are caused by a number of lattice properties such as anharmonic phonon-phonon interactions and impurity scattering. The scattering events are determined by utilising the relaxation time approximation. The probabilities for events are calculated based on a local temperature prior to evolving the ensemble. The phonons distribution is evolved based on a simple equilibrium based re-population algorithm. The advantage of the MC method over analytical solutions is that boundary conditions, impurity scattering and other such quantum or size effects can be modelled explicitly.

1.3.5 Thermal model usage

The application of each of the thermal transport solutions discussed above is limited by length scale as shown in figure 1.2. In theory, all methods could be applied on the

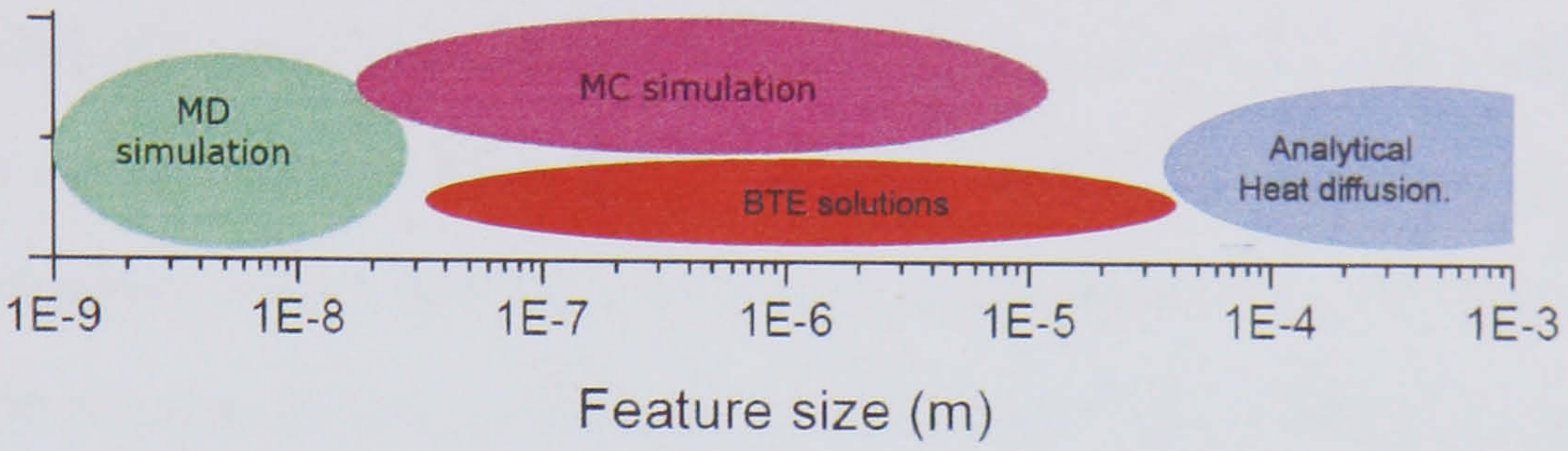

Figure 1.2: Feature size validity for various thermal models.

macro scale, however the information produced would be better approximated with a less complex model. The MD simulation is limited by the computational power available. Chen [2] recently stated that with the MD method, simulation of only a few thousand atoms is possible with standard computing equipment. The MC solution and the direct calculation of the BTE can be applied to larger systems and can predict heat transport in the phonon ballistic and diffusive limits [26]. The validity of the MC solution can be extended into lower length scales due to the exact nature of the solution. On length scales greater than the phonon mean free path, analytical solutions with application of Fourier's law provide sufficient accuracy. Below the mean free path and as structures become more complex at smaller geometries, these models deviate more from experimental values. The limits to all these models are not fixed, as with some approximations the ranges can be extended.

1.4 Summary

This chapter has introduced the motivation for development of more comprehensive heat transport model and a brief introduction to the methods currently in use. This work will catalogue the development of several methods to create a MC simulation of phonon transport. The following chapter (chapter 2) describes in greater detail the theory of thermal transport. Chapter 3 describes the calculation of phonon anharmonic scattering rates and applies these rates to an analytical thermal conductivity solution. Mazumder's [36] MC simulation is analysed in chapter 4 and several improvements to the algorithm are presented and disussed. In chapter 5 a MC simulation is developed, in which momentum conservation is applied to the anharmonic phonon interactions. Chapter 6 applies some of these models to nanowire structures. Chapter 7 concludes with a summary of the achievements of this work and possible areas for further development.

Chapter 2

Background

2.1 Basics of thermal transport

Heat conduction is the spontaneous transfer of thermal energy through matter from a region of higher temperature to lower temperature. This occurs though the combined effect of a number of processes, such as atomic vibration and electron interaction. The classical law of heat conduction, or Fourier's law, represents this diffusion process on the macro scale [42].

2.1.1 Fourier's law

Fourier's law (equation 2.1) states that net heat flux ($\mathbf{Q}$) is directly proportional to the negative gradient of the temperature difference ($\bigtriangledown T$) between two sections of a material,

$$\mathbf{Q} = -\kappa \bigtriangledown T \tag{2.1}$$

where κ is the thermal conductivity of the material. This assumes that the thermal conductivity is constant along the thermal gradient.

2.1.2 Validity of Fourier's law

A substantial amount of work has been done on the validity of Fourier's law [2, 43, 44], and the results show that thermal conductivity is temperature dependent. It can be seen in figure 2.1 that thermal conductivity can vary by an order of magnitude across a range of temperatures. Chen's [45] modelling along with with Sverdrup's [46] experimental results have shown that Fourier's Law underestimates temperature rise in modern small metal-oxide-semiconductor field-effect transistors (MOSFETs).

Fourier's Law relies on a temperature gradient in terms of the classic definition of temperature. This means that the time and length scales involved have to be sufficient for equilibrium to be established. This is not the case with modern semiconductor material structures such as quantum dots, nanowires and thin films, where the scales of the structures are within or close to the phonon mean free path.

2.2 Phonons and lattice dynamics

As the focus of this work is in semiconductor crystal structures, it is useful to take a brief look at lattice properties of crystal structures.

2.2.1 Lattice structure

Crystal structures are often described in terms of their unit cell. The structure comprises of the unit cell repeated over the whole structure. The unit cell itself is a spatial arrangement of atoms which determine the lattice parameters. The smallest of these cells is known as the primitive unit cell or the Wigner-Seitz cell (shown in figure 2.2).

A lattice is defined as an infinite regular array of points in which all points have identical surroundings. For every lattice we find three primitive translations, $\mathbf{a}_1, \mathbf{a}_2, \mathbf{a}_3$ such that the vector required to move from a chosen point in a unit cell to the same

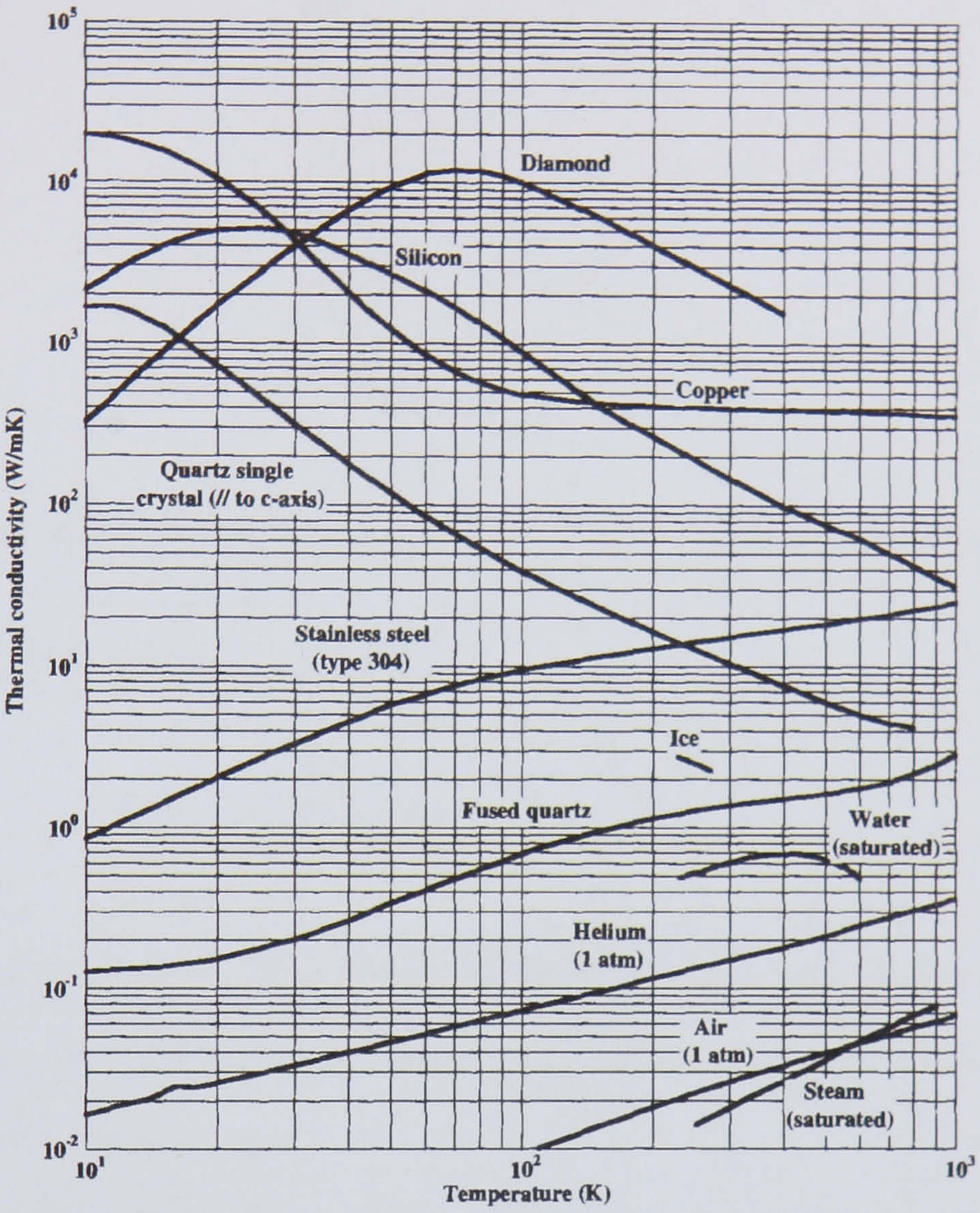

Figure 2.1: Thermal conductivity as a function of temperature for respective materials taken from [2] with data from [3].

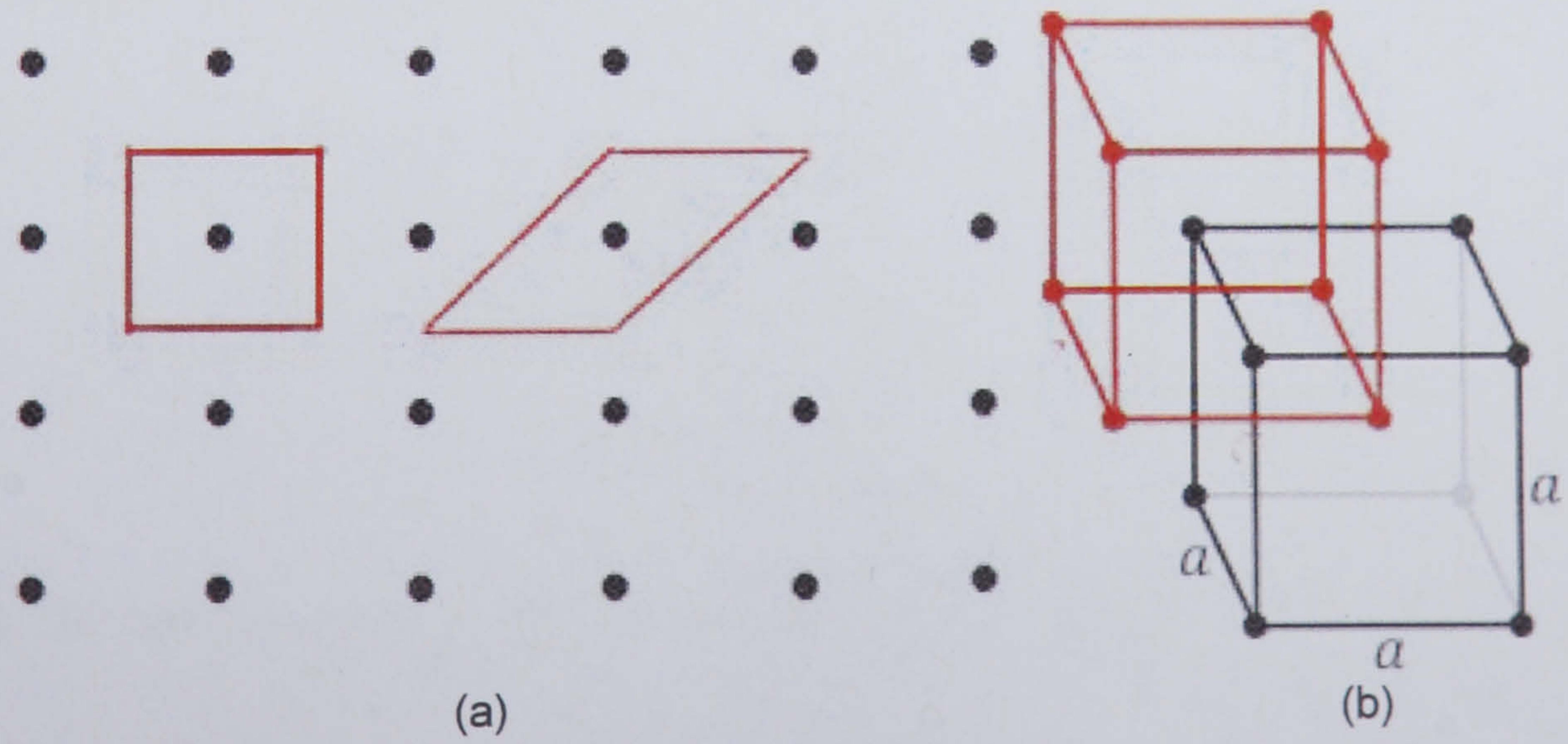

Figure 2.2: Wigner-Seitz cells indicated by the red lines in (a) a 2D lattice and (b) a 3D cubic lattice.

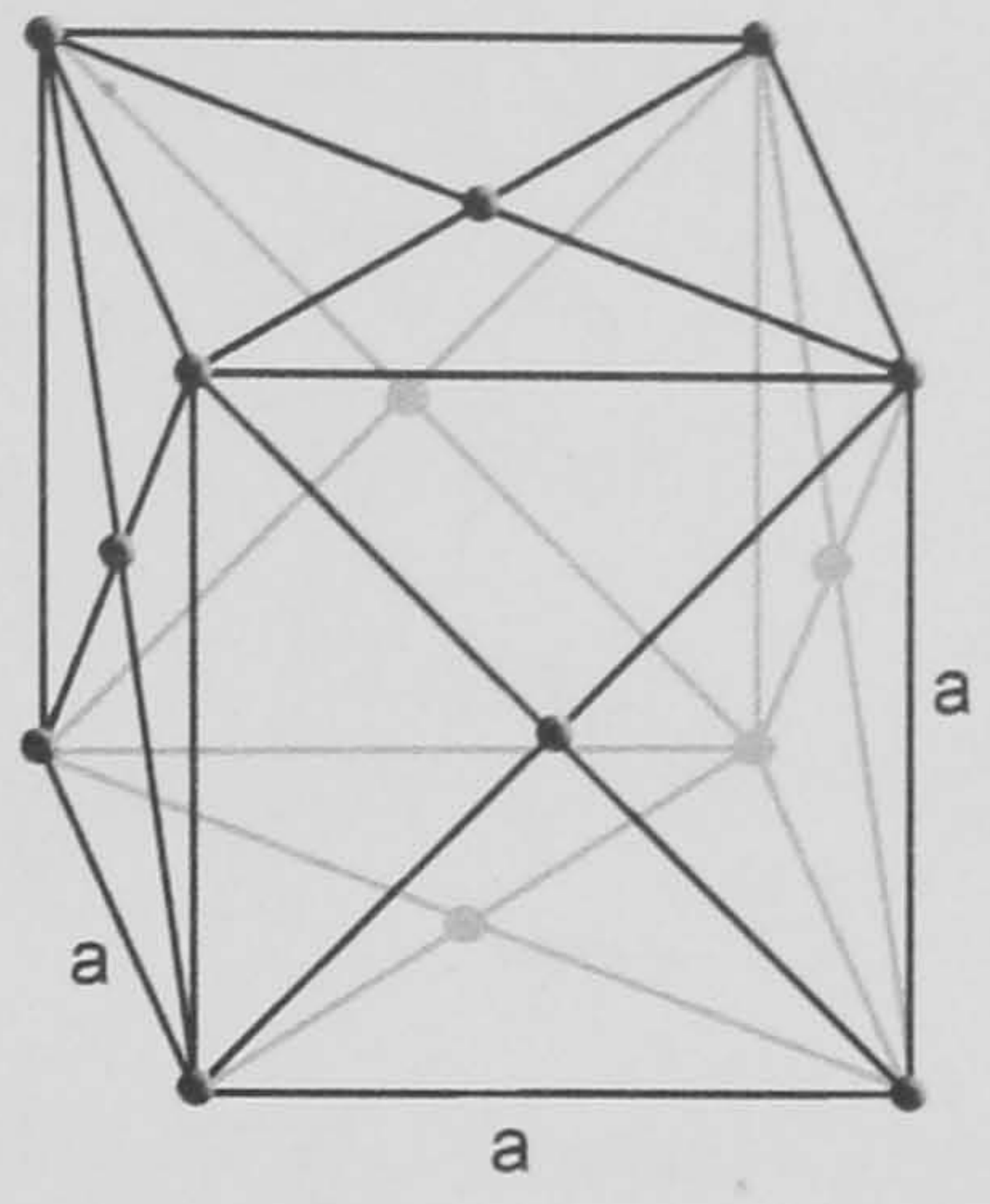

Figure 2.3: The crystal system for a face centred cubic unit cell.

point in another unit cell is

$$\mathbf{T} = n_1\mathbf{a}_1 + n_2\mathbf{a}_2 + n_3\mathbf{a}_3, \tag{2.2}$$

where n_1, n_2, n_3 are integers. The vector $\mathbf{T}$ defines a set of points known as the Bravais lattice. There are 14 distinct three-dimensional lattices and for convenience these can be grouped into 7 systems [47].

As the primary focus of this work has been silicon, the lattice structure examined below will be the face centered cubic (FCC) structure (shown in figure 2.3). The calculations for other materials and crystal structures can be found in [44, 47].

The primitive cell of an FCC lattice is defined as

$$\mathbf{a}_1 = \frac{a}{2}(0,1,1) \tag{2.3}$$

$$\mathbf{a}_2 = \frac{a}{2}(1,0,1) \tag{2.4}$$

$$\mathbf{a}_3 = \frac{a}{2}(1,1,0) \tag{2.5}$$

where a is the lattice constant and the volume of the cell Ω is

$$\Omega = |\mathbf{a}_1 \cdot (\mathbf{a}_2 \times \mathbf{a}_3)| = \frac{a^3}{8} \tag{2.6}$$

The reciprocal lattice is a construct in three dimensional reciprocal space (or momentum space) such that

$$e^{i\mathbf{G}\cdot\mathbf{T}} = 1 \tag{2.7}$$

where **G** is the reciprocal translation vector defined by

$$\mathbf{G} = m_1\mathbf{b}_1 + m_2\mathbf{b}_2 + m_3\mathbf{b}_3 \tag{2.8}$$

and where m_1, m_2, m_3 are integers and $\mathbf{b}_1, \mathbf{b}_2, \mathbf{b}_3$ are the primitive translational vectors defined by

$$\mathbf{b}_1 = 2\pi\frac{\mathbf{a}_2 \times \mathbf{a}_3}{\mathbf{a}_1 \cdot (\mathbf{a}_2 \times \mathbf{a}_3)} \tag{2.9}$$

$$\mathbf{b}_2 = 2\pi\frac{\mathbf{a}_3 \times \mathbf{a}_1}{\mathbf{a}_2 \cdot (\mathbf{a}_3 \times \mathbf{a}_1)} \tag{2.10}$$

$$\mathbf{b}_3 = 2\pi\frac{\mathbf{a}_1 \times \mathbf{a}_2}{\mathbf{a}_3 \cdot (\mathbf{a}_1 \times \mathbf{a}_2)} \tag{2.11}$$

The solutions for these in a FCC crystal are

$$\mathbf{b}_1 = \frac{2\pi}{a}(-1, 1, 1) \tag{2.12}$$

$$\mathbf{b}_2 = \frac{2\pi}{a}(1, -1, 1) \tag{2.13}$$

$$\mathbf{b}_3 = \frac{2\pi}{a}(1, 1, -1) \tag{2.14}$$

and the volume defined by these vectors is

$$\Omega_{rl} = 4\left(\frac{2\pi}{a}\right)^3 \tag{2.15}$$

The primitive unit cell of the reciprocal lattice is known as the first Brillouin zone. The significance of this construct is the specular reflection caused by the zone boundaries in wavevector space. This effect is discussed further in section 2.4.1.

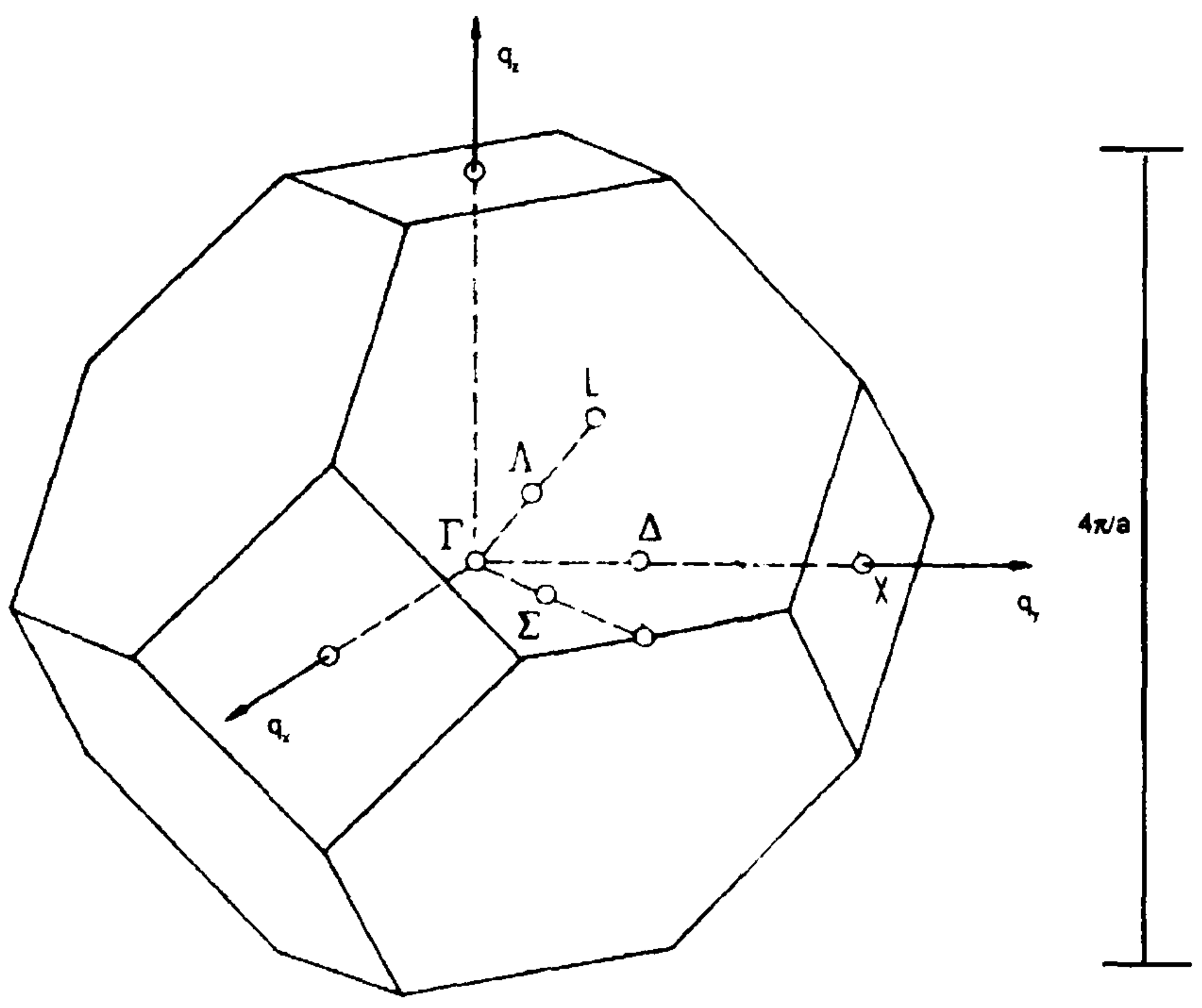

Figure 2.4: The Brillouin zone for a diamond lattice where, like silicon, Γ is the centre of the primitive reciprocal lattice.

2.2.2 Elastic theory

In order to understand the nature of phonon transport, the propagation of vibrational lattice energy must be discussed with relation to atomic movement. Mechanical vibrations in solids are essentially the movement of atomic sites in relation to their lattice position. This change is called deformation.

Classical elastic theory defines the deformation tensor as the shearing strain between orthogonal planes caused by displacement. So

$$\epsilon_{ij} = \frac{1}{2}(\zeta_{ij} + \zeta_{ji}) \tag{2.16}$$

where ϵ is the classical deformation tensor[1] and $\zeta_{ij} = \frac{\delta u_i}{\delta x_j}$ where $\mathbf{u}$ is displacement and $\mathbf{x}$ is the position.

In equation 2.16 this simple expression can be made by assuming that ζ is small and so only first order interactions are relevant. This approximation is usual with the classical theory but is insufficient when taking into account deviations from harmonic motion. With the inclusion of second order terms the expression of the deformation

---

[1] For further information about tensor notation see Appendix A

tensor becomes increasingly complex to

$$\eta_{ij} = \frac{1}{2}(\zeta_{ij} + \zeta_{ji} + \zeta_{ki}\zeta_{kj}). \tag{2.17}$$

From here on, η will be refered to as the second order deformation tensor.

When a body is deformed there are forces which restore it to its initial shape. These are internal stresses and are absent from an undeformed state. Thus

$$f_i = \frac{\partial \sigma_{ij}}{\partial x_j} \tag{2.18}$$

where f_i is the force component in the i^{th} direction and σ is the second rank stress tensor.

2.2.3 Hooke's law

When an external force creates a deformation upon an elastic body, this results in internal forces that try to remove the deformation. Increasing the former increases the latter and as a result there is a definite relationship between stress and deformation.

Hooke's law states that stress is proportional to strain in the form

$$\sigma_{ij} = c_{ijkl}\epsilon_{kl} \tag{2.19}$$

where c is the elastic constant,

$$c_{ijkl} = \left(\frac{\partial \sigma_{ij}}{\partial \epsilon_{kl}}\right)_{\epsilon_{kl}=0} \tag{2.20}$$

and σ_{ij} and ϵ_{kl} are second rank tensors such that c is an orthogonal fourth rank tensor.

2.2.4 Energy of a deformed crystal

It can be shown that the change in potential energy of a elastic body when undergoing small deformations [48] is given by

$$dW = \sigma_{kl} d\epsilon_{kl} = \frac{\partial W}{\partial \epsilon_{kl}} d\epsilon_{kl} \tag{2.21}$$

where W is the potential energy density. Assuming that potential in zero when there is no deformation, W is a homogeneous quadratic function of ϵ_{kl}. This implies that

$$W = \frac{1}{2}\sigma_{kl}\epsilon_{kl}. \tag{2.22}$$

Using equation (2.19) to remove the stress component we can define the elastic potential energy as

$$W = \frac{1}{2}c_{ijkl}\epsilon_{ij}\epsilon_{kl}, \tag{2.23}$$

which in terms of the deformation tensor η is

$$W = \frac{1}{2}c_{ijkl}\eta_{ij}\eta_{kl} + \frac{1}{6}c_{ijklmn}\eta_{ij}\eta_{kl}\eta_{mn} \tag{2.24}$$

to account for cubic term in ζ [49]. The c_{ijlkmn} are known as the third order elastic constants and form the components of a sixth-order tensor.

2.2.5 Elastic constants

There are a large number of second and third order elastic constants (c_{ijkl} and c_{ijklmn} respectively) as a result of the tensor scheme. This number can be reduced because of symmetry in the strain and stress tensor [49–51].

Reduction in the number of these constants can be made from the expression for internal energy and symmetry elements of the crystal [49]. From equation 2.23 we can state that $c_{ijkl} = \partial^2 W/(\partial\epsilon_{ij}\partial\epsilon_{kl})$, as W is a single valued function. the order of the differentiations is interchangeable. Thus

$$c_{ijlk} = c_{lkij} = c_{jilk} = c_{klij} \ldots$$

Further reduction occurs because of the symmetry of the unit cell. In a cubic cell, for example, there is a four fold axis of symmetry which means if the cells are rotated by a right angle, they will map on to another cell exactly. This applies to the tensor components and thus $c_{1111} = c_{2222}$ or $c_{1223} = c_{2113}$ and so on.

This means that second order elastic constants are reduced to c_{11}, c_{12} and c_{44}. The application of this scheme to third order tensor components can be seen in [51].

Traditionally these constants have been determined by matching various models to experimental phonon spectra [50,52–54]. Keating [52] shows that potential energy can be expressed as a function of various scalar products between the vectors representing the relative positions of the nuclei in a crystal structure. Using a method pioneered by Born and Huang [50], by imposing invariance requirements on the expression, calculation of the elasticity coefficients can be done. A list of these constants for various materials is available in [10,51].

2.2.6 Potential energy

In an isotropic material it is shown by Murnaghan [55] that η has 3 invariants: trace η, co. trace η and det. η. The three above quantities are independent of rotation of the initial coordinate axis due to isotropy. Using these invariants a general expression for W [49] in an isotropic medium can be written as

$$W = AI_1^2 + BI_2 + CI_1^3 + DI_1I_2 + EI_3 \tag{2.25}$$

where I_i represents the invariants below:

$$\begin{aligned} I_1 &= \text{Trace } \eta = \text{sum of diagonal elements of } \eta \\ &= \eta_{11} + \eta_{22} + \eta_{33}, \end{aligned}$$

$$\begin{aligned} I_2 &= \text{Trace co. } \eta = \text{sum of the three diagonal minors of } \eta \\ &= \eta_{22}\eta_{33} + \eta_{11}\eta_{33} + \eta_{11}\eta_{22} - (\eta_{23}^2 + \eta_{13}^2 + \eta_{12}^2), \end{aligned}$$

$$\begin{aligned} I_3 &= \text{determinant of } \eta \\ &= \eta_{11}\eta_{22}\eta_{33} + 2\eta_{23}\eta_{13}\eta_{12} - (\eta_{11}\eta_{23}^2 + \eta_{22}\eta_{13}^2 + \eta_{33}\eta_{12}^2). \end{aligned}$$

Using the fact $\eta_{ij} = \eta_{ji}$ and that $c_{ijklimn} = c_{mnklij} = c_{klijmn}$ etc, it can be shown from equation (2.25) that

$$W = \frac{1}{2}c_{1111}I_1^2 - (c_{1111} - c_{1122})I_2 + c_{111111}I_1^3 - 12c_{111313} + 24c_{121132}3I_3 \tag{2.26}$$

which, using a notation obtained by pairing the suffices, where

$$11 \rightarrow 1, 22 \rightarrow 2, 33 \rightarrow 3, 23 \rightarrow 4, 13 \rightarrow 5, 12 \rightarrow 6,$$

results in

$$W = \frac{1}{2}c_{11}I_1^2 - (c_{11} - c_{12})I_2 + c_{111}I_1^3 - 12c_{155} + 24c_{456}I_3.$$

Expressed in terms of ζ this gives

$$\begin{aligned} W &= \frac{1}{8}(c_{11} - c_{12})(\zeta_{ij} + \zeta_{ki})^2 + \frac{1}{2}c_{12}\zeta_{ii}\zeta_{jj} + \left(\frac{1}{2}c_{12} + 3c_{155} - 6c_{456}\right)\zeta_{ii}\zeta_{jk}^2 \\ &+ \left(\frac{1}{2}c_{11} - \frac{1}{2}c_{12} + 6c_{456}\right)\zeta_{ij}\zeta_{ki}\zeta_{kj} + (3c_{155} - 6c_{456})\zeta_{ii}\zeta_{jk}\zeta_{kj} \\ &+ (c_{111} - 6c_{155} + 4c_{456})\zeta_{ii}\zeta_{jj}\zeta_{kk} + 2c_{456}\zeta_{ij}\zeta_{jk}\zeta_{ki}, \end{aligned} \tag{2.27}$$

thus stating an expression which accounts for the cubic anharmonic interaction. The cubic terms of ζ above are those responsible for the interactions between the elastic waves. It can be seen from the third and fourth term in equation (2.27) that even in the absence of third order elastic constants, the potential energy function has cubic terms in ζ which indicate that harmonic motion contributes to third order effects.

2.2.7 Discrete lattice vibrations

The classical Hamiltonian for a one dimensional monatomic chain is [56]

$$H = \sum_{s=1}^{N} \{ \frac{p_s^2}{2M} + \frac{1}{2} C (u_s - u_{s+1})^2 \} \tag{2.28}$$

where N is the number of particles in the chain, M is the mass, C is the force constant between 2 particles, u is the displacement and p is the atomic momentum. The first term is the kinetic energy of the system and the second is the potential energy. Utilising the Fourier transforms of the normal mode operators

$$u(q) = \frac{1}{\sqrt{N}} \sum_{s=1}^{N} u_s e^{iqsa} \tag{2.29}$$

$$p(q) = \frac{1}{\sqrt{N}} \sum_{s=1}^{N} p_s e^{-iqsa} \tag{2.30}$$

and the commutation rule $[u(q), p(q')] = i\hbar\delta_{q,q'}$ we can express the Hamiltonian as

$$H = \frac{1}{2M} \sum_q p(q)p(-q) + \sum_q 2Cu(q)u(-q) \sin^2\left(\frac{1}{2}qa\right) \tag{2.31}$$

which, when using the creation ($a^\dagger$) and annihilation operators (a)

$$a(q) = (2M\hbar\omega(q))^{1/2}(p(q) - iM\omega(q)u(-q)) \tag{2.32}$$

$$a^\dagger(q) = (2M\hbar\omega(q))^{1/2}(p(-q) + iM\omega(q)u(q)) \tag{2.33}$$

can be expressed as

$$H = \sum_q \frac{1}{2}\hbar\omega(q)[a^\dagger(q)a(q) + a(q)a^\dagger(q)]. \tag{2.34}$$

The harmonic oscillator described by 2.34 for a particular q will have an associated set of eigenfunctions, of which the eigenvalues are

$$E_i(q) = \hbar\omega(q)\left(n(q) + \frac{1}{2}\right) \tag{2.35}$$

where i are the integer values from 0 to infinity.

The total energy of a lattice is

$$E_T = \sum_q \hbar\omega(q)\left(n(q) + \frac{1}{2}\right). \tag{2.36}$$

showing that vibrations in the lattice can be regarded as $n(q)$ quanta of energy with a ground state of $\frac{1}{2}\hbar\omega(q)$. These quanta are called phonons.

2.2.8 Phonons

Phonons have been used as a means of describing lattice vibrations in solids. Though they are quasi-particles that are regarded as bosons, some of their properties are derived from their wave nature.

Phonons are quanta of mechanical vibrations, and therefore have an associated polarisation. The different polarisations are representative of the way in which the lattice atoms move. Figure 2.5 shows how lattice movement relates to polarisation. This results in three branches of phonon modes; two transverse modes (in which the vibration is orthogonal to the direction of propagation) and one longitudinal mode (in which the vibration is parallel to the direction of propagation).

In solids with more then one atom in the smallest unit cell, two types of phonons

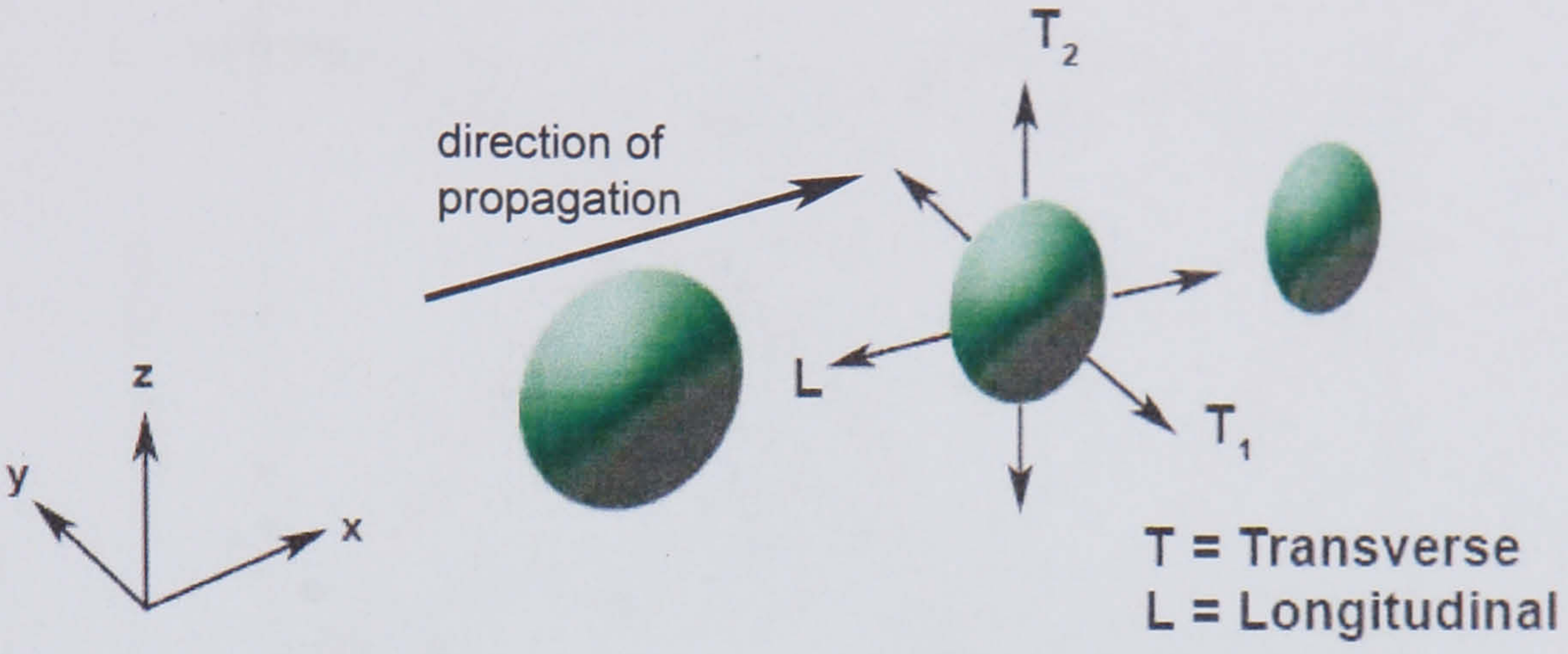

Figure 2.5: Direction of vibration for polarisation of phonon modes.

exist; acoustic and optical phonons. Acoustic phonons are phonons described by the Hamiltonian in equation 2.28. They have frequencies that become small at long wavelengths. Optical phonons occur when two (or more) atoms in a primitive cell move in opposite directions leaving the centre of mass at rest. This phonon type has highest energy when the wavelength is infinity, when the two sublattices move rigidly against each other.

In thermodynamic equilibrium the phonon occupation number n is determined by the Bose-Einstein distribution [23].

$$n = \frac{1}{e^{-\frac{\hbar\omega}{k_B T}} - 1} \tag{2.37}$$

where ω is the frequency of the phonon and k_B is the Boltzmann constant. The total energy in a crystal with volume $V$is

$$E = \sum_p \sum_{\mathbf{q}} \left(n(q) + \frac{1}{2} \right) \hbar\omega(q) \tag{2.38}$$

which, if integrated over the phonon wavevector $\mathbf{q}$ results in

$$E = \sum_p \int_q \left(n(q) + \frac{1}{2} \right) \hbar\omega(q) D(q) dq \tag{2.39}$$

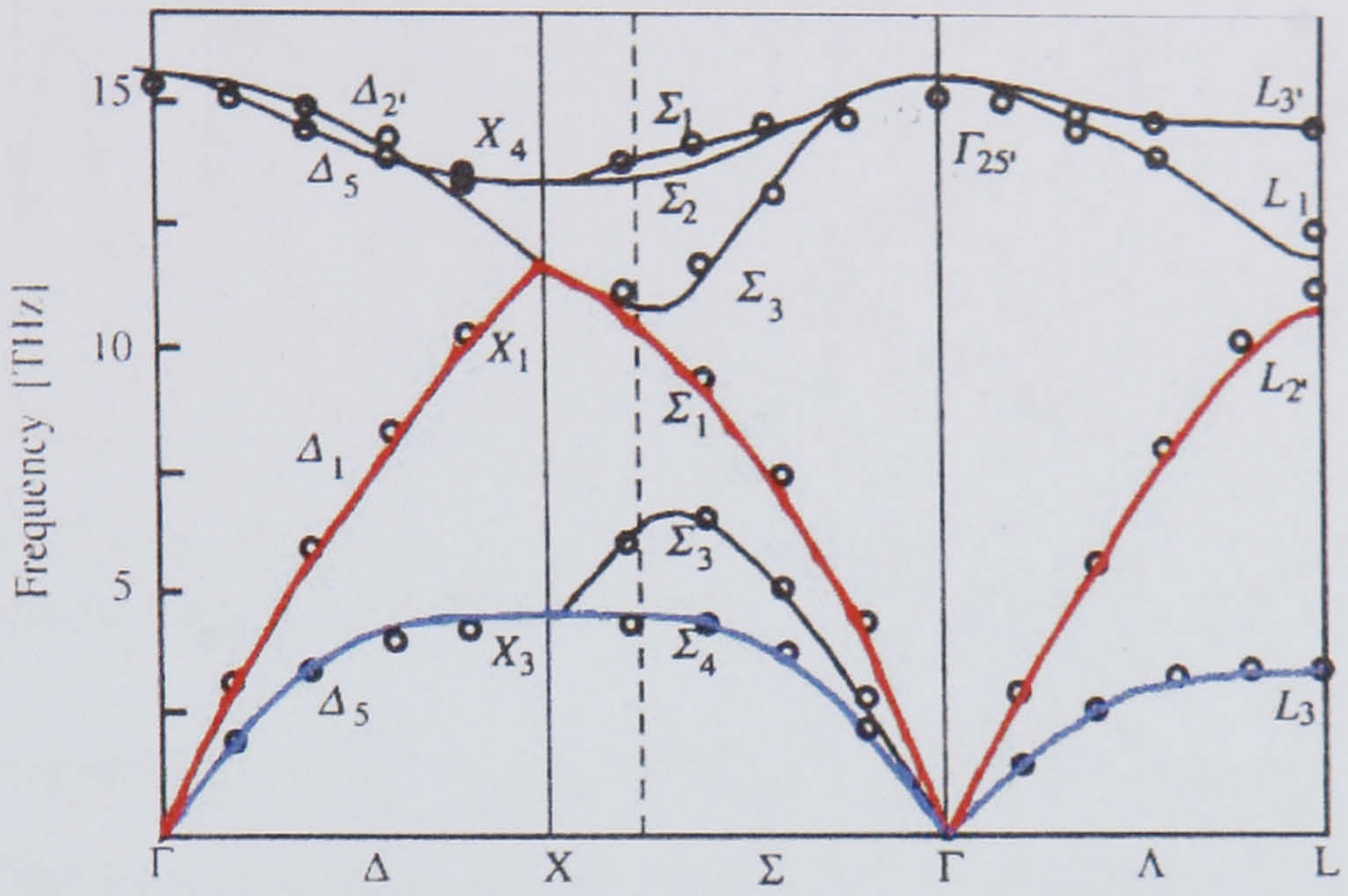

Figure 2.6: Dispersion relation for pure bulk silicon, graph taken from [4] with measurements from [5].

where $D(q)$ is the 3D density of states and is expressed as

$$D(q) = \frac{q^2}{2\pi^2} \tag{2.40}$$

2.2.9 Phonon dispersion

The phonon dispersion relation describes the relationship between the energy of a phonon and the wavelength in a material. This anisotropic relation determines the speed of sound and phonon movement in the lattice. Equation 2.41 shows the nature of this relationship, it should be noted that different modes will have different group velocities v_g:

$$v_g = \frac{d\omega}{dq}. \tag{2.41}$$

Figure 2.6 shows the dispersion relationship for phonons in silicon for orientations shown in figure 2.4. As in figure 2.4 Γ is the centre of a Brillouin zone. The red and blue lines showing the longitudinal and transverse acoustic relation respectively. The group velocity of optical phonons is low, and is often taken to be zero. This assumption is commonplace in phonon transport theory [24, 36, 57].

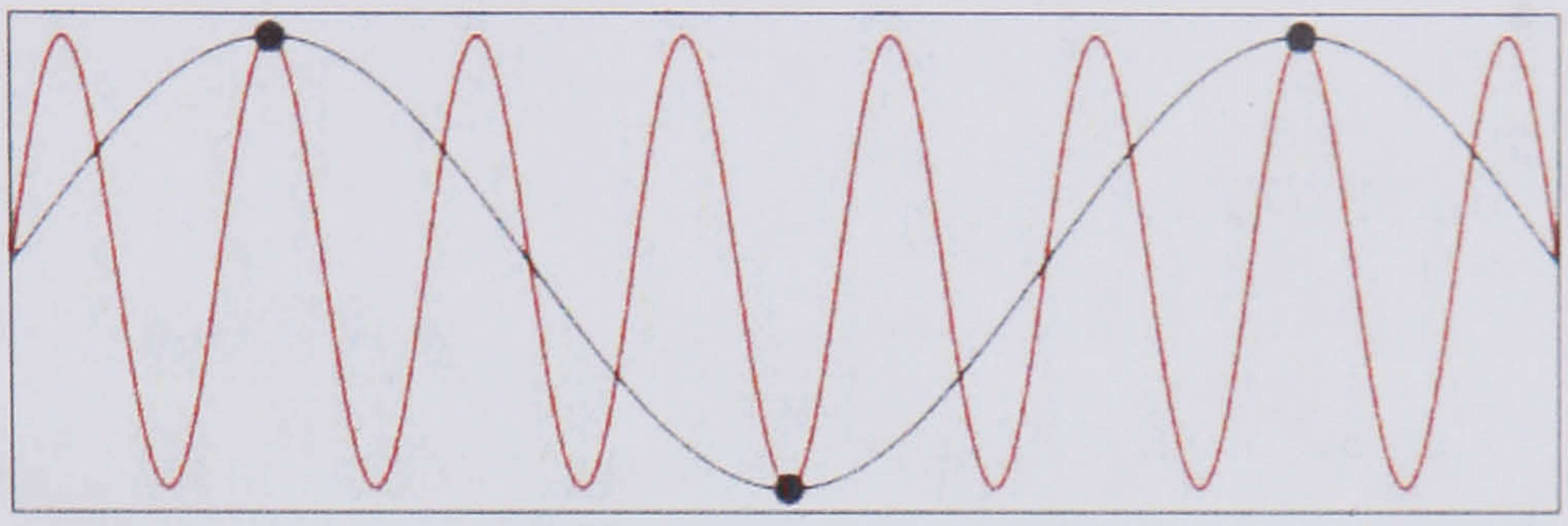

Figure 2.7: The atomic displacement is the same for both waves despite the fact that the wave represented by the red curve has 5 times smaller a wavelength.

There is a repetition of the dispersion relation between Brillouin zones which is caused by the vibration of atoms. As seen in figure 2.7, when wavelengths in the system decrease below the atomic spacing, there is no mechanism to reflect this increase in frequency. The decreased wavelength will not contain an increase in lattice vibrational energy. The lattice energy will be that of the equivalent wavelength in the first Brillouin zone resulting in the dispersion relation shown in figure 2.8.

Extensive work in both experiment and modelling has been carried out on the dispersion relationship, a summary of which can be found in [4]. Chung [37] states the rigorous treatment of phonon dispersion is essential to produce accurate thermal transport models.

2.3 Boltzmann transport equation for phonons

When the system length scale is too short for use of Fourier's Law, but large enough that phonon wavelengths are not similar in size and phase coherence is unimportant, then the BTE for phonons can be used. The BTE for phonons is expressed as [58]:

$$\frac{\partial f(t,\mathbf{r},\mathbf{q})}{\partial t} = [\frac{\partial f(t,\mathbf{r},\mathbf{q})}{\partial t}]_{scat} - v_g \cdot \nabla f, \tag{2.42}$$

where $f(t,\mathbf{r},\mathbf{q})$ is the distribution function for phonons with wavevector $\mathbf{q}$ and $\mathbf{r}$ is the position vector. The left hand side represents the net change to the phonon distribution. On the right hand side, the second term represents the changes to the distribution caused

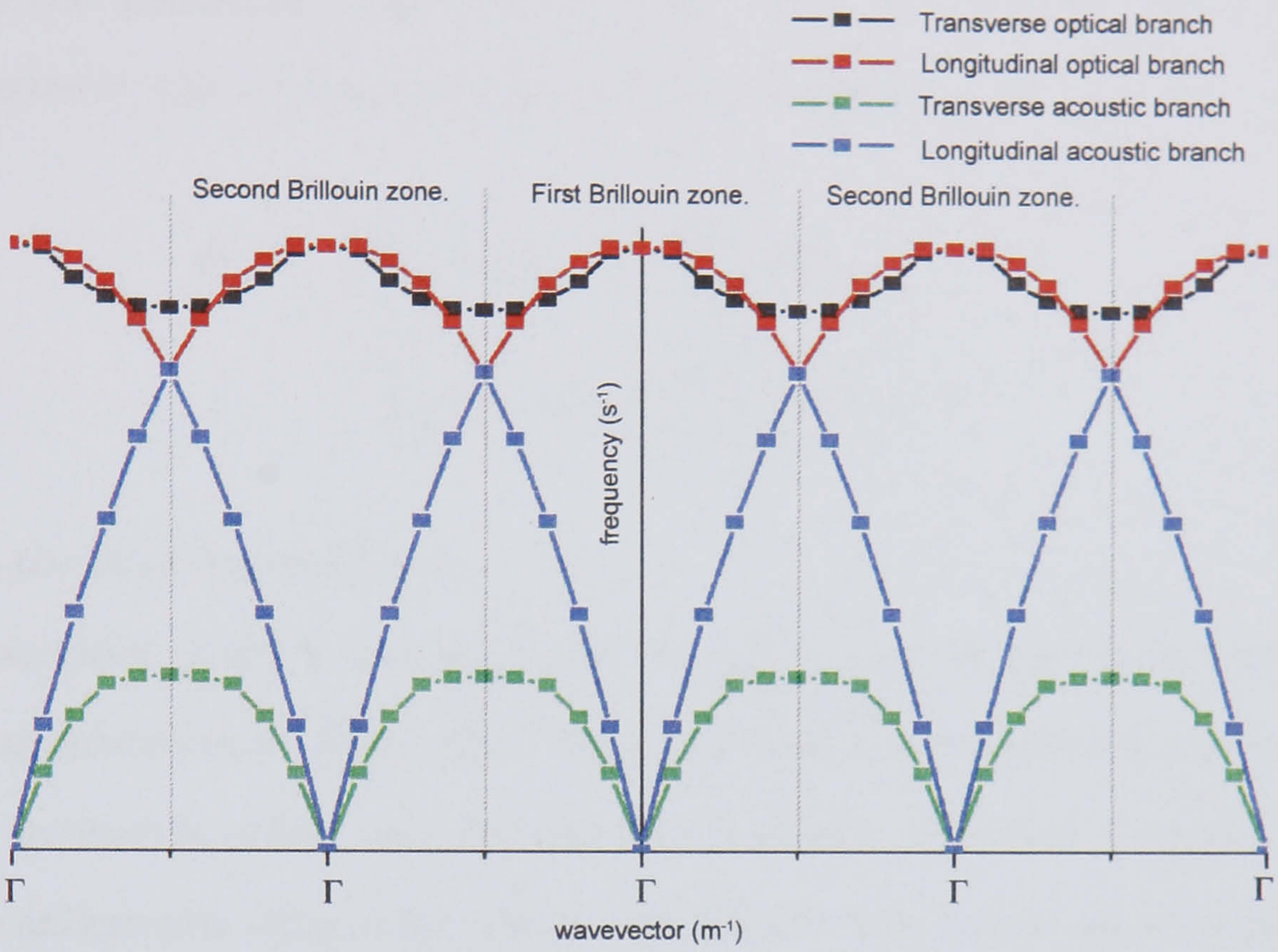

Figure 2.8: The first and second Brillouin zone in silicon [100] orientation (the Δ section in the graph above) using Dolling's [5] measurements.

by phonon diffusion and the first term represents the changes brought about by phonon scattering. Phonon scattering occurs due to a number of factors: anharmonic scattering, impurity or defect scattering and boundary scattering.

In an system in equilibrium, the net change of phonon distribution is zero. The anharmonic scattering term is the mechanism which will negate the changes caused by the other scattering terms, restoring equilibrium.

2.4 Anharmonicity in lattice dynamics

When atoms are displaced in a crystal we may write this in the form

$$\mathbf{r}_\alpha = \mathbf{r}_\alpha^0 + \mathbf{u}_\alpha \tag{2.43}$$

where x^0 is the unstrained position of the atom. If the potential energy is expanded in a Taylor series of atomic displacements then the Hamiltonian is

$$\begin{aligned} H &= \frac{1}{2}\sum_{\alpha} m\dot{u}_{\alpha} + \phi_0 + \sum_{\alpha}\phi_{\alpha}u_{\alpha} \\ &+ \frac{1}{2}\sum_{\alpha\beta}\phi_{\alpha\beta}u_{\alpha}u_{\beta} + \frac{1}{6}\sum_{\alpha\beta\gamma}\phi_{\alpha\beta\gamma}u_{\alpha}u_{\beta}u_{\gamma} + \ldots \end{aligned} \tag{2.44}$$

where ϕ is the coupling coefficient.

From equation (2.44) it can be shown that all except the last term represents the harmonic approximation. Subsequent terms represent the anharmonic interactions. As the terms increase in order, their influence is decreased: therefore in order to obtain a reasonable anharmonic approximation the third order term shown above is sufficient. In expressing the third order component of H in terms of (2.29) the expression obtained is

$$H_3' = \frac{1}{3!}\frac{1}{\sqrt{N}} \sum_{\binom{\mathbf{q}_1\mathbf{q}_2\mathbf{q}_3}{p_1p_2p_3}} \phi_{\binom{\mathbf{q}_1\mathbf{q}_2\mathbf{q}_3}{p_1p_2p_3}} u(\mathbf{q}_1,p_1)u(\mathbf{q}_2,p_2)u(\mathbf{q}_3,p_3) \tag{2.45}$$

where

$$\phi_{\binom{\mathbf{q}_1\mathbf{q}_2\mathbf{q}_3}{p_1p_2p_3}} = \frac{1}{N}\sum_{\alpha\beta\gamma}\frac{\phi_{\alpha\beta\gamma}}{(m_1m_2m_3)^{\frac{1}{2}}}\mathbf{e}_{\alpha}\mathbf{e}_{\beta}\mathbf{e}_{\gamma} \times \mathrm{e}^{-i\ \mathbf{q}_1\cdot\mathbf{r}_1+\mathbf{q}_2\cdot\mathbf{r}_2+\mathbf{q}_3\cdot\mathbf{r}_3}$$

and $\mathbf{e}$ indicates the polarisation. $\phi_{\alpha\beta\gamma}$ is invariant if a translation by a lattice vector is made.

2.4.1 Scattering events

Anharmonic interaction scattering events manifest themselves in phonon-phonon scattering. The primary scattering method is the three-phonon interaction [59]: higher orders of interaction (four or more phonon interactions) are generally regarded as negligible [60] since to the probability of these events occurring is much smaller than for three phonon scattering. Phonon-phonon interactions can be divided into two distinct

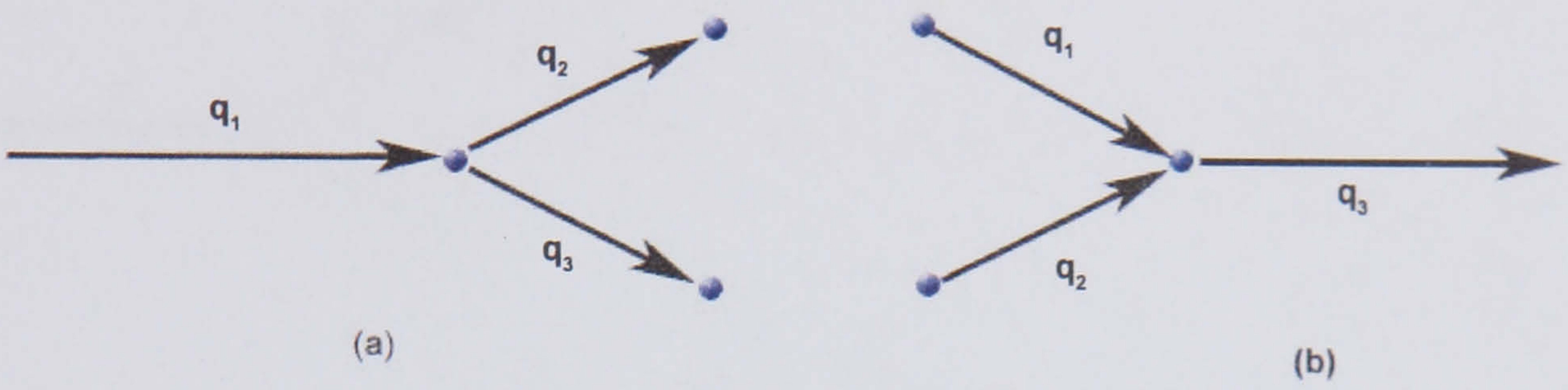

Figure 2.9: Normal scattering vector diagram of (a)decay process and (b) merge process.

types: Normal and Umklapp scattering. In the three-phonon process there are two ways in which the interaction can occur, a merge process whereby two phonons combine to create a higher energy phonon and a decay process where a phonon of a larger energy will decay into two phonons of lower energies.

Normal scattering is the scattering that implicitly conserves phonon momentum and energy such that

$$\mathbf{q}_1 = \mathbf{q}_2 + \mathbf{q}_3 \tag{2.46}$$

$$\omega(q_1, p_2) = \omega(q_2, p_2) + \omega(q_3, p_3) \tag{2.47}$$

as illustrated in figure 2.9(a) while in (b)

$$\mathbf{q}_1 + \mathbf{q}_2 = \mathbf{q}_3 \tag{2.48}$$

$$\omega(q_1, p_1) + \omega(q_2, p_2) = \omega(q_3, p_3) \tag{2.49}$$

Normal scattering (N processes) on its own cannot lead to a finite thermal conductivity due to the exact conservation of phonon momentum. This means that the overall forward momentum will be unhindered. N processes still play an significant role in heat movement by the redistribution of energy among the phonon polarisation branches.

Umklapp scattering is the primary cause of thermal resistance: this scattering method includes the lattice vector **G** which results in a net change in phonon mo-

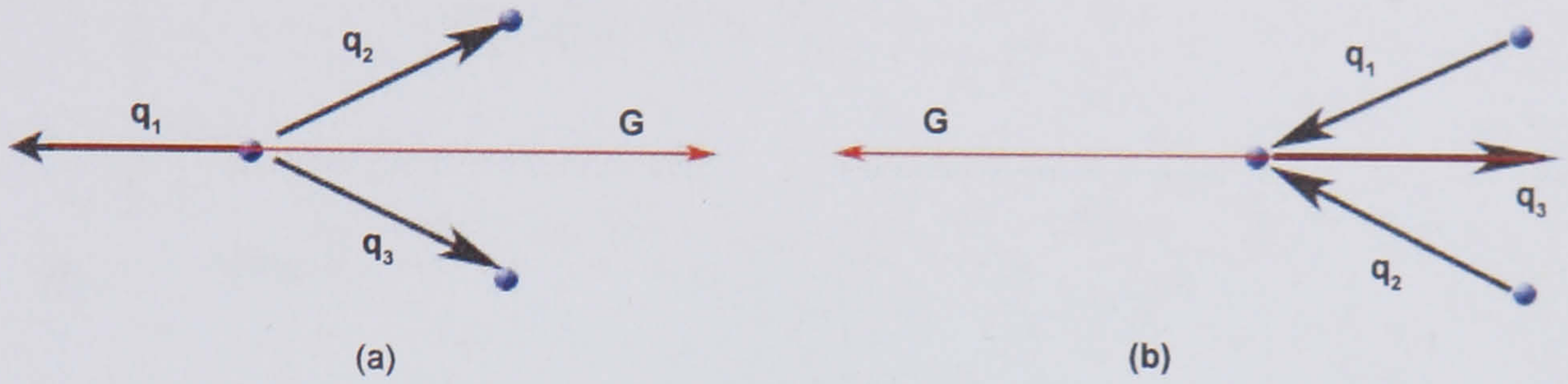

Figure 2.10: Umklapp scattering vector diagram of (a) decay process and (b) merge process.

mentum. These processes follow the following rules

$$\mathbf{q}_1 + \mathbf{G} = \mathbf{q}_2 + \mathbf{q}_3 \tag{2.50}$$

$$\omega(q_1, p_1) = \omega(q_2, p_2) + \omega(q_3, p_3) \tag{2.51}$$

as illustrated in figure 2.10(a) while in (b)

$$\mathbf{q}_1 + \mathbf{q}_2 = \mathbf{q}_3 + \mathbf{G} \tag{2.52}$$

$$\omega(q_1, p_1) + \omega(q_2, p_2) = \omega(q_3, p_3). \tag{2.53}$$

This occurs due to the periodicity of the dispersion relation in wavevector space. Figure 2.11 illustrates this effect using the simple dispersion relationship of a monatomic linear chain. The summation of the vectors from phonon 1 and phonon 2 results in a wavevector outside the first Brillouin zone; the reciprocal lattice vector reflects the resultant phonon wavevector back into the first Brillouin zone while preserving the group velocity of phonon 3.

Due to the energy conservation only certain transitions can occur within the scattering scheme. This has been discussed in a number of texts [23, 30, 56, 59]. Ziman provides a particularly useful explanation, using the nature of the dispersion curve. He illustrates this with figure 2.12 and by placing a copy of the dispersion relation at the point of a phonon's energy and wavevector position, he shows the transitions that can

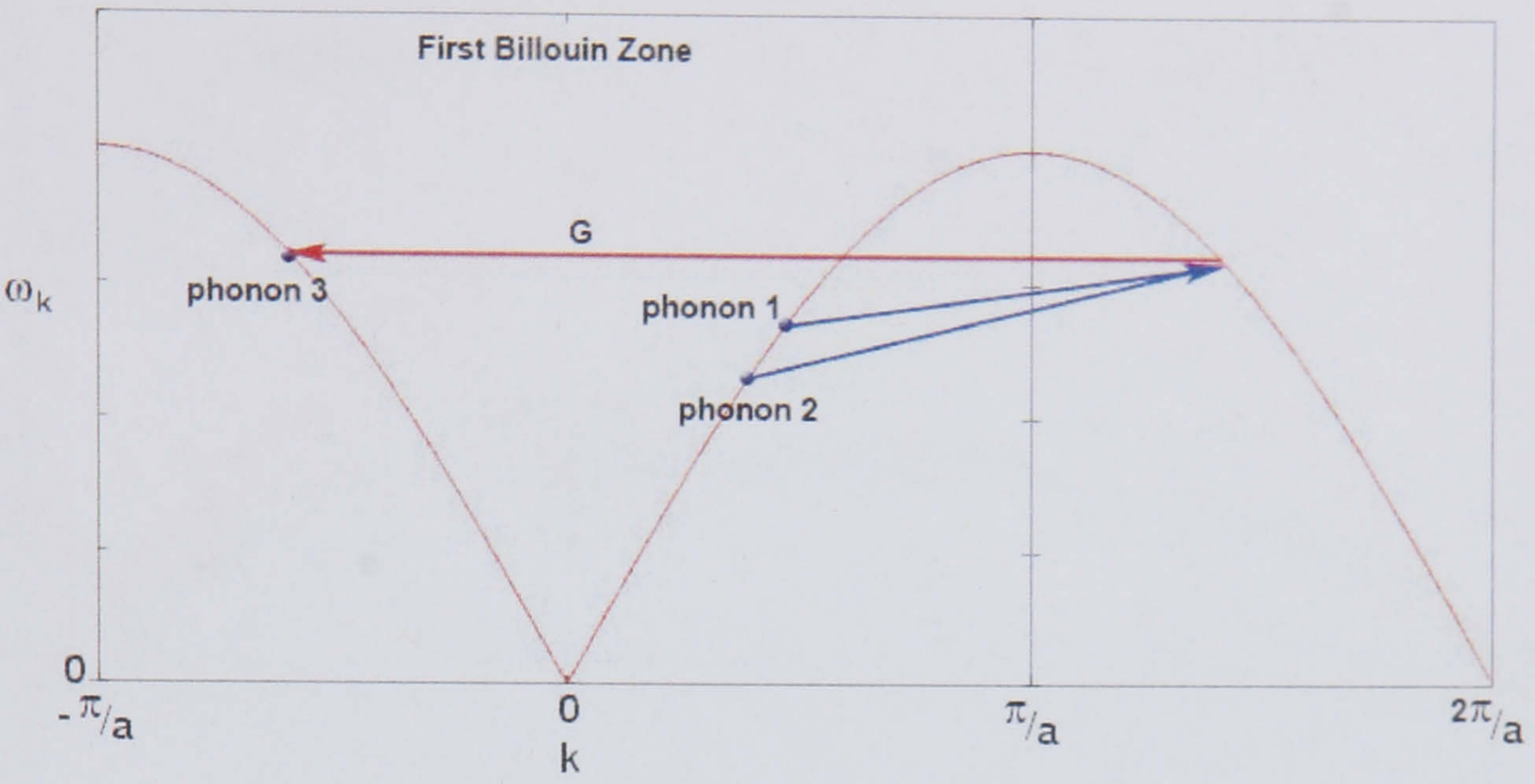

Figure 2.11: Umklapp scattering process in a linear monatomic lattice.

occur with energy and momentum conservation in a one dimensional system. These are indicated by where the second set of dispersion curves crosses the first. This illustrates that no transition can contain all three phonons from the same polarisation branch and that the largest energy phonon must lie in a higher branch than at least one of the other phonons. This continues to hold true in a three dimensional system. This means the possible transitions between acoustic branches are

$$LA \rightarrow TA + TA \tag{2.54}$$

$$LA \rightarrow LA + TA \tag{2.55}$$

$$TA + TA \rightarrow LA \tag{2.56}$$

$$LA + TA \rightarrow LA \tag{2.57}$$

where LA is the longitudinal branch and TA is the transverse branch. In addition to these restrictions, Tamura [61] states that for processes (2.54) and (2.56), the two TA phonon modes involved must be from the same polarization branches, while in processes 2.55 and 2.57 the TA phonon involved must be in the plane spanned by the wavevectors of the two LA phonons.

Scattering events also occur which involve the optical phonon branches; these how-

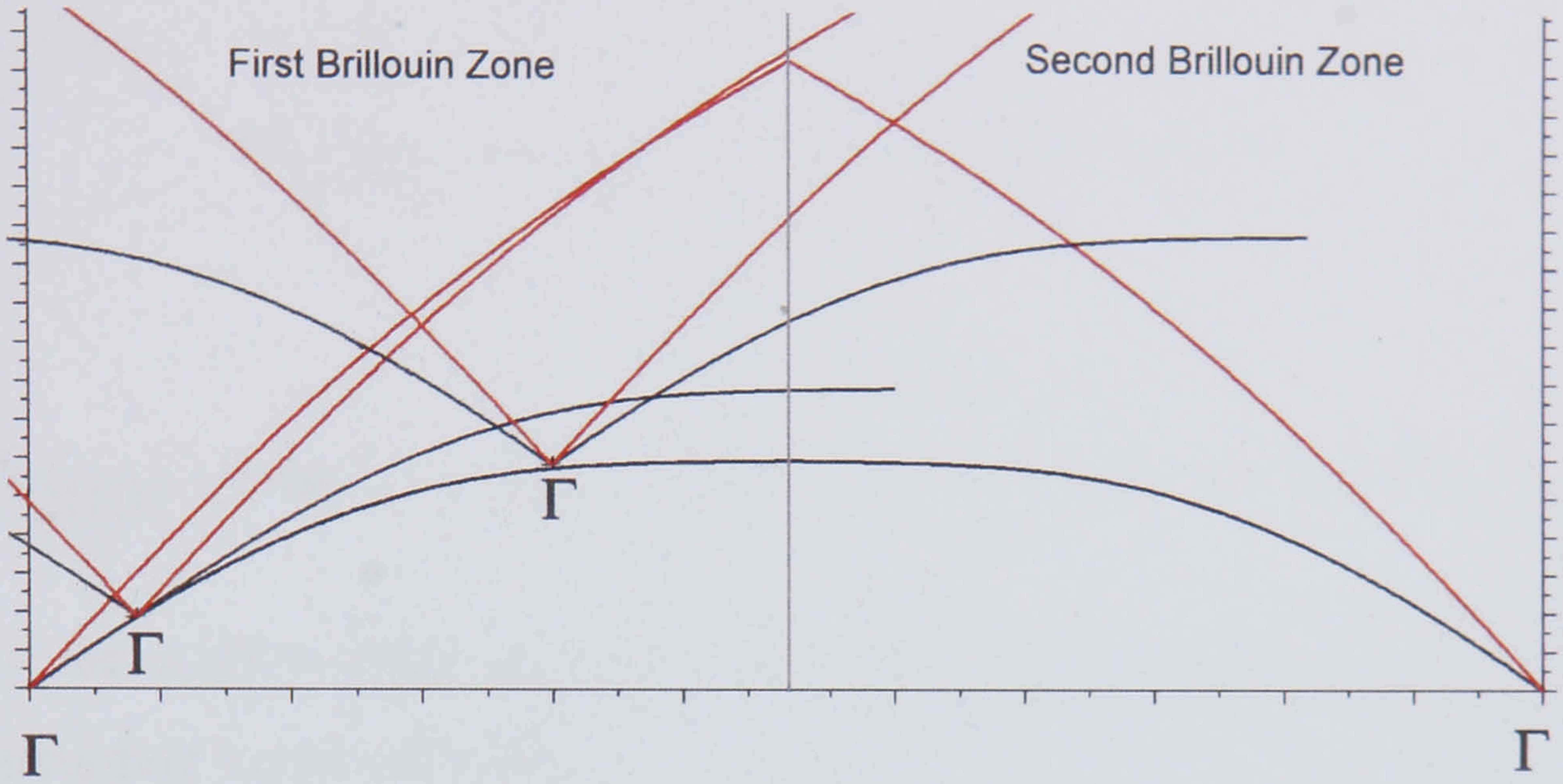

Figure 2.12: Illustration of energy and momentum conservation in a one dimensional system using silicon acoustic phonon dispersion. The points where the curves intersect indicate the allowed transitions.

ever have little effect on the transport characteristics. The relaxation times for the optical phonon population [62] are significantly lower than acoustic phonon scattering times [57]. This high frequency scattering means that these phonons will quickly degenerate into the acoustic branches. The high energy of the optical branches means that the acoustic phonons required to merge into these phonons will have high energies and low velocities, thus rendering any effect on the energy transport negligible.

2.5 Three phonon interactions

The anharmonic term H_3' above describes all phonon interactions which involve the collision of two phonons to create a higher energy phonon and the spontaneous decay of a phonon to two lower energy phonons. In order to calculate the time dependence of the occupation numbers and hence the relaxation time, H_3' must be expressed in terms of creation and annihilation operators. From equation (2.45) it can be found that

$$H_3' = -\frac{i}{3!}\frac{\hbar^{3/2}}{2^{2/3}N^{1/2}} \sum_{\left(\begin{smallmatrix}\mathbf{q}_1\mathbf{q}_2\mathbf{q}_3\\ p_1p_2p_3\end{smallmatrix}\right)} \mathbf{M}_{\left(\begin{smallmatrix}\mathbf{q}_1\mathbf{q}_2\mathbf{q}_3\\ p_1p_2p_3\end{smallmatrix}\right)} \mathbf{A}_{\left(\begin{smallmatrix}\mathbf{q}_1\mathbf{q}_2\mathbf{q}_3\\ p_1p_2p_3\end{smallmatrix}\right)} \tag{2.58}$$

where

$$\mathbf{M}_{\binom{q_1 q_2 q_3}{p_1 p_2 p_3}} = \phi_{\binom{q_1 q_2 q_3}{p_1 p_2 p_3}}[\omega(q_1, p_1)\omega(q_2, p_2)\omega(q_3, p_3)]^{-1/2}$$

and

$$\mathbf{A}_{\binom{q_1 q_2 q_3}{p_1 p_2 p_3}} = [a(q_1, p_1) - a^{\dagger}(q_1, p_1)][a(q_2, p_2) - a^{\dagger}(q_2, p_2)][a(q_3, p_3) - a^{\dagger}(q_3, p_3)]$$

where $a^{\dagger}$ and a are creation and annihilation operators. These operators act on these states according to the rules [59]

$$a^{\dagger}(q,p)|n(q,p)\rangle = \sqrt{(n(q,p)+1)}|n(q,p)+1\rangle \tag{2.59}$$

$$a(q,p)|n(q,p\rangle = \sqrt{(n(q,p))}|n(q,p)-1\rangle \tag{2.60}$$

The matrix elements for A can be shown to be:

for creation

$$\langle n(q_1,p_1)-1, n(q_2,p_2)-1, n(q_3,p_3)+1|A|n(q_1,p_1), n(q_2,p_2), n(q_3,p_3)\rangle$$
$$= -\{n(q_1,p_1)n(q_2,p_2)(n(q_3,p_3)+1)\}^{1/2}$$

$$\langle n(q_1,p_1)-1, n(q_2,p_2)+1, n(q_3,p_3)-1|A|n(q_1,p_1), n(q_2,p_2), n(q_3,p_3)\rangle$$
$$= -\{n(q_1,p_1)(n(q_2,p)+1)n(q_3,p_3)\}^{1/2}$$

$$\langle n(q_1,p_1)+1, n(q_2,p_2)-1, n(q_3,p_3)-1|A|n(q_1,p_1), n(q_2,p_2), n(q_3,p_3)\rangle$$
$$= -\{(n(q_1,p_1)+1)n(q_2,p_2)n(q_3,p_3)\}^{1/2}$$

for annihilation

$$\begin{aligned}
&\langle n(q_1,p_1)-1,n(q_2,p_2)+1,n(q_3,p_3)+1|A|n(q_1,p_1),n(q_2,p_2),n(q_3,p_3)\rangle \\
&\qquad = -\{n(q_1,p_1)(n(q_2,p_2)+1)(n(q_3,p_3)+1)\}^{1/2} \\
&\langle n(q_1,p_1)+1,n(q_2,p_2)-1,n(q_3,p_3)+1|A|n(q_1,p_1),n(q_2,p_2),n(q_3,p_3)\rangle \\
&\qquad = -\{(n(q_1,p_1)+1)n(q_2,p_2)(n(q_3,p_3)+1)\}^{1/2} \\
&\langle n(q_1,p_1)+1,n(q_2,p_2)+1,n(q_3,q_3)-1|A|n(q_1,p_1),n(q_2,p_2),n(q_3,p_3)\rangle \\
&\qquad = -\{(n(q_1,p_1)+1)(n(q_2,p_2)+1)n(q_3,p_3)\}^{1/2}
\end{aligned}$$

2.6 Three phonon transition rates

In order to calculate the rate at which H_3' may destroy a phonon (the relaxation time) use is made of time-dependent perturbation theory starting with Fermi's golden rule

$$P = \frac{2\pi}{\hbar} \sum_{\text{final states}} |H_3'|^2 \delta(E_f - E_i), \tag{2.61}$$

where P is the probability of a transition per unit time. From the expression (2.45) the displacement of a particle may be expressed in the form [49]

$$\mathbf{u} = \mathbf{i}\sum_q (\hbar/2\rho V\omega(\mathbf{q}))^{1/2}\mathbf{e}(\mathbf{q})\mathbf{e}^{i\mathbf{q}\cdot\mathbf{r}}[a(\mathbf{q}) - a^\dagger(\mathbf{q})] \tag{2.62}$$

where $\mathbf{e}(\mathbf{q})$ is the polarisation unit vector. Using the third order energy density expression shown below:

$$\begin{aligned}
H_3'/V &= W' = (\frac{1}{2}c_{12} + 3c_{155} - 6c_{456})\zeta_{ii}\zeta_{jk}^2 + (\frac{1}{2}c_{11} - \frac{1}{2}c_{12} + 6c_{456})\zeta_{ij}\zeta_{ki}\zeta_{kj} \\
&+ (3c_{155} - 6c_{456})\zeta_{ii}\zeta_{jk}\zeta_{kj} + (c_{111} - 6c_{155} + 4c_{456})\zeta_{ii}\zeta_{jj}\zeta_{kk} \qquad (2.63) \\
&+ 2c_{456}\zeta_{ij}\zeta_{jk}\zeta_{ki}
\end{aligned}$$

and substituting equation (2.62) into the equation (2.61) above, with some algebra, the resulting equation is

$$
\begin{aligned}
P(\mathbf{q}_1) &= \frac{2\pi\hbar}{8\rho^3 V\omega(\mathbf{q}_1)} \sum_{\left(\begin{smallmatrix}\mathbf{q}_2\mathbf{q}_3\\ p_2p_3\end{smallmatrix}\right)} \frac{\mid \mathbf{M}_{\left(\begin{smallmatrix}\mathbf{q}_1\mathbf{q}_2\mathbf{q}_3\\ \mathbf{p}_1\mathbf{p}_2\mathbf{p}_3\end{smallmatrix}\right)} \mid^2}{\omega(\mathbf{q}_2)\omega(\mathbf{q}_3)} \\
&\times \langle([n(\mathbf{q}_1)n(\mathbf{q}_2)(n(\mathbf{q}_3)+1)+(n(\mathbf{q}_1)+1)(n(\mathbf{q}_2)+1)n(\mathbf{q}_3)] \\
&\quad \delta(\omega(\mathbf{q}_1)+\omega(\mathbf{q}_2)-\omega(\mathbf{q}_3))\delta_{\mathbf{q}_1+\mathbf{q}_2,\mathbf{q}_3} \qquad (2.64) \\
&+ [(n(\mathbf{q}_1)+1)n(\mathbf{q}_2)n(\mathbf{q}_3)+n(\mathbf{q}_1)(n(\mathbf{q}_2)+1)(n(\mathbf{q}_3)+1)] \\
&\quad \delta(\omega(\mathbf{q}_1)-\omega(\mathbf{q}_2)-\omega(\mathbf{q}_3))\delta_{\mathbf{q}_1,\mathbf{q}_2+\mathbf{q}_3}\rangle
\end{aligned}
$$

where ρ is the mass density, $\mathbf{M}$ is the matrix element and V is the volume of the sample. $P(\mathbf{q}_1)$ is the probability of a transition involving a phonon of wavevector $\mathbf{q}_1$. The delta functions ensure momentum and energy conservation. The matrix element is [49,61]

$$
\begin{aligned}
\mathbf{M}_{\left(\begin{smallmatrix}\mathbf{q}_1\mathbf{q}_2\mathbf{q}_3\\ p_1p_2p_3\end{smallmatrix}\right)} &= A_1[(\mathbf{e}_1\cdot\mathbf{q}_1)(\mathbf{e}_2\cdot\mathbf{e}_3)(\mathbf{q}_2\cdot\mathbf{q}_3)+(\mathbf{e}_2\cdot\mathbf{q}_2)(\mathbf{e}_1\cdot\mathbf{e}_3)(\mathbf{q}_1\cdot\mathbf{q}_3) \\
&+ (\mathbf{e}_3\cdot\mathbf{q}_3)(\mathbf{e}_1\cdot\mathbf{e}_2)(\mathbf{q}_1\cdot\mathbf{q}_2)]+A_2[(\mathbf{e}_1\cdot\mathbf{q}_2)(\mathbf{q}_1\cdot\mathbf{q}_3)(\mathbf{e}_2\cdot\mathbf{e}_3) \\
&+ (\mathbf{e}_2\cdot\mathbf{q}_3)(\mathbf{q}_1\cdot\mathbf{q}_2)(\mathbf{e}_1\cdot\mathbf{e}_3)+(\mathbf{e}_3\cdot\mathbf{q}_1)(\mathbf{q}_2\cdot\mathbf{q}_3)(\mathbf{e}_1\cdot\mathbf{e}_2) \\
&+ (\mathbf{e}_1\cdot\mathbf{q}_3)(\mathbf{q}_1\cdot\mathbf{q}_2)(\mathbf{e}_2\cdot\mathbf{e}_3)+(\mathbf{e}_2\cdot\mathbf{q}_1)(\mathbf{q}_2\cdot\mathbf{q}_3)(\mathbf{e}_2\cdot\mathbf{e}_3) \\
&+ (\mathbf{e}_3\cdot\mathbf{q}_2)(\mathbf{q}_1\cdot\mathbf{q}_3)(\mathbf{e}_1\cdot\mathbf{e}_3)]+A_3[(\mathbf{e}_1\cdot\mathbf{q}_3)(\mathbf{e}_2\cdot\mathbf{q}_3)(\mathbf{e}_3\cdot\mathbf{q}_2) \qquad (2.65) \\
&+ (\mathbf{e}_1\cdot\mathbf{q}_2)(\mathbf{e}_2\cdot\mathbf{q}_3)(\mathbf{e}_3\cdot\mathbf{q}_1)]+A_4[(\mathbf{e}_1\cdot\mathbf{q}_1)(\mathbf{e}_2\cdot\mathbf{q}_3)(\mathbf{e}_3\cdot\mathbf{q}_2) \\
&+ (\mathbf{e}_2\cdot\mathbf{q}_2)(\mathbf{e}_1\cdot\mathbf{q}_3)(\mathbf{e}_3\cdot\mathbf{q}_1)(\mathbf{e}_3\cdot\mathbf{q}_3)(\mathbf{e}_1\cdot\mathbf{q}_2)(\mathbf{e}_2\cdot\mathbf{q}_1)] \\
&+ A_5[(\mathbf{e}_1\cdot\mathbf{q}_1)(\mathbf{e}_2\cdot\mathbf{q}_2)(\mathbf{e}_3\cdot\mathbf{q}_3)]
\end{aligned}
$$

where $\mathbf{e} = \mathbf{e}(\mathbf{q})$ and [49]

$$\begin{aligned} A_1 &= (c_{12} + 6c_{155} - 12c_{456}) \\ A_2 &= \frac{1}{2}(c_{11} - c_{12} + c_{456}) \\ A_3 &= 6c_{456}; A_4 = 6(c_{155} - 2c_{456}) \\ A_5 &= 6(c_{111} - 6c_{155} + 4c_{456}) \end{aligned}$$

For an equilibrium system the net transition rate for each phonon (creation less annihilation) is zero. This is the principle of detailed balance. From equation 2.64 it can be shown that the transition rates for a single transition are not equal:

$$n(\mathbf{q}_1)n(\mathbf{q}_2)(n(\mathbf{q}_3) + 1) \neq (n(\mathbf{q}_1) + 1)(n(\mathbf{q}_2) + 1)n(\mathbf{q}_3). \qquad (2.66)$$

The principle of detailed balance, therefore, applies only as a summation over all 3-phonon processes in the phonon ensemble.

2.6.1 Modal relaxation and phonon transition rates

The probability for a single scattering event occurring can be determined from equation 2.64. With the transition $\mathbf{q}_1(LA) \rightarrow \mathbf{q}_2(TA) + \mathbf{q}_2(TA)$ the rate at which this transition will occur is

$$\begin{aligned} P &= \frac{2\pi\hbar|\mathrm{M}|^2 n(\mathbf{q}_1)(n(\mathbf{q}_2) + 1)(n(\mathbf{q}_3) + 1)}{8\rho^3 V\omega(\mathbf{q}_1)\omega(\mathbf{q}_2)\omega(\mathbf{q}_3)} \\ &\times \ \delta(\omega(\mathbf{q}_1) - \omega(\mathbf{q}_2) - \omega(\mathbf{q}_3))\delta_{\mathbf{q}_1,\mathbf{q}_2+\mathbf{q}_3}. \end{aligned} \qquad (2.67)$$

This rate applies for an equilibrium distribution of phonons. P indicates that a phonon with the properties $\mathbf{q}_1(LA)$ will decay in this way. P is therefore the scattering rate for the phonon mode. The probability of a individual phonon scattering with this transition is determined by the following equation:

$$P_{phonon}(\mathbf{q},p) = \frac{P(\mathbf{q},p)}{n(\mathbf{q}.p)}. \tag{2.68}$$

P_{phonon} is the phonon scattering rate.

2.7 Phonons and temperature

The usual definition of temperature is related to the average energy of a system of particles. Temperature is normally defined for a system in equilibrium where the Bose-Einstein distribution, seen in equation 2.37, describes the phonons in the system; this can even be applied on the nanoscale. This definition is harder when dealing with heat transport; the movement of heat on the nanoscale can result in a change of phonon distribution which is a deviation from equilibrium. The validity of the concept of non-equilibrium temperature is discussed in Cahill's review [26]. Cahill states it is difficult to talk about temperature as a non-equilibrium construct especially on an atomistic level. He provides several definitions of temperature.

The purely classical definition of temperature states a direct relationship between atomic movement and temperature:

$$\frac{1}{2}Mv_i^2 = \frac{3}{2}k_BT_i, \tag{2.69}$$

where T_i is the temperature of an atom at site i. This is a common approach in molecular dynamic (MD) simulations.

Another approach is derived from a more quantum mechanical definition. The average kinetic energy of phonons is determined by

$$\frac{1}{2}Mv_i^2 = \frac{1}{4N}\sum_{p,\mathbf{q}} \hbar\omega(q,p)|\mathbf{e}|^2(q,p)[\frac{2}{e^{\hbar\omega/k_BT_i}-1}+1] \tag{2.70}$$

where N is the number of unit cells and $\mathbf{e}$ is the polarisation vector. Cahill also postulates that temperature may be defined by removing the zero point motion from the quantum definition, since the effect is non-classical.

Even with the theory set out above, local temperature is difficult to describe. Using the classical definition we can define temperature for a single atom simply by regarding the motion of the atom. For the quantum definition, the length scale is defined by the mean-free-path of the phonon population. This can be a problematic in MC solutions, as the classical is hard to calculate with approximations made, and the quantum mechanical definition is too large for use in nanoscale simulation.

An alternative, which is used in this work, is to use the quantum mechanical definition, removing the zero point motion, to create a relationship between equilibrium energy and temperature. A local temperature can then be defined by the energy within a specified region and not by the phonon distribution as in equation 2.70. This method has the advantage that a temperature can be evaluated for a non equilibrium system, and can also be used at length scales smaller then the phonon mean free path. This method has found use in MC simulation [36].

Chapter 3

Anharmonic interaction rates

3.1 Anharmonicity and relaxation times

The relaxation time approximation is a proven technique for representing anharmonic effects in thermal conductivity calculations as discussed in section 3.2. The relaxation time is traditionally derived from Herring's single mode approximation [63]. His work has been supported experimentally but uses fitting parameters to match the data as well as arbitrary temperature variation in the calculation.

Ziman [59] suggests that an exact relaxation time can be calculated using the mathematics discussed in section 2.4. With more exact calculations, fitting parameters play less of a role. The probability of a scattering event occurring in a material is determined by 2.64. The relaxation time is

$$\tau(\mathbf{q},p)=\frac{1}{P(\mathbf{q},p)}. \tag{3.1}$$

3.2 Review of relaxation time solutions

Several attempts have been made to provide reasonable approximation for anharmonic phonon interaction. Some of these are discussed below.

3.2.1 Holland's thermal conductivity solution

Holland [11] describes a thermal conductivity solution based on the work of Debye and Peierls [64]; the simple principles established have been used in many subsequent works. The relaxation time approximation when applied to the Boltzmann equation gives thermal conductivity in the form

$$\kappa = \frac{1}{(2\pi)^3} \sum_p \int (\mathbf{v}(\mathbf{q}, p) \cdot \mathbf{i})^2 \tau(\mathbf{q}, p) C_{ph}(\mathbf{q}, p) d\mathbf{q} \tag{3.2}$$

where $\mathbf{v}$ is the phonon velocity, the temperature gradient is along the $\mathbf{i}$ vector and $C_{ph}$is the specific heat per normal mode which is determined by

$$C_{ph}(x) = kx^2 e^x \{e^x - 1\}^{-2}. \tag{3.3}$$

Here $x = \hbar\omega(\mathbf{q})/k_B T$ and τ is the phonon relaxation time.

Callaway [32] uses the above to derive the following equation:

$$\kappa = CT^3 \int_0^{\theta_D/T} \frac{x^4 e^x (e^x - 1)^{-2} dx}{v_b/L + \alpha x^4 T^4 + (\beta_1 + \beta_2) x^2 T^5} + \kappa_2, \tag{3.4}$$

where

$$C = \left(\frac{k}{2\pi^2 v_s}\right) \left(\frac{k}{\hbar}\right)^3,$$

$\alpha = A(k/\hbar)^4$, $\beta_i = B_i(k/\hbar)^2$, θ_D is the Debye Temperature and κ_2 is a correction factor. The denominator contains the scattering terms in which the 3 components are: v_b/L for the boundary scattering, $\alpha x^4 T^4$ for the isotope scattering, and $(\beta_1 + \beta_2) x^2 T^5$ for the anharmonic scattering (in which β_1 is the Umklapp process and β_2 is the Normal process). This equation was derived by assuming that relaxation times are a function of frequency and temperature. Callaway treats the material as elastically isotropic, ignores dispersion, and makes no distinction between different polarisation branches.

Callaway's approach has had some success in matching experimental data at low temperatures (1.5K to 100K); however even in this range the peak thermal conductivity is overestimated by a factor of two. A further analysis of Callaway's theory can be found in [65]. McGaughey [66] shows that a single mode approximation works well at low temperatures, but with greater anharmonic interaction at higher temperatures the model falls down. Carruthers [35] also mentions that this method would be inaccurate at high temperatures.

Holland adds to the basic idea of Callway's model by modelling two branches of the phonon dispersion relation (LA and TA) and separating the Normal and Umklapp processes. This results in new relaxation times determined by:

$$\tau_L^{-1} = B_L \omega^3 T^3 \tag{3.5}$$

at low temperatures, and

$$\tau_L^{-1} = B'_L \omega^2 T \tag{3.6}$$

at high temperatures, for the longitudinal acoustic mode;

$$\tau_{TN}^{-1} = B_T \omega T^4 \tag{3.7}$$

at low temperatures,

$$\tau_{TN}^{-1} = B'_T \omega T \tag{3.8}$$

at high temperatures, for Normal processes in the transverse mode; and

$$\tau_{TU}^{-1} = B_{TU} \frac{\omega^2}{\sinh \hbar/k_B T} \tag{3.9}$$

for Umklapp processes in the transverse mode, which does not occur until the wavevector of the phonon is $q_{MAX}/4$ where q_{MAX} is the length of the Billouin zone.

Holland derives his Normal scattering expressions from Herring's calculations [63] for relaxation times. Herring also uses a single mode approximation which gives the frequency and temperature dependence. Applying his method to a two branch model will give different results. This is discussed further in section 3.6.2.

The Umklapp processes are derived from work by Klemens [33] and his methodology is discussed in detail in the appendix of [11]. Klemens obtains the expression

$$\tau_U^{-1} = -\sum_{\mathbf{q}'\mathbf{q}''} A_{qq'q''} \frac{\mathbf{e}\cdot\mathbf{G}}{\mathbf{e}\cdot\mathbf{q}} \frac{(e^x - 1)}{(e^{x'} - 1)(e^x - e^{-x'})} \tag{3.10}$$

where

$$A_{qq'q''} \propto \omega\omega'\omega''. \tag{3.11}$$

Holland makes the observation that for the $TA + TA \rightarrow LA$, $\omega \sim \omega'$ and $\omega'' \sim 2\omega$, he then evaluates the expression above as equation 3.9.

Holland's approach results in the thermal conductivity equation:

$$\kappa_T = \kappa_L + \kappa_T + \kappa_{TU} \tag{3.12}$$

where

$$\kappa_T = \frac{2}{3}T^3 \int_0^{\theta_1/T} \frac{C_T x^4 e^x (e^x - 1)^{-2} dx}{v_b/LF + \alpha x^4 T^4 + \beta_T x T^5} \tag{3.13}$$

$$\kappa_{TU} = \frac{2}{3}T^3 \int_{\theta_1/T}^{\theta_2/T} \frac{C_T x^4 e^x (e^x - 1)^{-2} dx}{v_b/LF + \alpha x^4 T^4 + \beta_{TU} x^2 T^2/\sinh x} \tag{3.14}$$

$$\kappa_L = \frac{1}{3}T^3 \int_0^{\theta_3/T} \frac{C_L x^4 e^x (e^x - 1)^{-2} dx}{v_b/LF + \alpha x^4 T^4 + \beta_L x^2 T^5} \tag{3.15}$$

where $x = \hbar\omega/k_B T, \theta = k_B\omega/\hbar, C = (k_B/2\pi^2 v_i)(k_B/\hbar)^3$,

$$v_b^{-1} = \frac{1}{3}(2v_T^{-1} + v_L^{-1}) \tag{3.16}$$

α and β are defined as in equation 3.4 and F is a correction factor to cater for surface smoothness and the finite length to thickness ratio of a semiconductor structure. The numerical values for constants can be found in [57] and are catalogued in appendix B.

Though Holland does use a more comprehensive representation of phonon dispersion than Callaway, he still does not account for it fully. The dispersion relation is approximated using a piecewise linear spline and there is no distinction between the two orthogonal TA branches.

In Holland's analysis, there is no distinction between high and low temperatures. He states that this boundary is an arbitrary value that is required in order for the calculation to match adequately to the experimental data. The result of his calculations does seem to match the thermal conductivity values across the temperature range from 1.5K to 1500K, though there has been some criticism of his methodology in the literature. Chung [37] states that since Holland's expression is based on low frequency approximations, they do not accurately predict thermal transport at high temperatures where the phonon interaction is primarily at high frequencies.

3.2.2 Tamura's phonon scattering probability calculations

Tamura considers the spontaneous decay rates of LA phonons [61] as well as surface scattering [67]. His method for scattering probability calculations is based on equation 2.64. Tamura writes this equation in the form

$$P(\mathbf{q}_1, p_1) = \frac{\pi\hbar}{8\rho^3 V\omega(q_1, p_1)} \sum_{\mathbf{q}_2} \sum_{p_2, p_3} \frac{|M(\mathbf{q}_1, \mathbf{q}_2, \mathbf{q}_1 - \mathbf{q}_2, p_1, p_2, p_3)|^2}{\omega(q_2, p_2)\omega(|\mathbf{q}_1 - \mathbf{q}_2|, p_3)} \delta(\omega(q_1, p_1) - \omega(q_2, p_2) - \omega(|\mathbf{q}_1 - \mathbf{q}_2|, p_3)) \tag{3.17}$$

which does not take into account phonon populations, and as a result has no temperature dependence. Tamura makes this approximation since he is calculating individual phonon scattering rates at low temperatures. As the phonon distribution dependence in a decay process is $(\langle n(q_2,p)\rangle+1)(\langle n(q_3,p)\rangle+1)$ and at low temperatures the phonon distributions for all phonons at equilibrium are significantly smaller than one. the phonon distribution terms, and hence the temperature can be neglected. The merge process does still have some temperature dependence and this can be seen in [68].

Tamura's work has been used by Wolfe [69] in phonon imaging solutions in order to understand low temperature heat movement. Applications of their work are in the development of phonon detectors and to further understand point disturbance effects on phonon distribution. Tamura's work is generally concerned with small specialized structures which are prone to being phonon hotspots and not towards the formation of a self consistent electrothermal solution.

3.3 Two mode relaxation approximation

To improve on the single mode relaxation time approximation and its derivatives, that are predominant in the literature [11, 32, 35, 63], this work develops a model which utilises a better description of the phonon dispersion relation for silicon. The model uses two phonon modes calculating the relaxation times accordingly. The derivation used here can be extended to all other semiconductor materials. For this calculation some approximations still have to be made.

The dispersion relation uses 2 modes: the LA mode and the TA mode (no distinction is made between the two orthogonal transverse polarisation modes). The dispersion curves are emulated with parabolic splines shown in Appendix E.2.

The dispersion relation is assumed to be isotropic. The result of this is that the constant energy surfaces are spherical. From the dispersion relation shown in 2.6 we can see that there is some change in the dispersion relation with orientation of the crystal. Ziman [59] shows that the constant energy surface deviates from spherical for the TA branch, however Herring [63] shows that the effect of this is negligible.

The Brillouin zone is approximated as a sphere with a radius of $2\pi/a$. With this approximation it can be determined, using equation 2.15, that the volume error is only 4%. The effect is that, in a U-process, we can assume that the reciprocal lattice vector is always parallel to the wavevector of the highest energy phonon.[1]

3.4 Relaxation time calculation

The calculation starts with equation 2.64. To determine the relaxation time for a phonon, only transitions where the phonon is annihilated are taken into account. The equation can be simplified by using momentum conservation to replace $\mathbf{q}_3$. Expressing $\mathbf{q}_2$ in polar coordinates and replacing the sum over $\mathbf{q}_2$ by an integral results in

$$\begin{aligned} P(\mathbf{q}_1) &= \frac{\pi\hbar}{4\rho^3 V\omega(\mathbf{q}_1)}\left(\frac{V}{8\pi^3}\right)\sum_{p_2p_3}\int_0^{2\pi/a}\int_0^{\pi}\int_0^{2\pi}\frac{\mid \mathbf{M}_{\left(\substack{\mathbf{q}_1\mathbf{q}_2\mathbf{q}_3\\ p_1p_2p_3}\right)}\mid^2}{\omega(\mathbf{q}_2)\omega(\mathbf{q}_1-\mathbf{q}_2)} \\ &\times \sin\phi q_2^2 \mathrm{d}\alpha\mathrm{d}\phi\mathrm{d}q_2 \\ &\times ([(n(\mathbf{q}_2)(n(\mathbf{q}_1-\mathbf{q}_2)+1)]\delta[\omega(\mathbf{q}_1)+\omega(\mathbf{q}_2)-\omega(\mathbf{q}_1-\mathbf{q}_2)] \\ &+ [(n(\mathbf{q}_2)+1)(n(\mathbf{q}_1-\mathbf{q}_2)+1)]\delta[\omega(\mathbf{q}_1)-\omega(\mathbf{q}_2)-\omega(\mathbf{q}_1-\mathbf{q}_2)]) \end{aligned} \quad (3.18)$$

where (as shown in figure 3.1) ϕ is the angle between $\mathbf{q}_1$ and $\mathbf{q}_2$ in the plane defined by them, and α is the angle with a plane parallel to $\mathbf{q}_1$, of which the probability calculation is independent.

3.4.1 Matrix element

The matrix element (M) is evaluated using equation 2.65; the parameters are taken from the vector diagrams and simplified. For $LA \leftrightarrow TA + TA$ transitions, using the vectors in figure 3.2, the matrix element is

---

[1] This approximation may result in a slight overestimation of the U-process scattering rate by the same degree of error as that associated with the volume difference. This also means that, when a U-process occurs, the maximum possible forward momentum will be subtracted leading to a further reduction of thermal conductivity.

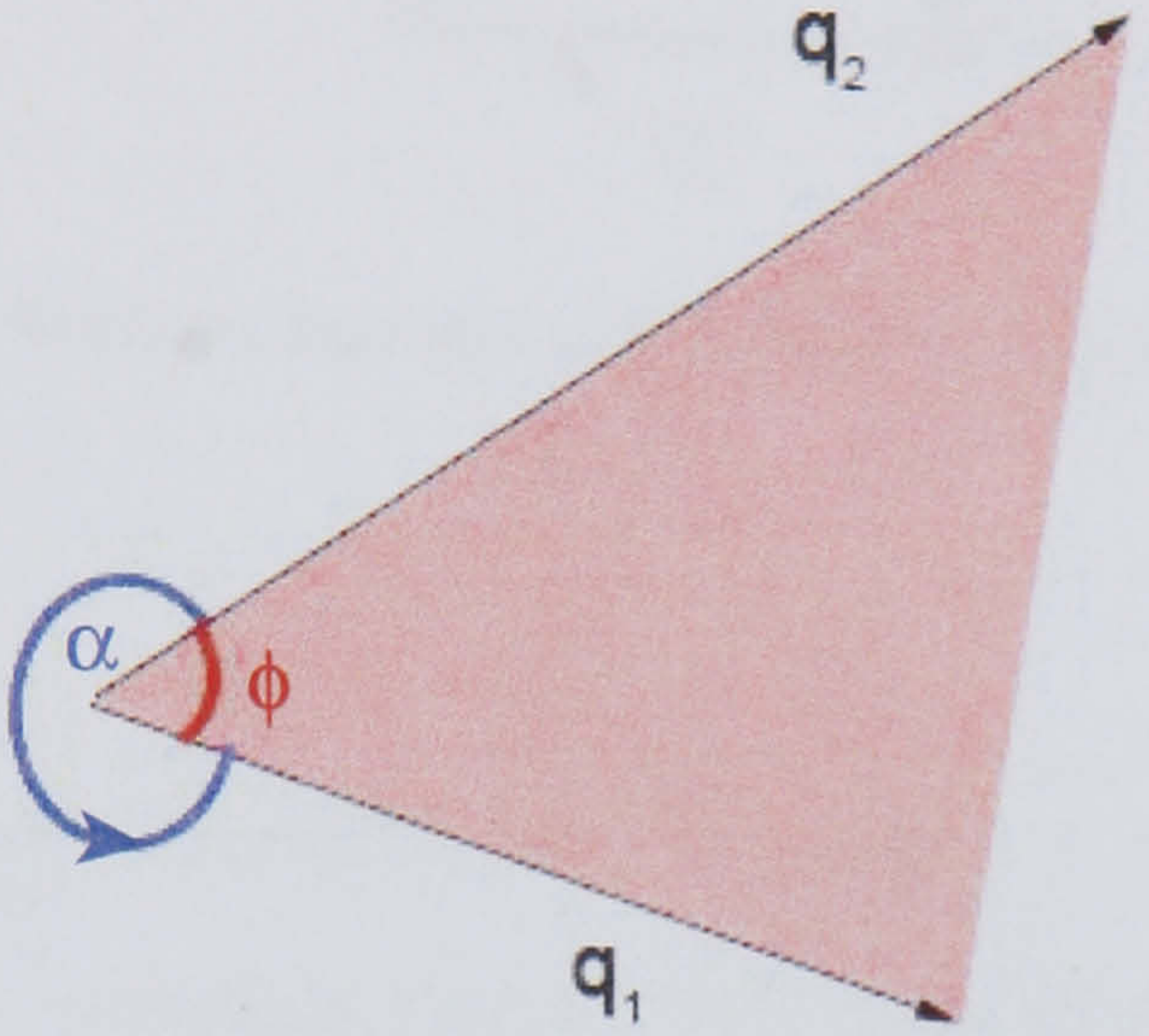

Figure 3.1: Angles used in probability calculation: α is the angle orthogonal to the plane spanned by $\mathbf{q}_1$ and $\mathbf{q}_2$. ϕ is the angle between $\mathbf{q}_1$ and $\mathbf{q}_2$.

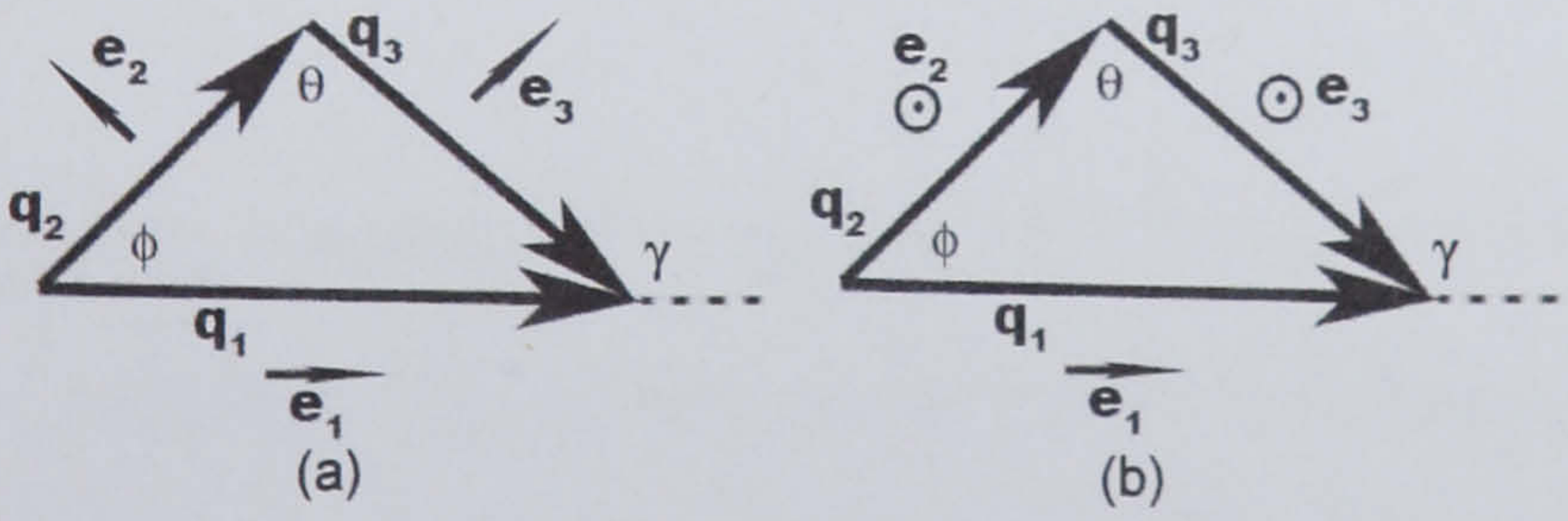

Figure 3.2: Vector diagrams for $LA(1) \leftrightarrow TA(2) + TA(3)$ transitions for the cases: (a) where the polarisations of the TA branches are in the plane spanned by $\mathbf{q}_1$, and $\mathbf{q}_2$ and (b) where the polarisations are orthogonal to this plane.

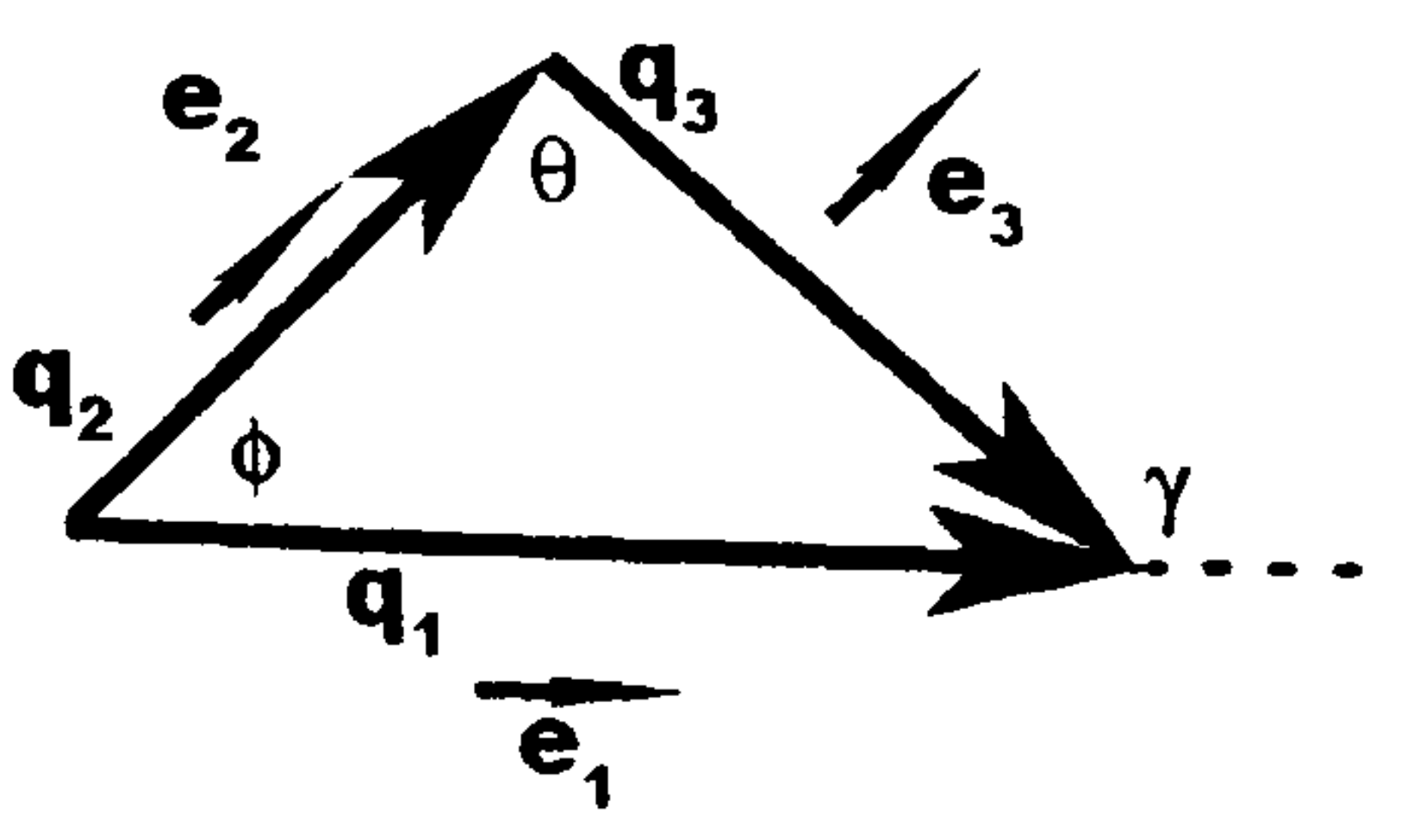

Figure 3.3: Vector diagrams for $LA(1) \leftrightarrow LA(2) + TA(3)$ transitions.

$$\begin{aligned} \mathrm{M}(a)_{\binom{LA,TA,TA}{q_1,q_2,q_3}} = q_1q_2q_3[&A_1\cos\gamma^2 + A_4\sin\gamma^2 + A_2(2\cos\theta\cos\gamma\cos\phi \\ &-\cos\theta\sin\gamma\sin\phi - 2\sin\theta\cos\gamma\sin\phi - \sin\theta\sin\gamma\cos\phi) \\ &+A_3(-\sin\theta\sin\gamma\cos\phi - \cos\theta\sin\gamma\sin\phi)] \end{aligned} \tag{3.19}$$

for (a) and

$$\mathrm{M}(b)_{\binom{LA,TA,TA}{q_1,q_2,q_3}} = q_1q_2q_3A_1\cos\gamma \tag{3.20}$$

for (b). For $LA \leftrightarrow LA + TA$ transitions, using the vector configuration shown in figure 3.3, the matrix element is

$$\begin{aligned} \mathrm{M}_{\binom{LA,LA,TA}{q_1,q_2,q_3}} = q_1q_2q_3[&(A_1 + A_4)(\cos\phi\sin\phi + \cos\gamma\sin\gamma) \\ &+(3A_2 + A_3)(\cos\theta\sin\phi\cos\gamma + \sin\gamma\cos\theta\cos\phi)] \end{aligned} \tag{3.21}$$

3.4.2 Elastic constants

The elastic constants used in the calculations that follow were taken from [70] see table 3.1.

Tamura [61] states that there are ambiguities in using these elastic constants, which

c_{11}	c_{12}	c_{44}	c_{111}	c_{112}	c_{123}	c_{144}	c_{155}	c_{456}
1.657	0.639	0.796	-7.43	-4.18	0.02	0.29	-3.15	-0.70

Table 3.1: Elastic constants taken from experiment for bulk silicon. Units:10^{12} dyn cm^{2}

are derived from anisotropic solids, to evaluate the constants in equation 2.65. Tamura goes on to redefine these constants, using a scheme previously adopted by Fedorov [48], to give a more natural definition of the isotropic elastic constants. He achieves this by minimising the quantity f using the formula

$$f = \sum_{i,j,k,l,m,n} \left(c'_{ijklmn} - c_{ijklmn}\right)^2, \tag{3.22}$$

where c_{ijklmn} is the elastic constant of a real solid and c'_{ijklmn} is that of the isotropic model.

With this scheme, the resulting elastic constants are:

$$\begin{aligned} A_1 &= \beta + \lambda \\ A_2 &= \gamma + \mu \\ A_3 &= \gamma \\ A_4 &= \beta \\ A_5 &= \alpha, \end{aligned}$$

where λ, and μ are Lamé constants while γ, α, and β are constants. These can all be expressed in terms of the elastic constants:

$$\begin{aligned}
\lambda &= \frac{1}{5}(c_{11} + 4c_{12} - 2c_{44}) \\
\mu &= \frac{1}{5}(c_{11} - c_{12} + 3c_{44}) \\
\alpha &= \frac{1}{35}(c_{111} + 18c_{112} - 16c_{123} + 19c_{144} + 2c_{166} - 12c_{456}) \qquad (3.23) \\
\beta &= \frac{1}{35}(c_{111} + 4c_{112} - 5c_{123} + 19c_{144} + 2c_{166} - 12c_{456}) \\
\gamma &= \frac{1}{35}(c_{111} - 3c_{112} + 2c_{123} - 9c_{144} + 9c_{166} + 9c_{456})
\end{aligned}$$

His calculations use the numerical values for λ, μ, β and γ in silicon, shown in table 3.2 below. α is unused in the calculations.

λ	μ	β	γ
5.24	6.80	-4.29	-9.45

Table 3.2: Tamura's elastic constant parameters for the anharmonic matrix element taken from [10]. Units 10^{11} dyn cm^{-2}

3.4.3 Energy conservation

The constant energy surface method used by Herring, Holland and Ziman to conserve momentum and energy is included directly in these calculations via the Dirac delta functions. Using the identity

$$\delta[g(x)] = \sum_i \frac{\delta(x - x_i)}{|g'(x_i)|}, \qquad (3.24)$$

where $g(x_i) = 0$, an expression has been derived for the scattering probability that can explicitly cater for energy conservation. If

$$g(\phi) = (\omega(q_1) - \omega(q_2) - \omega(|\mathbf{q}_1 - \mathbf{q}_2|)), \qquad (3.25)$$

where

$$|\mathbf{q}_1 - \mathbf{q}_2|^2 = q_1^2 + q_2^2 - 2q_1 q_2 \cos\phi. \tag{3.26}$$

an expression can be derived from this for $g'(\phi)$ using the dispersion relation. The results for the parabolic spline used in this work can be found in appendix E.2.

3.5 Phonon scattering

In order to satisfy the energy conservation for the scattering rate calculation, the following must be true:

$$q_3 = q(w_1 + w_2, p), \tag{3.27}$$

while for momentum conservation to be possible we ensure that

$$q_i \leq \sum_{i \neq j} q_j \tag{3.28}$$

so that vectors with magnitudes q_1, q_2, and q_3 can form a triangle in momentum space. For U-processes, the q-value which represents the LA phonon of the highest energy is replaced by the value $G - q$. The phonon scattering rate, using the two mode dispersion curve approximation, for the transition $\mathbf{q}_1(LA) \rightarrow \mathbf{q}_2(LA) + \mathbf{q}_3(TA)$ is

$$\begin{aligned} P_{LA \rightarrow LA+TA} &= \frac{\hbar}{8\rho^3 \pi \omega(q_1)} \sum_{q_2} \frac{|\mathrm{M}(\mathbf{q}_1, \mathbf{q}_2, \mathbf{q}_3)|^2}{\omega(q_2)\omega(q_3) g'(\phi)} \\ & \quad \times (n(q_2) + 1)(n(q_3) + 1) \\ & \quad \times q_2^2 \sin\phi \mathrm{d}q_2. \end{aligned} \tag{3.29}$$

For the transition $\mathbf{q}_1(LA) \rightarrow \mathbf{q}_2(TA) + \mathbf{q}_3(TA)$, it is

$$\begin{aligned} P_{LA\rightarrow TA+TA} &= \frac{\hbar}{8\rho^3\pi\omega(q_1)} \sum_{q_2} \frac{|\mathbf{M}(a)(\mathbf{q}_1, \mathbf{q}_2, \mathbf{q}_3)|^2 + |\mathbf{M}(b)(\mathbf{q}_1, \mathbf{q}_2, \mathbf{q}_3)|^2}{2\omega(q_2)\omega(q_3)g'(\phi)} \\ &\quad \times (n(q_2)+1)(n(q_3)+1) \\ &\quad \times q_2^2 \sin\phi \mathrm{d}q_2. \end{aligned} \tag{3.30}$$

For the transition $\mathbf{q}_1(LA) + \mathbf{q}_2(TA) \rightarrow \mathbf{q}_3(LA)$, it is

$$\begin{aligned} P_{LA+TA\rightarrow LA} &= \frac{\hbar}{8\rho^3\pi\omega(q_1)} \sum_{q_2} \frac{|\mathbf{M}(\mathbf{q}_3, \mathbf{q}_1, \mathbf{q}_2)|^2}{\omega(q_2)\omega(q_3)g'(\phi)} \\ &\quad \times n(q_2)(n(q_3)+1) \\ &\quad \times q_2^2 \sin\phi \mathrm{d}q_2. \end{aligned} \tag{3.31}$$

For the transition $\mathbf{q}_1(TA) + \mathbf{q}_2(LA) \rightarrow \mathbf{q}_3(LA)$, it is

$$\begin{aligned} P_{TA+LA\rightarrow LA} &= \frac{\hbar}{16\rho^3\pi\omega(q_1)} \sum_{q_2} \frac{|\mathbf{M}(\mathbf{q}_3, \mathbf{q}_2, \mathbf{q}_1)|^2}{\omega(q_2)\omega(q_3)g'(\phi)} \\ &\quad \times n(q_2)(n(q_3)+1) \\ &\quad \times q_2^2 \sin\phi \mathrm{d}q_2. \end{aligned} \tag{3.32}$$

Finally for transition $q_1(TA) + q_2(TA) \rightarrow q_3(LA)$, it is

$$\begin{aligned} P_{TA+TA\rightarrow LA} &= \frac{\hbar}{16\rho^3\pi\omega(q_1)} \sum_{q_2} \frac{|\mathbf{M}(a)(\mathbf{q}_2, \mathbf{q}_3, \mathbf{q}_1)|^2 + |\mathbf{M}(b)(\mathbf{q}_2, \mathbf{q}_3, \mathbf{q}_1)|^2}{2\omega(q_2)\omega(q_3)g'(\phi)} \\ &\quad \times n(q_2)(n(q_3)+1) \\ &\quad \times q_2^2 \sin\phi \mathrm{d}q_2. \end{aligned} \tag{3.33}$$

3.6 Results

3.6.1 Application of new relaxation times to Holland's thermal conductivity calculations

From Callaway's [32] calculations analysed in section 3.2.1, we can follow Holland's [11] approach to thermal conductivity calculations which separate the LA and TA contributions. The resulting equations are seen below:

$$\kappa_T = \frac{2}{3}\int_0^{\theta_T/T} \frac{C_T T^3 x^4 e^x (e^x - 1)^{-2} dx}{\tau_T^{-1}} \tag{3.34}$$

$$\kappa_L = \frac{1}{3}\int_0^{\theta_L/T} \frac{C_L T^3 x^4 e^x (e^x - 1)^{-2} dx}{\tau_L^{-1}}. \tag{3.35}$$

By using the above equations, with the relaxation times calculated by

$$\tau_T^{-1} = P_{TA+TA\rightarrow LA} + P_{TA+LA\rightarrow LA}, \tag{3.36}$$

$$\tau_L^{-1} = P_{LA\rightarrow LA+TA} + P_{LA\rightarrow TA+TA} + P_{LA+TA\rightarrow LA}, \tag{3.37}$$

a comparison for application to thermal conductivity can be drawn for the different sets of elastic constant data above, which can be seen in figure 3.4. A comparison is also made with Holland's relaxation time equations in 3.2.1. For this comparison, $\tau_{L/T}$ is derived from the anharmonic scattering term only.

Figure 3.4 shows considerable discrepancy in some of the solutions. The methods which match experimental results best are those from the calculation using Tamura/Hall's elastic constants, yet even these results deviate significantly below 50K. This can be attributed to the influence of other scattering events.

At low temperatures, the anharmonic scattering effect exponentially decreases and the effect of other scattering events, such as boundary scattering and impurity scattering, become more predominant. These effects are the main cause of low temperature thermal

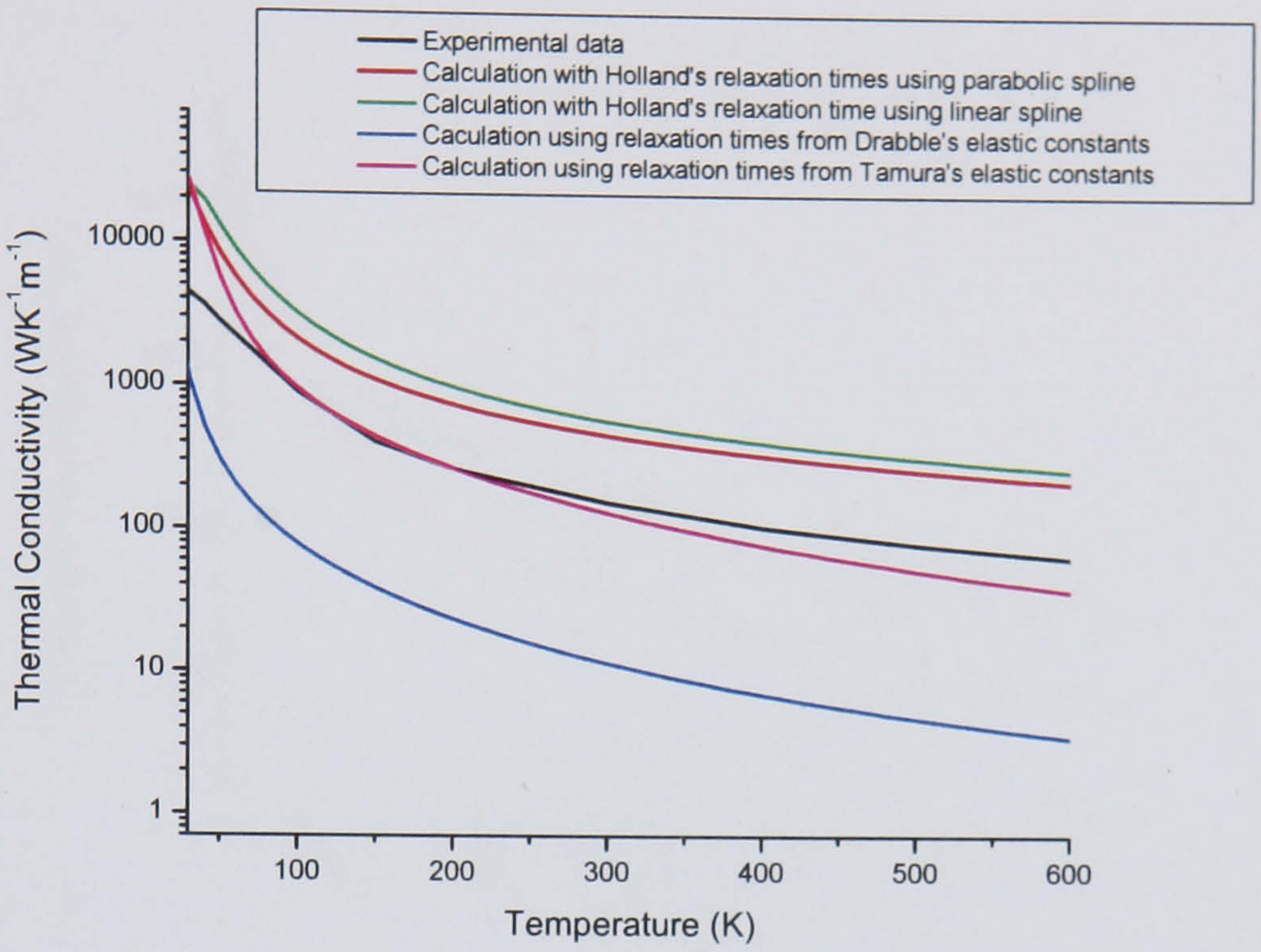

Figure 3.4: Comparison of various relaxation times calculations applied to the BTE with experimentally measured thermal conductivity of silicon from [6] and [7].

resistance.

The underestimation of the thermal conductivity calculation at high temperatures can be attributed to the elastic constants. Hall [10] observes that there is a temperature dependence for these values. In some cases negative third order elastic constants become positive at higher temperatures.

The calculation with Drabble's constants significantly underestimates thermal conductivity, which can be attributed to the anisotropy of the elastic constants. The results from Holland's relaxation time formulation show the validity of the anharmonic calculations in this work. The thermal conductivity curve from Holland's work shows that the calculation using Tamura/Hall's constants is accurate even at high temperatures.

Figure 3.4 also shows the effect of applying a more realistic dispersion relation to Holland's approximation. The result is a reduction in the calculated thermal conductivity, bringing it closer to experimentally recorded values.

In figure 3.5 the contribution of the various polarisation branches to thermal con-

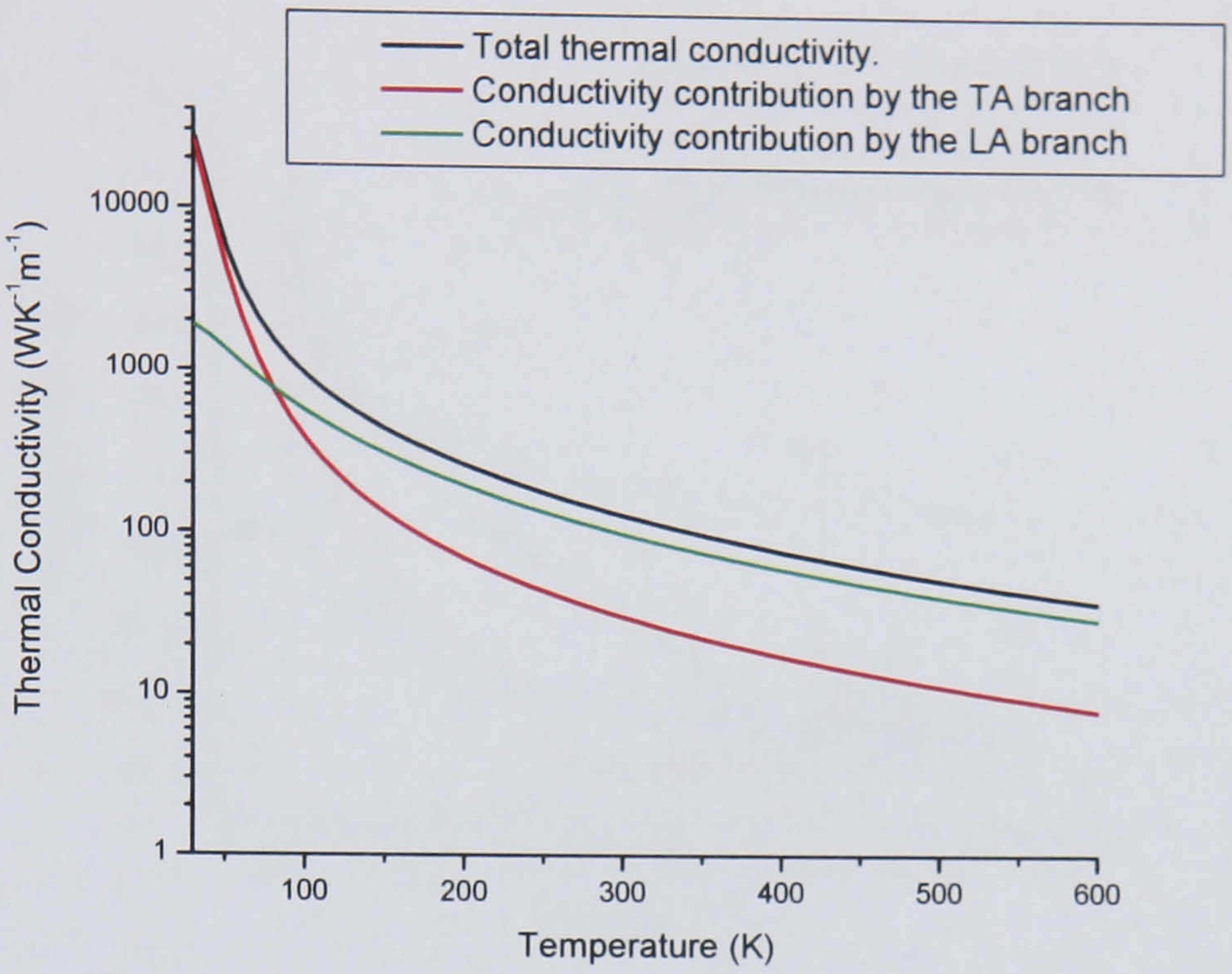

Figure 3.5: Comparison of the contribution of phonon polarisation branches to the thermal conductivity calculation using Tamura's elastic constants.

ductivity is shown. These results are from the calculations using Tamura/Hall's elastic constants. It can be seen that at low temperatures the primary heat transport branch is the TA. As temperature increases, the influence of the LA branch becomes dominant. This contradicts Holland's observations, in which he states that TA phonons are the dominant energy carriers at all temperatures. Interestingly, despite the larger numbers of TA phonons at high temperatures, LA phonons are the determining branch. The reason for this can be seen in the silicon dispersion curve in figure 2.6. The velocity of the LA branch across all wavevector space is higher than for the TA branch, and, as seen in figures 3.6 and 3.9, the relaxation time is greatest for low energy LA phonons at higher temperatures.

3.6.2 Phonon relaxation time

In figure 3.6, the phonon relaxation time for the LA phonon branch is shown. At higher temperatures (300K in this case) when compared to Holland's approximation, there is

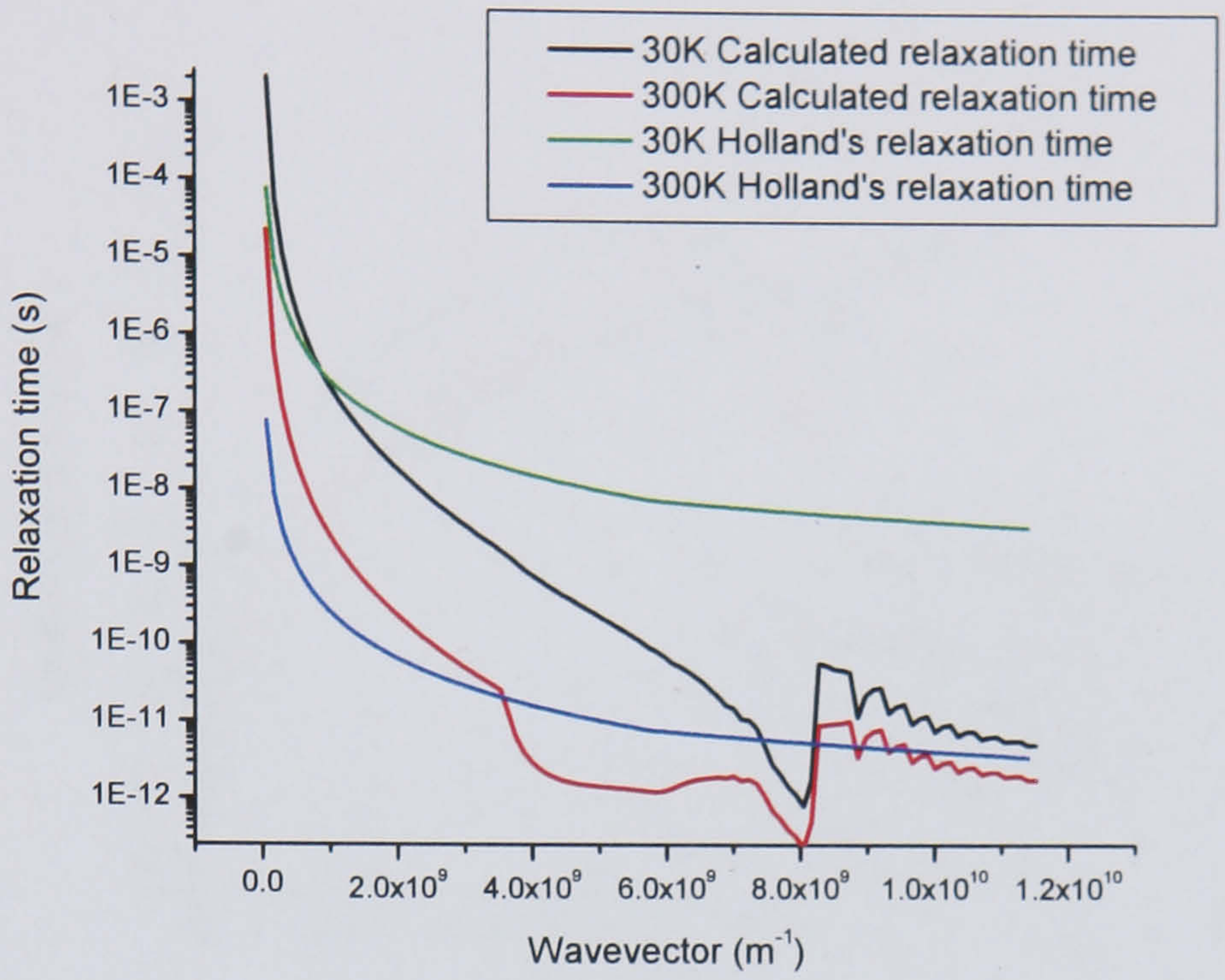

Figure 3.6: Phonon relaxation time for calculation compared to Holland's approximation for LA phonons.

a significant difference in the values. Holland's model overestimates scattering at low energies, and underestimates it in the midrange. Figure 3.7 shows the breakdown of the scattering probabilities. Analysis of this graph reveals that the effect of U-processes is significant, and Holland's approach to them (section 3.2.1) does not properly represent their influence. The U-process for $LA \rightarrow TA + TA$ causes a significant spike in the relaxation time curve due to the plateau in the TA dispersion curve at the end of the Brillouin zone. The discontinuity after this spike is because further transitions of this type are energetically impossible. It can also be seen that at high temperatures, the $LA + TA \rightarrow LA$ is the dominant process for low energy phonons. Figure 3.6 shows an oscillation at high wavevectors; figure 3.7 shows this is a result of the calculation done for U-processes of the $LA \rightarrow LA + TA$ transition. This is an effect of the discretisation of wavevector space and the maximum TA energy prohibiting certain transitions.

Figure 3.6 also shows that Holland's approximation grossly overestimates the relaxation times of high energy LA phonons at low temperatures. Here the predominant scattering events are the spontaneous decays shown in figure 3.8.

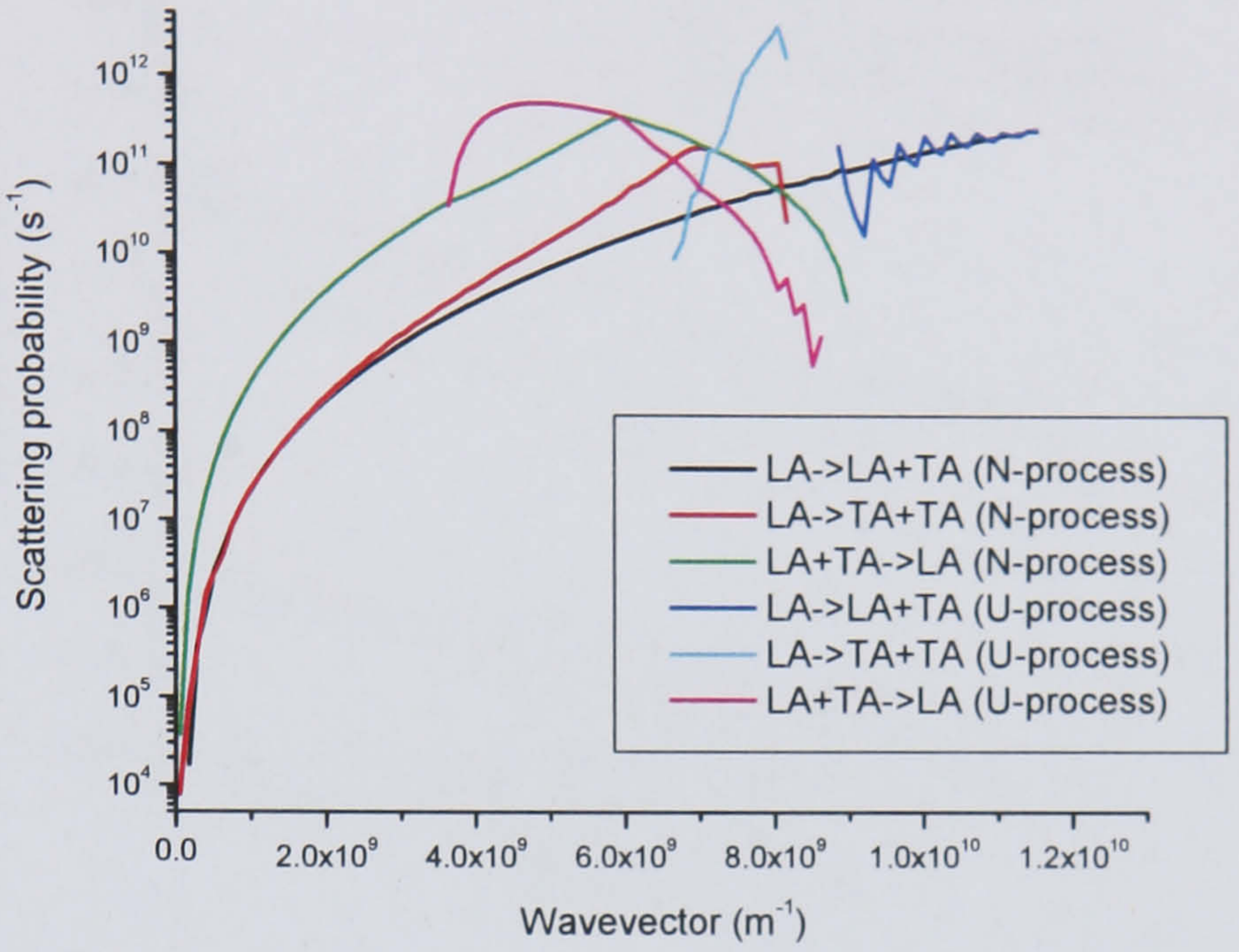

Figure 3.7: The individual phonon scattering probabilities for the LA phonon branch at 300K.

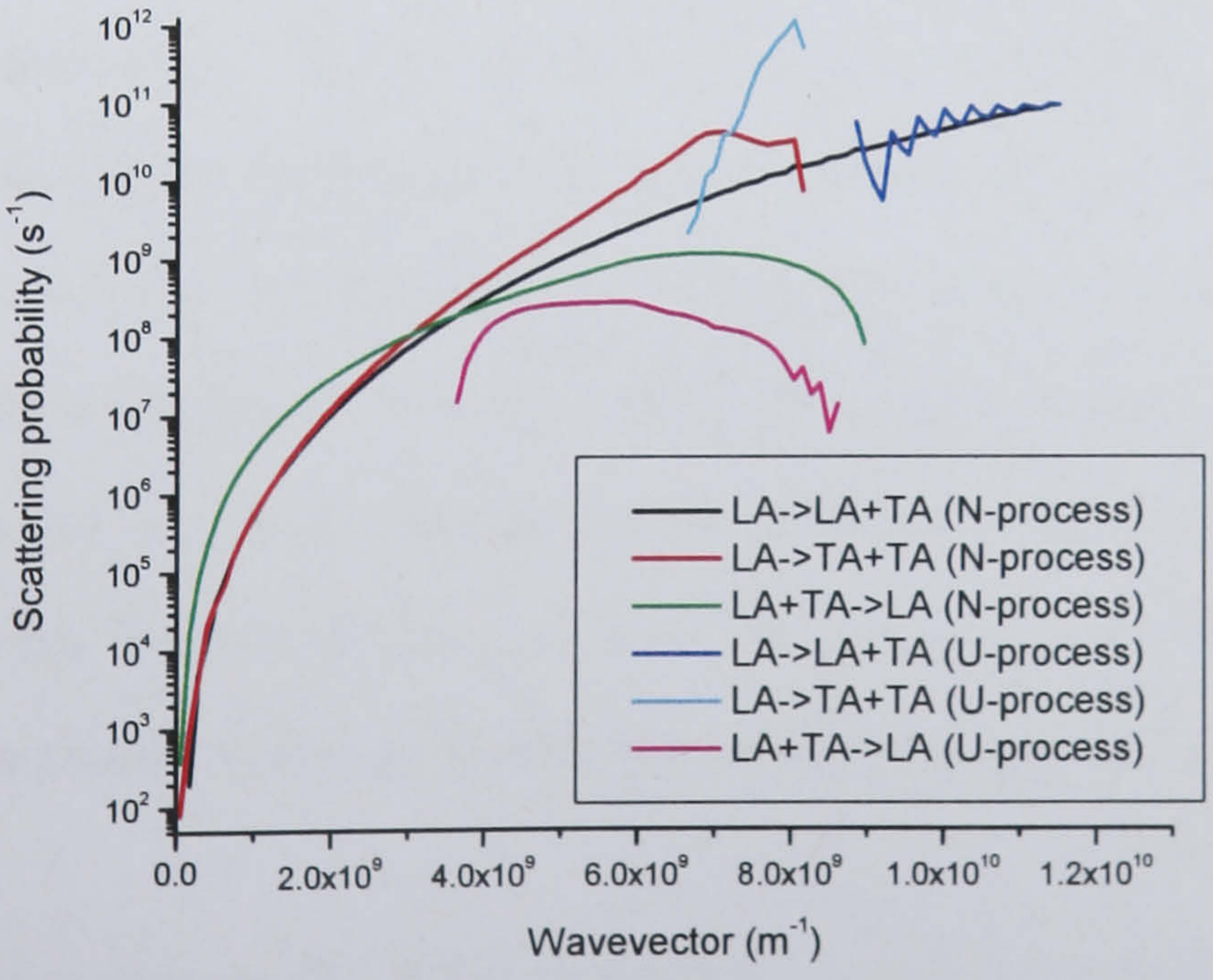

Figure 3.8: The individual phonon scattering probabilities for the LA phonon branch at 30K.

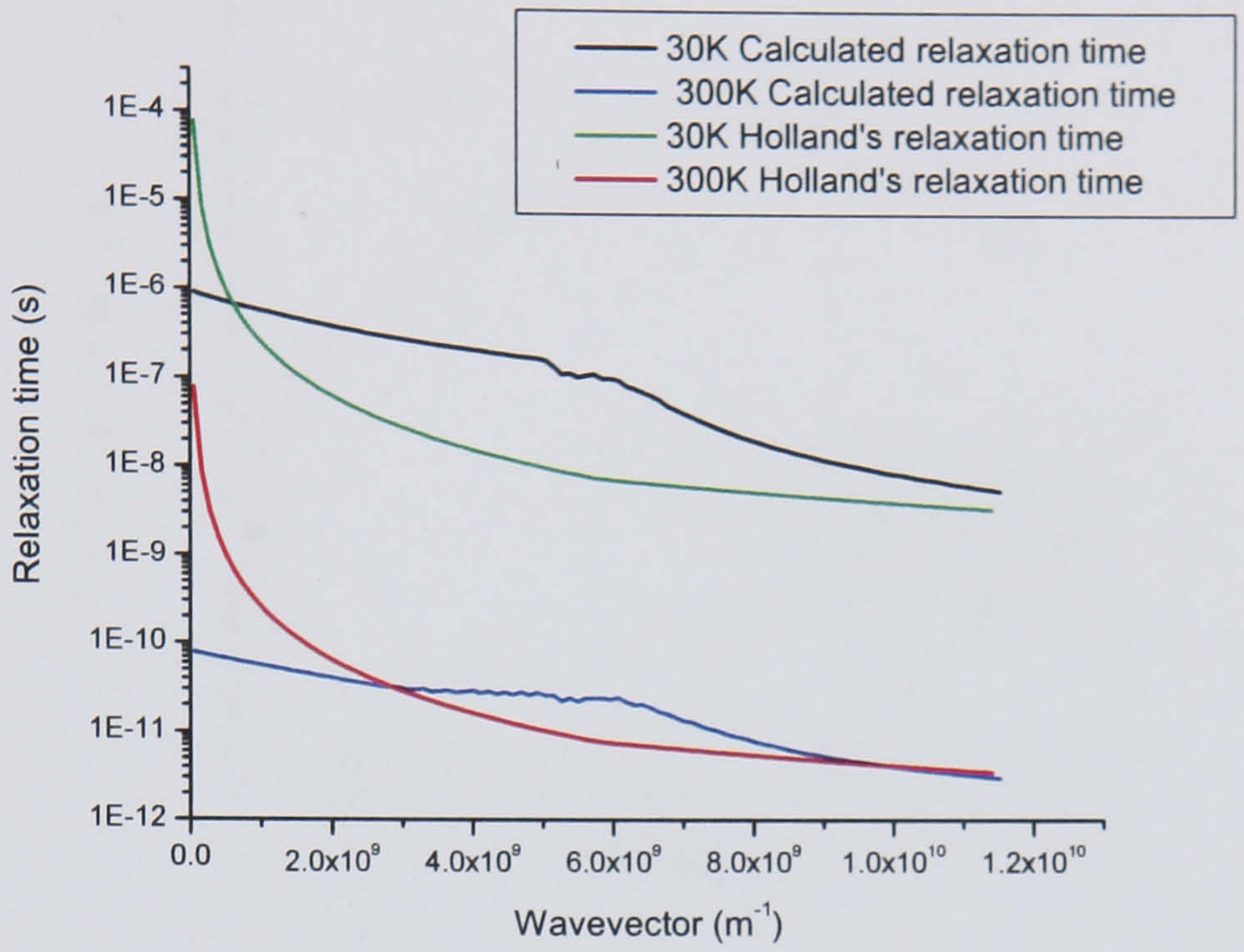

Figure 3.9: Phonon relaxation time for calculation compared to Holland's approximation for TA phonons.

Though the contribution of the TA branch to thermal conductivity is small at high temperatures, this branch still contributes to heat transport. The TA branch scattering events are the limiting process for LA phonon transport because they determine the occupation of LA phonon states. Figure 3.9 shows that the calculated relaxation times are relatively close to Holland's formulation at low temperatures. At higher temperatures the relaxation time is longer, accounting for the drop in thermal conductivity.

Figure 3.9 shows a significant deviation from Holland's approximation at low energies. This is due to the two mode approximation involved; the higher energy LA branch means that low energy TA transitions are more likely to occur via the $TA + LA \rightarrow LA$ process. This is illustrated in the scattering probability graphs in figures 3.10 and 3.11.

Holland [11] states that in the TA branch there would be no frequency dependence for the Umklapp scattering. The effect can be seen in figure 3.9, however due to the revised elastic constants this approximation is no longer valid. Figures 3.10 and 3.11 show that at high frequencies the dominant scattering process is the $TA + TA \rightarrow LA$

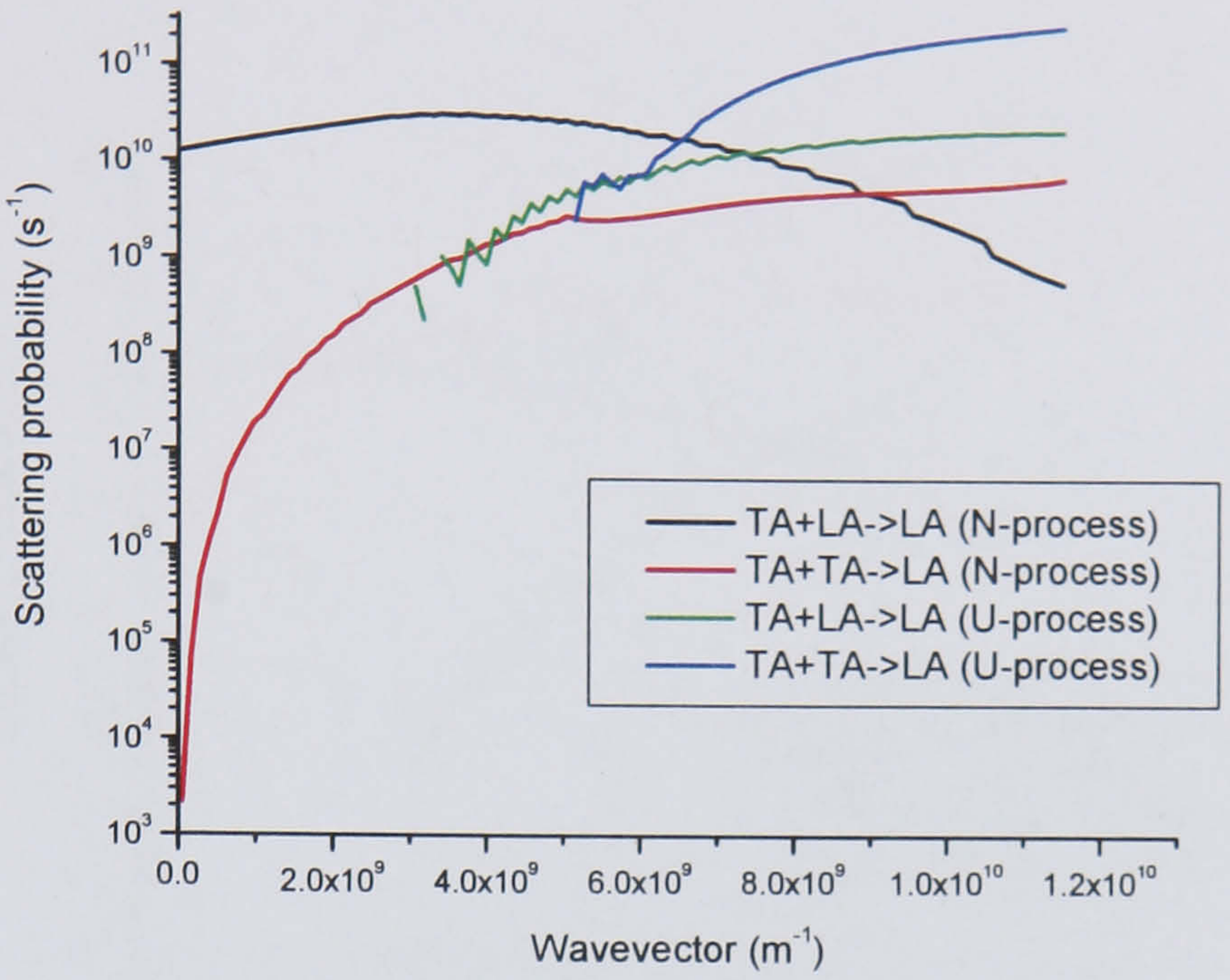

Figure 3.10: The individual phonon scattering probabilities for the TA phonon branch at 300K.

Umklapp process. This contradicts work done by Orbach [30] in which perturbation techniques show that $TA + LA \rightarrow LA$ dominates. Orbach's solution does hold for low frequency TA phonons, but the influence of these scattering events decreases with temperature.

3.6.3 Influence of Umklapp scattering

Umklapp scattering is the primary scattering event which provides thermal resistance in a pure crystal. The graphs in section 3.6.2 show that the overall scattering rate decreases with decreasing temperature. As our interest is in the thermal conductivity of the material, a useful indication of the influence of the U-processes is seen in Figure 3.12. This graph shows that at lower temperatures the overall effect of U-processes is reduced. This contributes to the rapid increase of thermal conductivity at low temperatures seen in figure 3.4. An interesting point of note in figure 3.12 is that there is a peak U-process influence at approximately 75K for LA phonons and about 50K for TA phonons, the effect coincides with a plateau in thermal conductivity seen in the thin

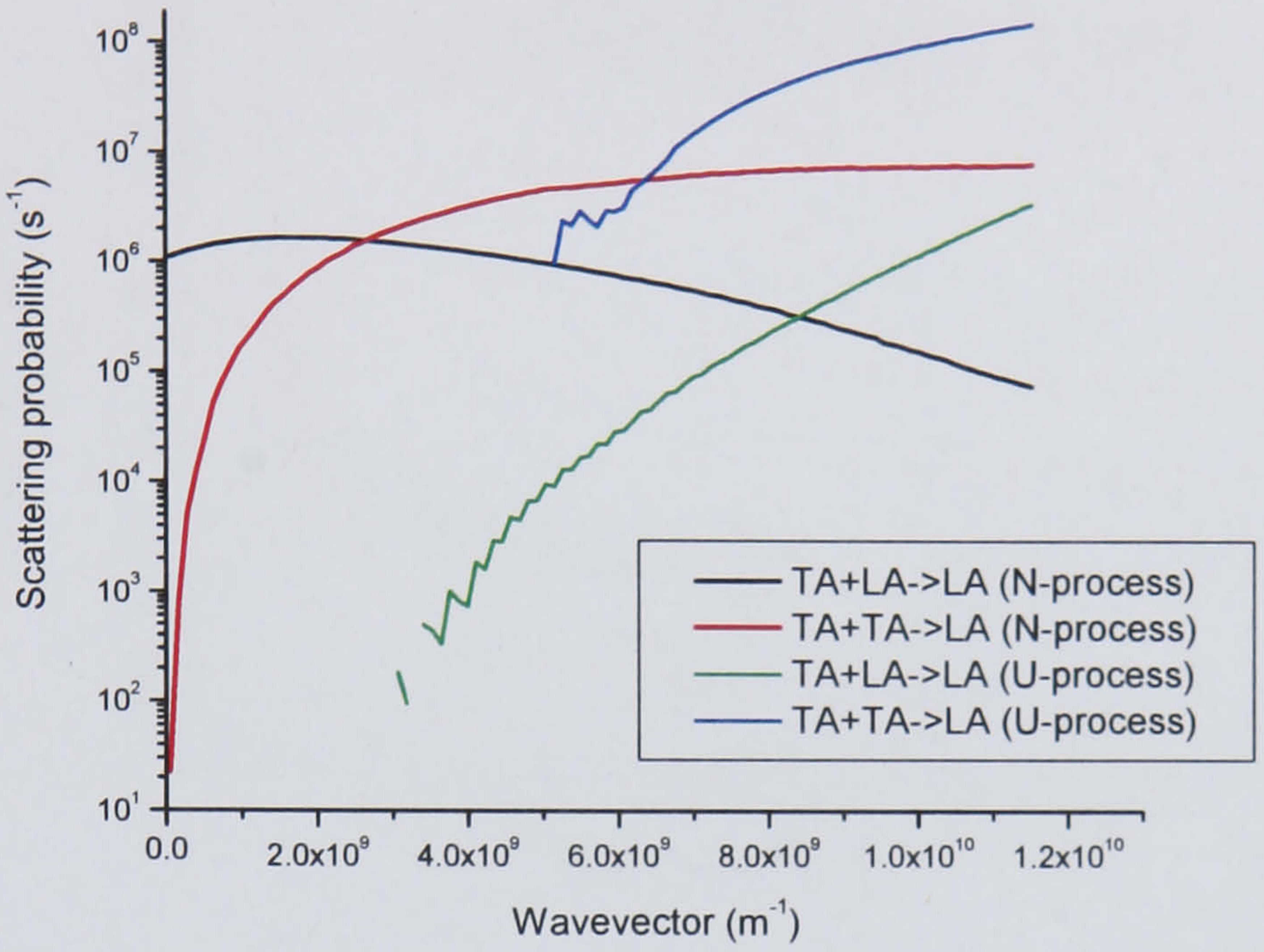

Figure 3.11: The individual phonon scattering probabilities for the TA phonon branch at 30K.

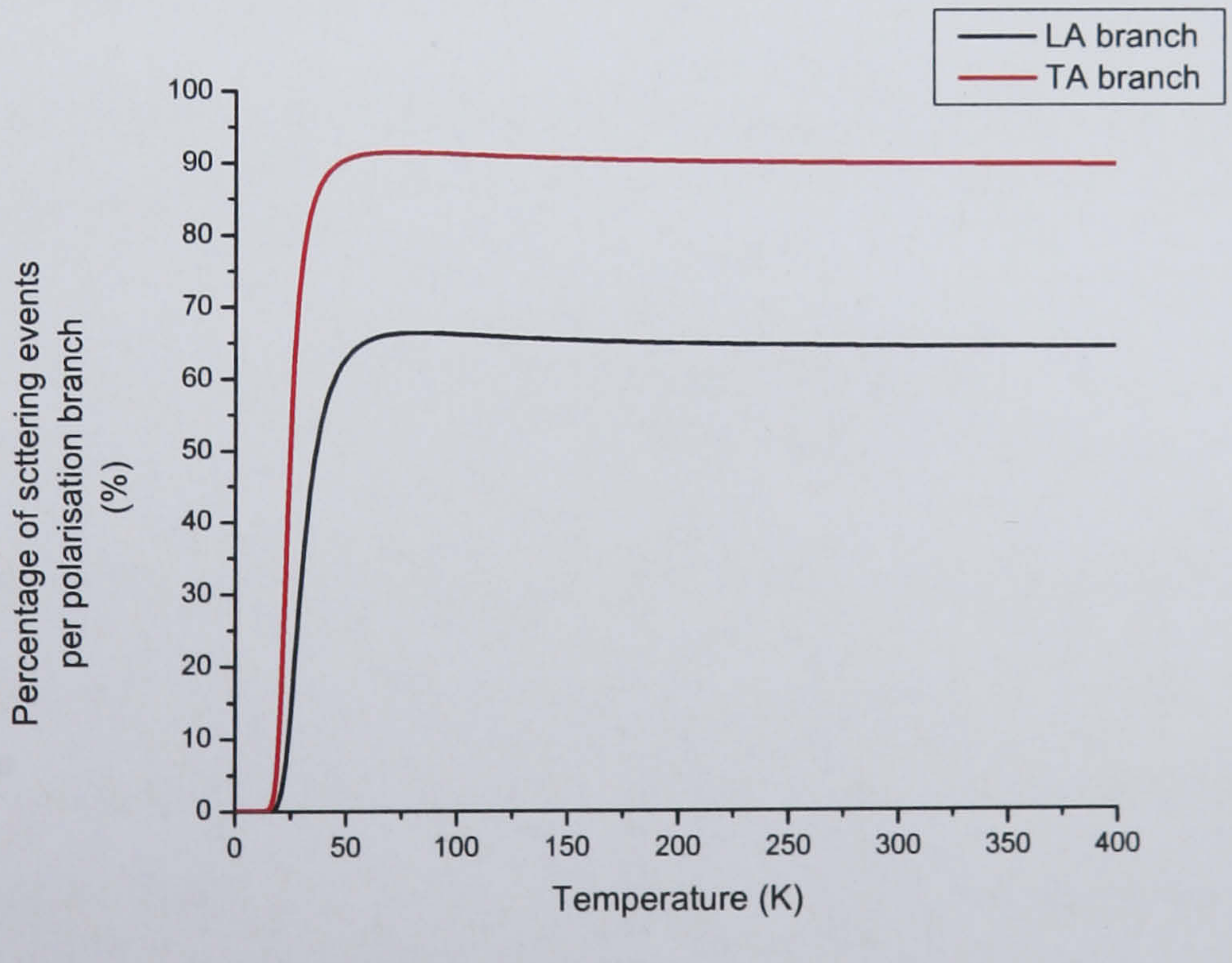

Figure 3.12: The effect of temperature variation on the percentage of Umklapp scattering events at equilibrium.

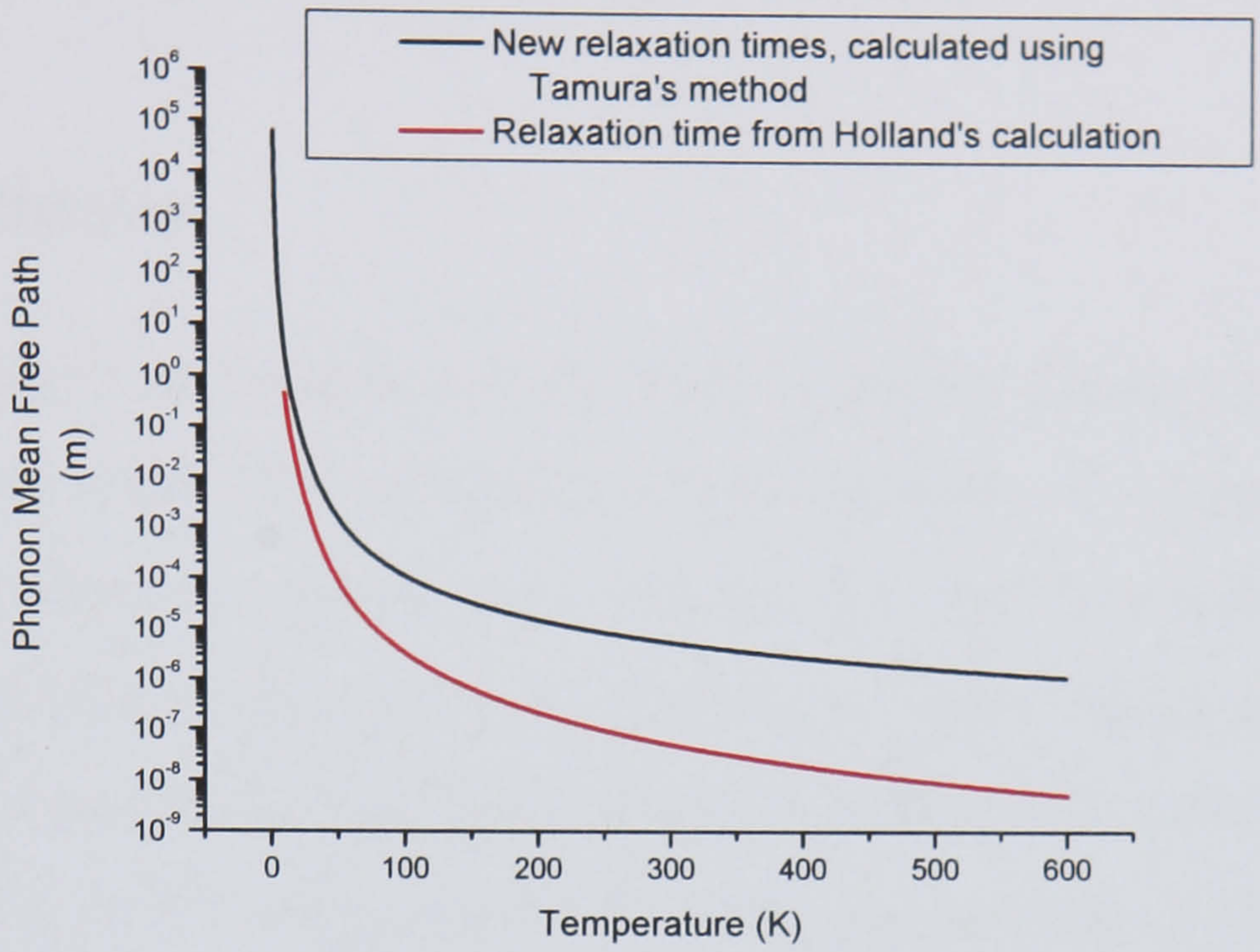

Figure 3.13: The phonon mean free path for various temperatures and relaxation time calculations.

film measurements of Asheghi [8].

3.6.4 Mean free path

From the relaxation times above, and using the dispersion curve, the expression for the mean free phonon path ($\bar{l}$) is

$$\bar{l} = \frac{\sum_{q,p} \langle n(q,p) \rangle D(q) \tau(q,p) v(q,p)}{\sum_{q,p} \langle n(q,p) \rangle D(q)}, \tag{3.38}$$

the results of which can be seen in figure 3.13. The mean free path is a good indication of the limit of accuracy for an analytical solution described in section 3.6.1. As stated in section 1.3, an analytical solution can only be used on length scales greater than the mean free path. Figure 3.13 shows that this range at room temperature is on the micronscale, justifying the requirement for a more comprehensive solution for modern semiconductor devices. It can also be seen that Holland's approach overestimates the usefulness of this model due to the small mean free path values that it predicts. The higher relaxation times for TA phonons explain this difference.

3.7 Summary

The new formulation for relaxation times seems to provide a more experimentally accurate result over Holland's relaxation time approximation. The formulation goes on to predict very different scattering rates, showing that there is a significantly greater influence of the Umklapp processes than estimated in Holland's approach. The effect of these processes is an increase in thermal resistance. Additionally the model goes on to show that the $TA + TA \leftrightarrow LA$ process influence is underestimated in Holland's description, especially the effect of this process on the LA phonon relaxation time. The mean free path of the phonons is significantly different as well due to the change in relaxation time, with the new model predicting much higher values.

Chapter 4

Monte Carlo simulation solutions

4.1 Introduction to Monte Carlo methods

Monte Carlo (MC) methods are stochastic computational algorithms that are often used to solve complex mathematical or physical systems. These methods can be used to find solutions to mathematical problems that have many dependencies and coupled degrees of freedom. The use of MC methods involves creating a stochastic description of the system which is being analysed and is particularly useful in order to solve systems which have a degree of uncertainty associated with them.

Emulation of the real physical system in the MC method is attained by the use of probabilities of events occurring within the system and the use of random numbers to affect these events. The model thus replicates the behaviour of the system undergoing changes in the characteristic distribution function of the system as they would occur in real time. The MC simulation can use different techniques to achieve this: the metropolis technique, which is a "rejection-acceptance algorithm" where changes to a distribution are applied to achieve a target distribution by using some criteria such as energy minimisation; and the trajectory or particle method, which involves simulation of particles while monitoring their movements and changes. Monte Carlo simulations have found use extensively in finance modelling [71], manufacture process modelling [72], semiconductor growth modelling [73], electronic transport modelling [74] as well as a range of other applications.

There are two main ways in which the MC simulation can be implemented [74]: the time averaging technique and the ensemble technique. The latter employs the use of a single sample (such as a representative carrier) and affecting stochastically chosen events on it (scattering events in the case of a carrier). The sample is monitored over time and an average representation of the sample can be determined. The ensemble technique utilises a representative population of samples and affects stochastic events across the whole population. This method is useful to analyse transient states in a system.

4.2 Monte Carlo modelling in semiconductors

The basic MC transport model follows the trajectory of a particle though real space. The particle has classical characteristics of a unique position and momentum (wavevector). The particle is then tracked through time with the application of appropriate drift and scattering events. The duration of drift, selection of scattering process and the effect of the scattering events are determined by probabilities and random numbers. Thus the stochastic nature of the MC simulation arises. Simulating an ensemble of particles or tracking the path of a single particle over a long period of time in order to give a large sample of alternating drifts and scattering events can provide a semi-classical representation of a real system and generate a solution for the BTE.

The noise that arises from the use of random numbers mimics the variations that can occur in a real system, and thus can provide a better description of transience in the system. Other techniques have to explicitly include a noise factor, whereas the MC solution has the benefit of it being implicitly included. This is sometimes seen as detrimental as the simulation often has to be run for long periods or use very large ensembles in order to reduce the artificial stochastic noise in order to extract a steady state result.

The main advantage of the MC method over other BTE solution methods is that there is no assumed form of the distribution function. This means that a system in a highly non-equilibrium state can still be solved and transient properties can also be extracted.

4.3 Monte Carlo and phonons

Very few attempts have been m ade to solve the BTE for phonons. In its regular form the BTE is difficult to solve analytically for realistic phonon dispersions, densities of states, anharmonic interactions and irregular geometries without significant approximations. This is because the number of dependant variables is too large, and would render any discretisation scheme too complex [26]. As discussed above, the MC method overcomes some of these difficulties.

Klitsner [75] has used a MC simulation to look at low temperature surface scattering but did not consider phonon-phonon interactions. Without inclusion of anharmonic interactions his model will not predict accurate results at high temperatures. Peterson [76] performed a Monte Carlo simulation for phonons in the Debye approximation with a single relaxation time. More recently Mazumder [36] extended Peterson's idea to include the simulation of dispersion and two different acoustic phonon modes. This method is described in more detail below.

4.4 Non-momentum conservation Monte Carlo simulation

An attempt to formulate a Monte Carlo solution to the BTE for phonons has been published by Mazumder [36]. Mazumder's method uses a simplistic approximation of anharmonic interactions (described in section 4.4.4) which does not conserve momentum. His simulation does however provide a significantly better representation of phonon movement than previous work. Whilst the aim of this work is to provide a more comprehensive MC solution to the phonon transport problem, adoption of Mazumder's method was decided upon as a good starting point.

4.4.1 Core algorithm

Mazumder's method uses an ensemble simulation of phonons in a material, in which phonons are tracked individually. In each case the phonon movement is monitored along with interactions with other phonons, boundaries and impurities. The transport characteristics are emulated by allowing interaction at consant time steps. This time step has to be smaller than the smallest phonon relaxation time. At each time step phonon positions and lifetimes are synchronised and can be used to calculate the local temperature and phonon distribution. If a phonon-phonon interaction occurs within the time step (determined by the relaxation time) the phonon in question is removed from the simulation and the energy added back into the simulation using the scattering method described in section 4.4.4 below. Figure 4.1 shows a simple flow diagram of the method used.

4.4.2 Initial conditions

The simulation domain is populated with a number of particles which represent the total phonon population in the material. The real population of phonons (determined by equation 2.38) in a material is an extremely large number (for instance in a volume of material of 3 μm^3 at 300K, there are approximately 1.8×10^{11} phonons) and hence computationally impossible to simulate directly. Therefore a scaling factor S is used to represent the phonon population adequately. This is determined from a prescribed

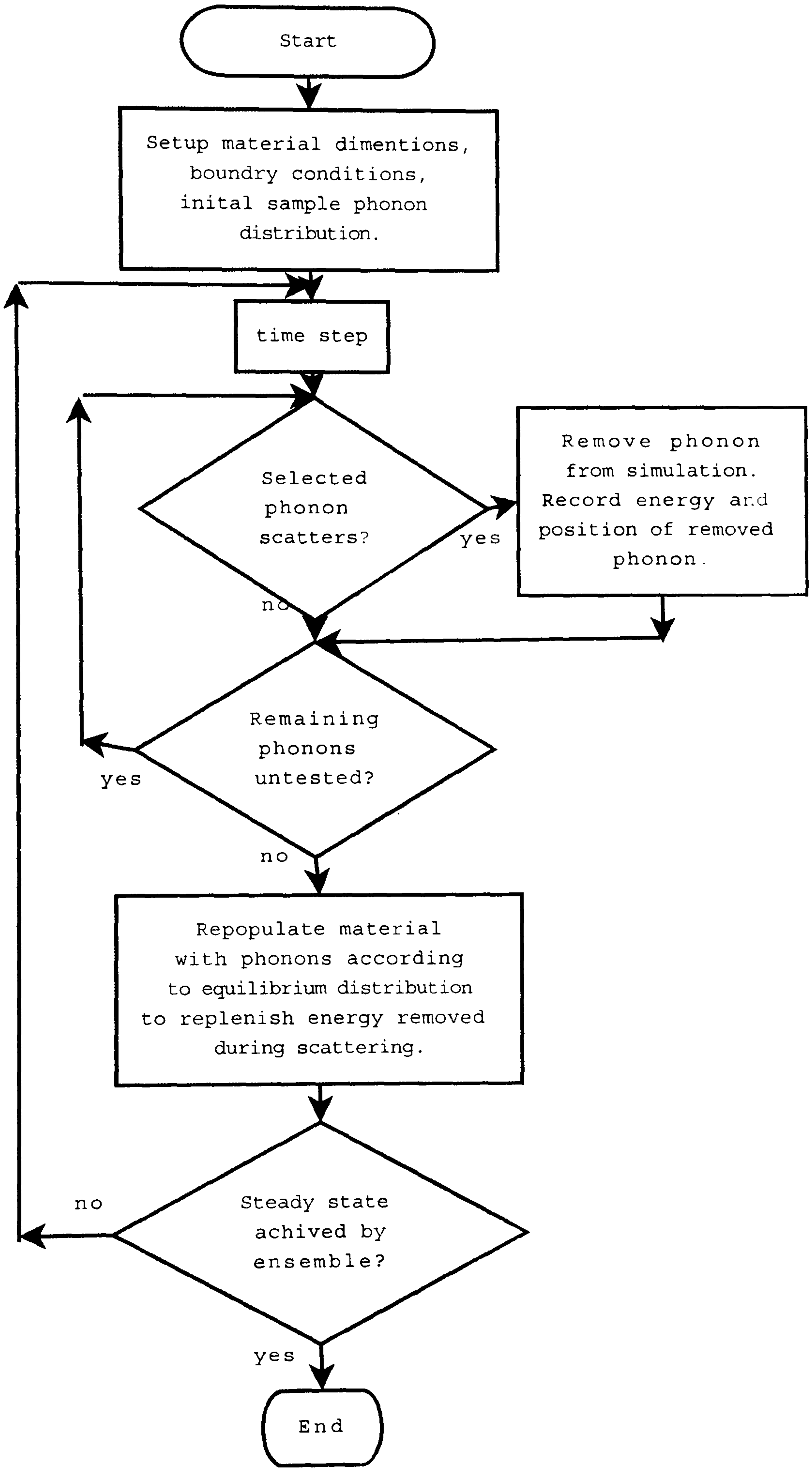

Figure 4.1: Flow diagram for Mazumder's Monte Carlo simulation.

number of particles for simulation as

$$S = \frac{N_{actual}}{N_{prescribed}}, \tag{4.1}$$

where N_{actual} is the computed population and $N_{prescribed}$ is the number of particles at the start of the simulation. S is used throughout the simulation for each stochastic sample. During the course of the simulation the number of representative particles will vary.

To derive a sample population from a continuous distribution using the dispersion curves would be complex. A way to avoid this complexity is to define discrete spectral intervals in frequency space. This is done by taking the maximum energy of the LA phonon ($\omega_{max,LA}$) and dividing it by a set number,

$$\Delta\omega_i = \omega_{max,LA}/N_b \tag{4.2}$$

where N_b is the number of frequency intervals and $\Delta\omega$ is the discrete frequency spacing.

The number of phonons in a spectral interval per unit volume is given by

$$N_i = n(\omega_i, LA)D(\omega_i, LA)\Delta\omega + 2n(\omega_i, TA)D(\omega_i, TA)\Delta\omega \tag{4.3}$$

where the discrete population, N_i, is evaluated using the centre frequency of the spectral interval, hence the total phonon population is

$$N_{total} = \sum_{i=\frac{\Delta\omega}{2}}^{\omega_{max,LA}} N_i \tag{4.4}$$

When populating the simulation with particles and determining the polarisation and energy of each added particle, the probability for its existence is calculated as

$$P_i(\omega_i, LA|TA) = \frac{n(\omega_i, LA|TA)D(\omega_i, LA|TA)\Delta\omega}{N_{total}}. \tag{4.5}$$

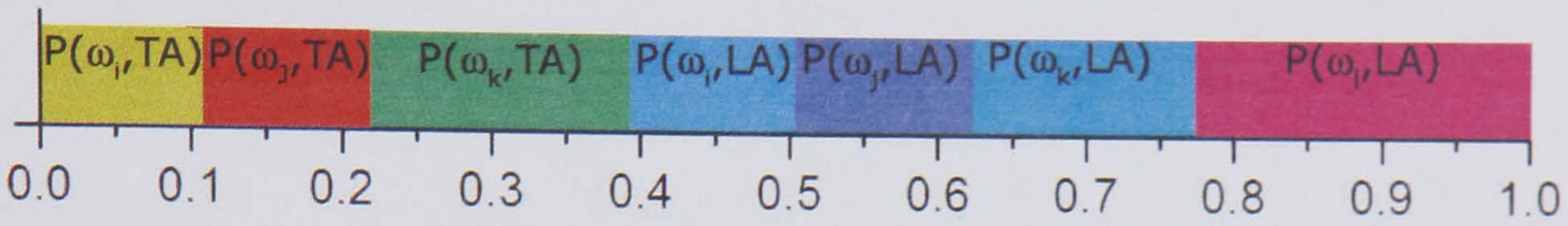

Figure 4.2: Illustration of the probability ladder for the phonon population scheme.

A ladder of probabilities is created (seen in figure 4.2[1]) and a random number, r, between one and zero is generated. The phonon whose probability occupies that value of r in the ladder will be added to the simulation. This process is repeated until the required total energy is reached.

The positioning of phonons as they are generated is done by setting coordinates within the material. To distribute phonons equally throughout the material, the position coordinates are assigned randomly:

$$\mathbf{r} = s_1 x_{max} + s_2 y_{max} + s_3 z_{max} \tag{4.6}$$

where $\mathbf{r}$ is the positional vector, s_1,s_2,s_3 are random numbers between one and zero, and x_{max}, y_{max}, z_{max} are the maximum coordinates for the material defined by the boundaries.

Once the frequency of the particle is known, the wavevector can be determined. As with the calculations in chapter 3 some simple assumptions must be made. In this case we also assume that the dispersion relation is isotropic and that the dispersion relation follows the form shown in appendix E.2 which is an approximation of the relation shown in figure 2.6. Once the scalar value of the wavevector has been determined the vector is determined by multiplication with a randomly generated unit vector. Generation of these vectors can be seen in appendix D.

To monitor localised temperature, the material is divided into cubic cells (as shown below in figure 4.3). The local temperature in the cube (or cell) is determined by the

---

[1] In the simulation there are significantly more steps in the probability tree. For illustration purposes figure 4.2 only has a small number of steps.

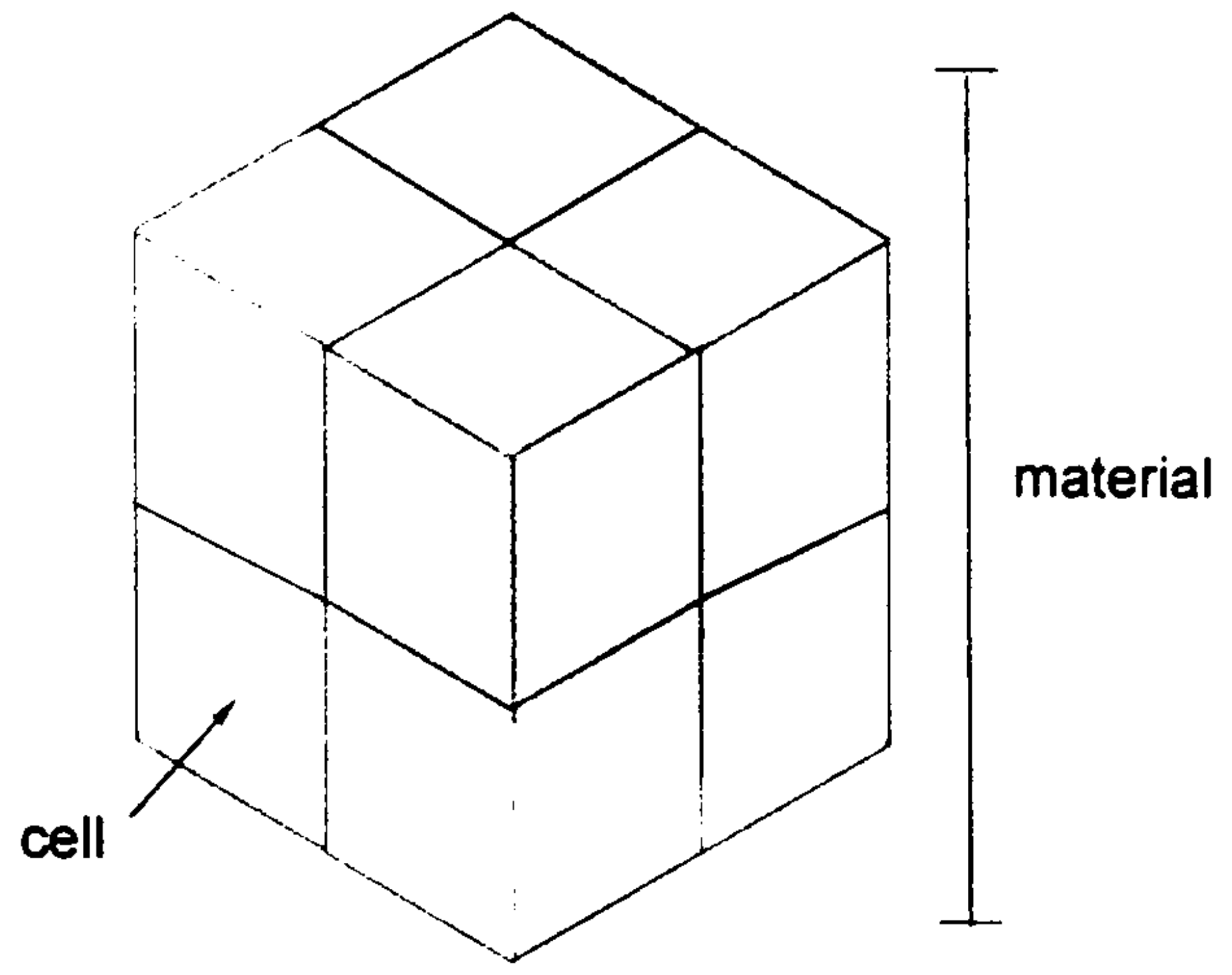

Figure 4.3: Spatial cells used to build the material for simulation.

energy contained[2]. The size of the cells can be varied in order to increase the resolution of the simulation. Increasing the resolution can result in a finer local temperature mesh but with smaller cells: each cell will have a smaller particle population and, as a result, a less accurate representation of local temperature.

As the sample phonon distribution in a cell is not fully representative of an equilibrium distribution, the approximation in section 2.7 is employed. The temperature of the cell is defined by comparing the energy of the cell with the phonon energy at equilibrium (defined by equation 2.38). To increase the calculation speed, a spline is used to represent the resultant curve as described in appendix E.1.

4.4.3 Phonon movement

Phonons have a group velocity determined by the dispersion curve (section 2.2.9). This movement is modelled by adding a displacement vector to the position vector, $\mathbf{r}$, of each sample phonon at each time step.

$$\mathbf{r}(t+\Delta t)=\mathbf{r}(t)+\mathbf{v}_g\Delta t \tag{4.7}$$

---

[2] Mazumder uses a tetrahedral cell for his 3D structures: this was dismissed due to the increase in computational complexity that would be involved. The advantage of using tetrahedral cells is that, when constructing complex shapes, the tetrahedral shape offers more flexibility, however for simple structures the cubic cells are sufficient.

At the end of each time step the phonon is assessed to determine whether it participates in a scattering event.

4.4.4 Scattering mechanism

When a phonon is tested for scattering, the phonon relaxation time from Holland's [11] work is used. The relaxation time is calculated using the formula seen in section 3.2.1 for each phonon, using the temperature of the cell containing the phonon. If

$$r < \left(1 - e^{-\frac{\Delta t}{\tau_{p,T}}}\right) \tag{1.8}$$

the phonon scatters, where r is a random number between one and zero, τ_p is the relaxation time of the phonon, and T is the local temperature. The phonon energy is then recorded and the phonon removed from the simulation. The energies of scattered phonons are associated with the cells they were in at the time of scattering. Once all the phonons in the material have been tested for scattering and all the removed energies compiled, phonons are introduced to the simulation according to an equilibrium distribution determined by the temperature of the cell, using the same scheme as for the initialisation population (see section 4.4.2). Phonons are created at random positions in each cell, until the energy lost by phonon scattering is replaced within a set tolerance.[3]

4.4.5 Boundary conditions

In order to simulate the heat transport in any contained system such as a semiconductor structure, boundary conditions are very important. In this solution, several boundary conditions have been implemented to model different structures. The boundary conditions are detailed below.

The isothermal wall is analogous to a black wall for phonon radiation. The wall

---

[3] Mazumder uses $\hbar\omega_{max,TA}$ as the tolerance, which he determines from a trial and error method. This value is also adopted in this work.

emits phonons into the structure based on the phonon flux from a body with constant temperature. Phonons which collide with this boundary are thermalised (similar to black body absorption).

The phonon emission is simulated in a similar way to the initialisation described in section 4.4.2. The phonon emission rate is calculated using the group velocity $\mathbf{v}_g$ to calculate the phonon flux:

$$N_{face,i} = A\Delta t(\mathbf{v}_g \cdot \hat{\mathbf{n}})N_i \tag{4.9}$$

where N_{face} is the number of phonons entering the material from an isothermal wall with area A during the time step Δt and $\mathbf{v}_g \cdot \hat{\mathbf{n}}$ is the group velocity normal to the face of the wall. The total energy, E_{face} for injection is calculated from this by

$$E_{face} = \sum_{P} \sum_{i=\frac{\Delta\omega}{2}}^{\omega_{max,LA}} \hbar\omega_i N_{face,i}. \tag{4.10}$$

Phonons are then randomly added into the simulation using a similar probability scheme to that described for the initialisation of the phonon population. The probability of a phonon being injected into the material is

$$P_{i,face}(\omega_i, LA|TA) = \frac{N_{face,i}}{N_{face,total}} \tag{4.11}$$

where $N_{face,total}$ is the total number of phonons injected by the isothermal wall. Phonons are introduced into the simulation randomly though the time step until the energy E_{face} has been reached within a tolerance of $\hbar\omega_{max,TA}$. The phonon will be located arbitrarily along the face of the wall with the wavevector generated randomly, ensuring the unit vector normal to the wall and is facing into the material.

Adiabatic boundaries with specular reflection are also used. These are container boundaries at which purely elastic collisions occur. Figure 4.4 shows the effect of an adiabatic wall on position, wavevector and velocity.

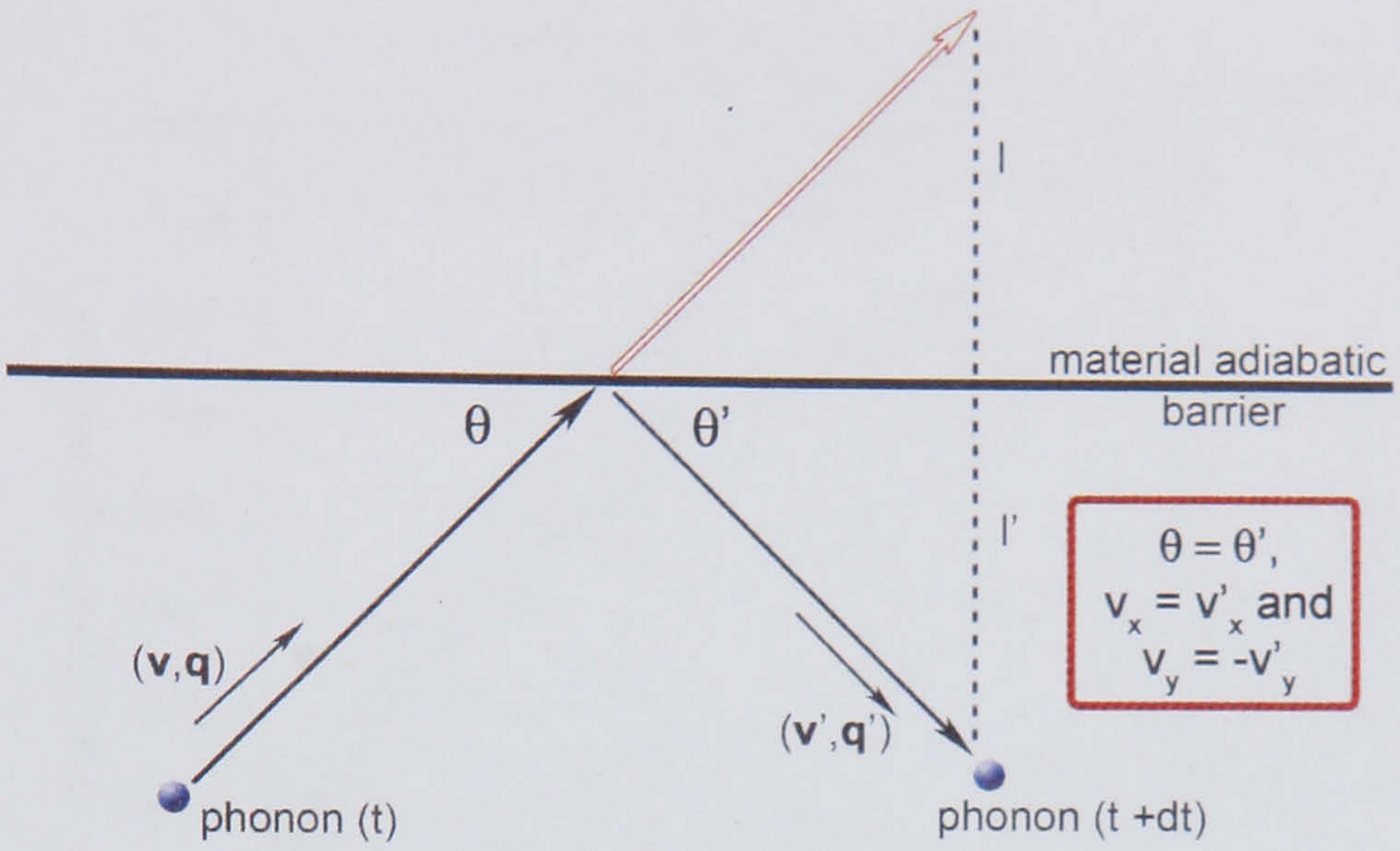

Figure 4.4: Illustration of elastic reflection.

4.4.6 Analysis of non-momentum MC method

The discretisation of the dispersion curve in energy space has the consequence that each energy step encompasses a variable step in wavevector space as shown in figure 4.5 (indicated by the green and red lines). As the average energy of the energy step increases, the wavevector space accounted for by this step increases. Figure 4.5 also compares the dispersion curve to the equilibrium population at 300K in an isolated system for TA phonons. This shows that the population encompassed at high frequencies is much larger. Around room temperature, where the largest proportion of the phonons will be at these high energies, representation of these phonons by the average energy will be inaccurate without very small discretisation steps. Mazumder accounts for this by using very small discretisation steps ($\Delta\omega = \omega_{max,LA}/1000$). The use of such a large number of discretised steps also requires a high number of sample particles in order to represent the phonon distribution adequately and adds to the computational complexity of the simulation.

The scattering algorithm implementation does not attempt to conserve momentum, the rationale being that the lack of conservation will account for the Umklapp scattering. This means that the U-process effect is not included explicitly. The results in section 3.6.3 show that the influence of the U-processes is temperature dependent. Mazumder's

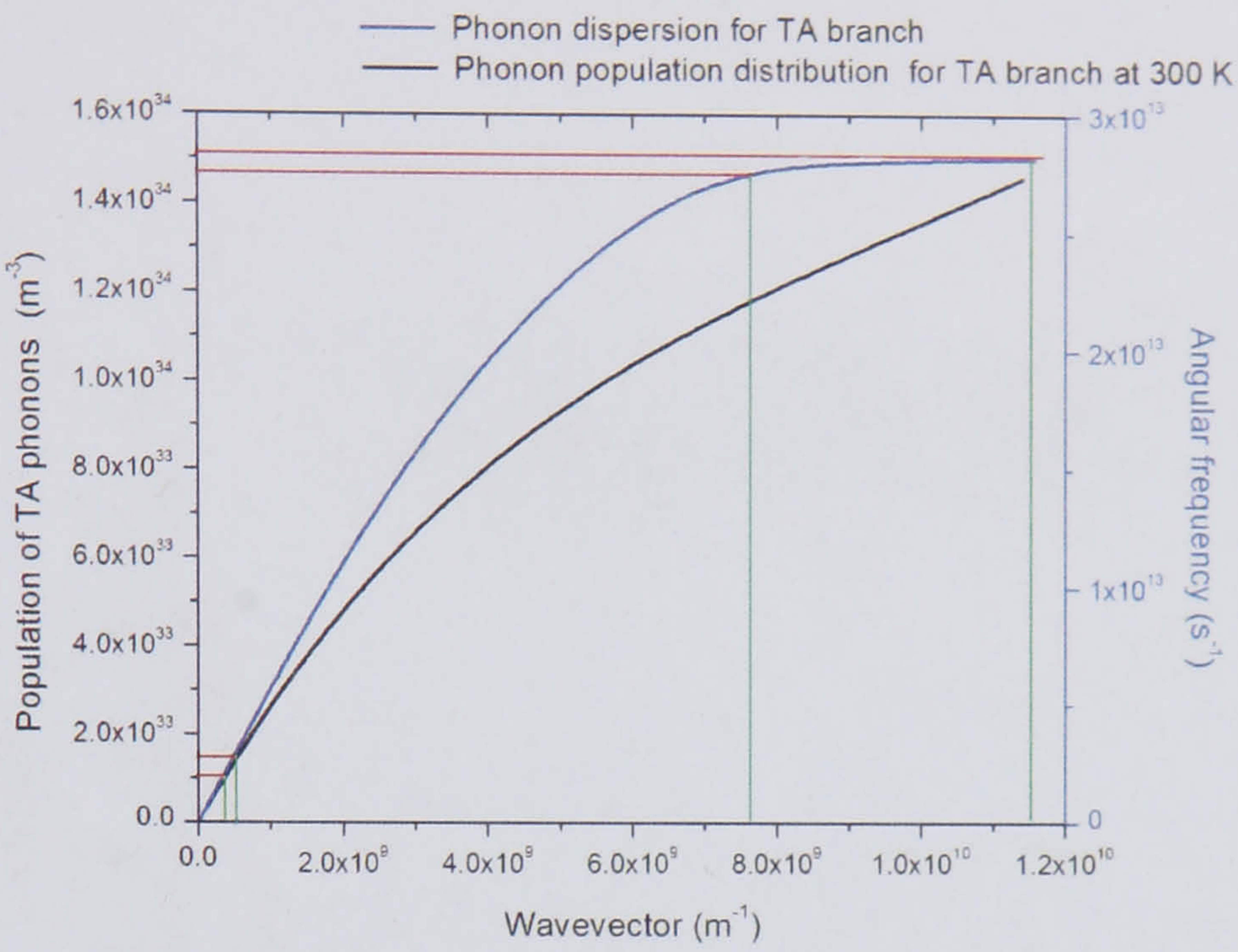

Figure 4.5: Comparison of the TA dispersion relationship to the population density of TA phonons in silicon.

method does not accommodate this effect.

When Mazumder's method is applied to an equilibrium system (in this case, an isothermal block at 300K with 3μm by 1μm by 1μm dimensions and $N_{prescribed}$ at a 100000) the scattering method does not maintain equilibrium. The steady state[4] phonon distribution is shown in figure 4.6. The resulting distribution shows a shift of the phonon population to lower energies. This deviation occurs because the ratio of high frequency to low frequency phonon relaxation times greatly exceeds the corresponding ratio for population numbers. The effect is more apparent in the LA distribution due to the lower relaxation time and lower population numbers. This would lead to an overall increase of the average phonon speed in the material.

Mazumder uses the example of an adiabatic 2D simulation of a GaAs (gallium arsenide) square with isothermal boundaries on two opposing walls set at 500K and 300K respectively and dimensions outside of the ballistic limit. Mazumder's published result [36] agrees with Fourier's Law. Figure 4.7 shows the results of the simulation described above, when applied to a 3D silicon adiabatic tube with the same isothermal

---

[4] Steady state occurs when the overall population within the simulation is approximately constant.

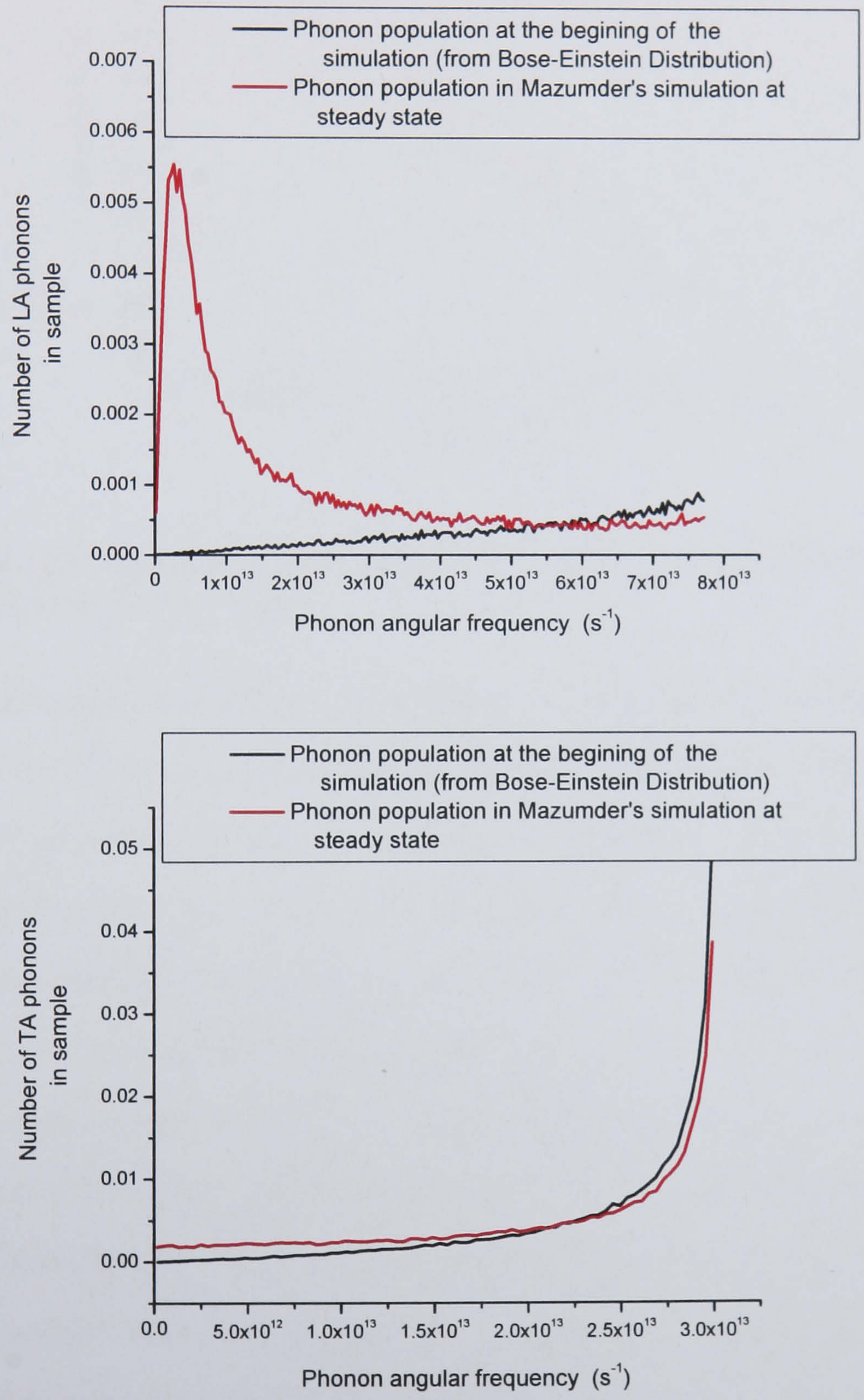

Figure 4.6: The change in phonon distribution from initial conditions to steady state.

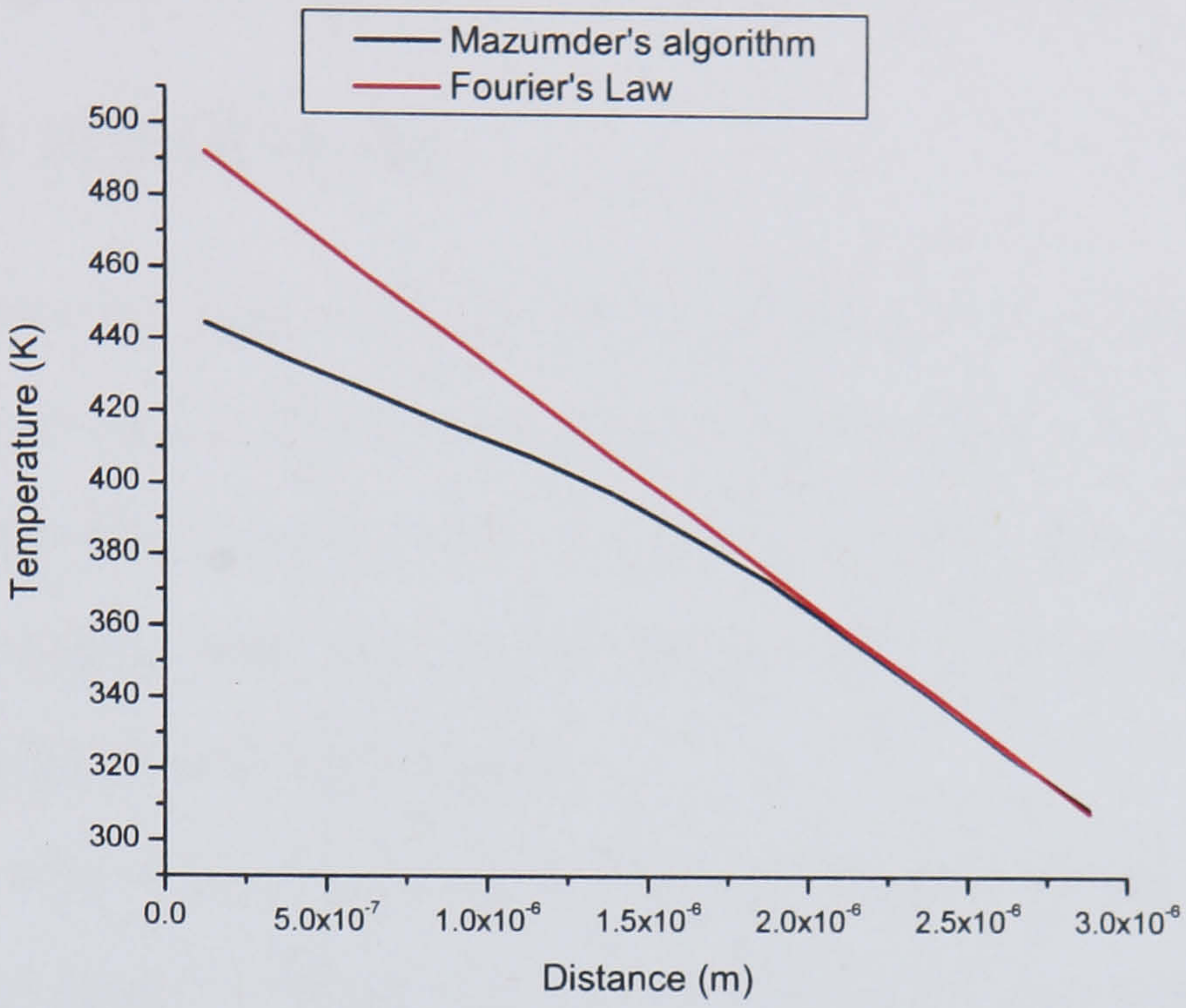

Figure 4.7: Thermal profile of a $3\mu m$ block of pure silicon with isothermal injection at 500K and 300K on opposing sides.

boundaries and 3μm by 1μm by 1μm dimensions. The isothermal boundaries are placed orthogonal to the 3μm plane. The result shows that there is a definite deviation from Fourier's Law[5], predicting lower than expected temperatures closer to the 500K wall. This can be attributed to the change in phonon distribution discussed above. At higher temperatures the phonons will have a higher relaxation time, causing the shift into lower energy phonons to occur quicker. This then increases the phonon speed and allows the phonons to traverse across the material faster. This causes a lower thermal resistance and thus an inability for the material cells to maintain the higher temperature.

Though Mazumder [36] shows that his methodology does predict thermal conductivity with reasonable accuracy, there is some discrepancy between the results shown in his work compared to the results obtained from the ostensibly equivalent simulation described here. This is discussed further in section 4.7.

---

[5] The linear prediction is based on a constant thermal conductivity value.

4.5 Re-engineering the non-momentum MC conservation simulation

One of the main shortcomings of Mazumder's method is its inability to maintain equilibrium, thus even in non-equilibrium simulations the resulting phonon distribution is likely to be unrepresentative of the real phonon distribution responsible for transport. An attempt was made in this work to alter Mazumder's core scattering algorithm to further bias the simulation to equilibrium.

Some changes were made to the core algorithm in order for the alterations to the scattering ladder to be put in place. In the re-engineered simulation, the discretisation of the dispersion curves is done in wavevector space using the scalar value to make profiling of a simulation population easier.

4.5.1 Scattering method alteration

As stated in section 2.3, the effect of anharmonic scattering, in an isolated system, is to morph a non-equilibrium distribution to an equilibrium distribution. To implement a more effective bias to the re-population algorithm, an alteration was made to the way in which this occurs. At the beginning of the re-population process, a histogram of the phonon population in the cell is created. This is then used to create a re-population probability tree in which the probability of a phonon being added to the cell is determined by the difference between equilibrium phonon population and the population of sample phonons (see figure 4.8). The population histogram is updated as phonons are added to the cell.

To add tighter control of the energy conservation to the simulation, the tolerance factor was removed and an "energy reservoir" was added to each spatial bin. This reservoir acts as a static energy store. When the phonon addition stage occurs, phonons are added to the cell until all the scattering energy is accounted for. If the phonon

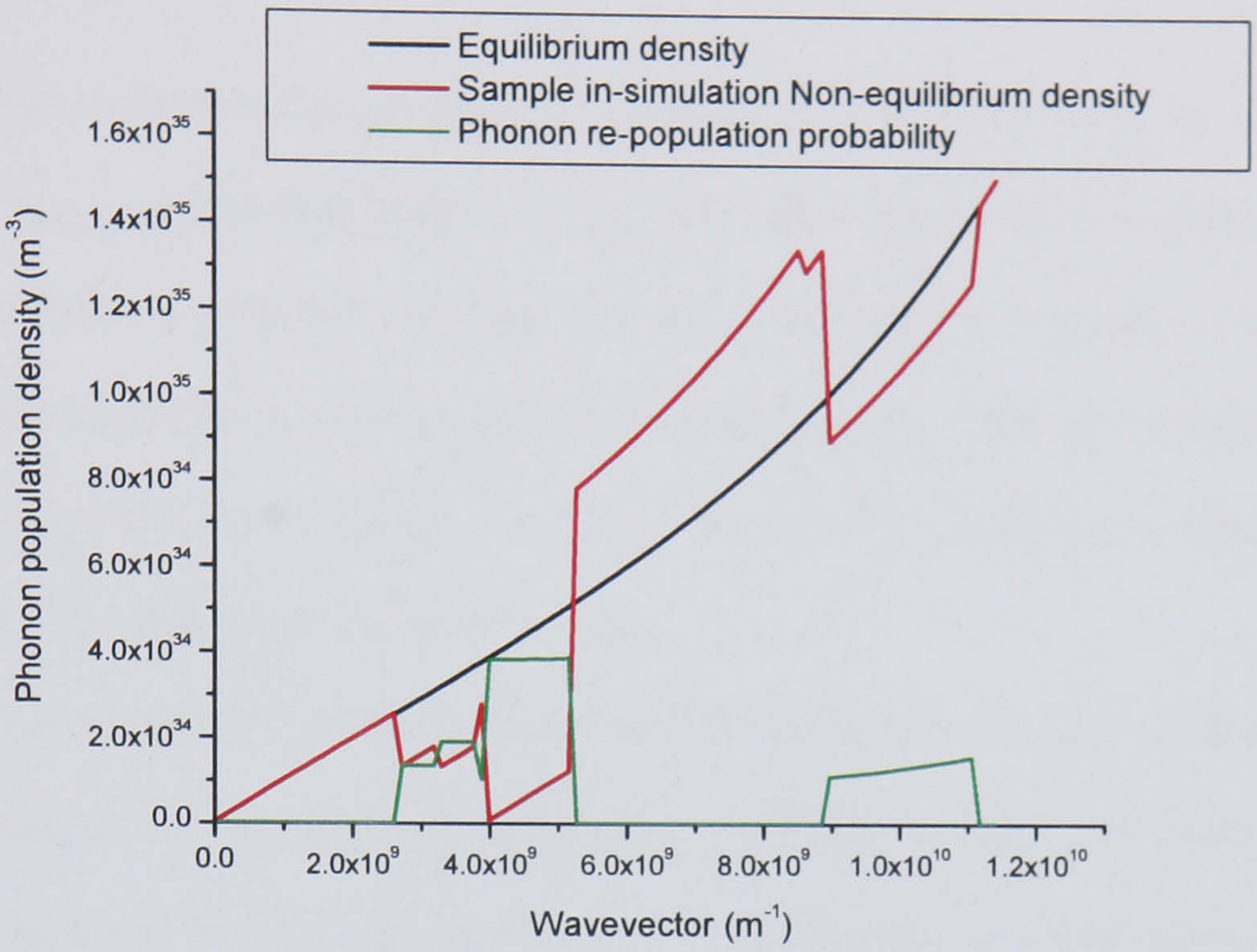

Figure 4.8: Illustration of method used to calculate the re-population probabilities in the re-engineered Mazumder simulation. The sample population used in this figure is for illustration purposes.

addition process results in an overshoot of the scattering energy, the last phonon added is removed and the scattering energy left prior to the addition of that phonon is stored in the energy reservoir. During the next scattering stage after the next time step, the energy in the reservoir is added to the scattering energy. The reservoir still contributes to the calculated temperature of the cell.

The justification is that a significant proportion of the phonon population will be high energy TA phonons. These are low velocity phonons and therefore act as a sort of static energy store. The energy reservoir only represents a small percentage of the energy in the cell, and can be considered as a contribution to these high energy phonons of which there is a significant population at temperatures above 100K. This approximation is harder to justify at low temperatures (below 30K) as the TA phonon distribution at high energies is small: however at low temperatures the amount of energy that would be stored in the reservoir is much lower.

4.5.2 Results

In the equilibrium test simulation (300K isothermal cube with 3μm by 1μm by 1μm dimensions and $N_{prescribed}$ at 500,000), the biasing algorithm yeilds a significant improvement over Mazumder's original method. Figure 4.9 shows the steady state distribution for this improved algorithm. The graph shows the steady state distribution matches the theoretical equilibrium distribution for TA phonons, although there are still significant discrepancies on the LA phonon distribution.

The deviation in the LA phonon distribution is due to the use of the material cells. For the same reasons as the original algorithm the lower energy phonons are more likely to be created. At these lower energies there are insufficient phonons in each cell to fill the histogram with a representative population, and thus the biasing to the re-population method is ineffective without a larger $N_{prescribed}$ and a low discretisation of wavevector space. The higher deviation in the LA branch is due to the lower number of these types of phonons.

For the reformulated algorithm to work more effectively than the original, each material cell must have sufficient stochastic samples in order to generate the histogram. Thus the smaller the cells being used in simulation the larger the sample population. This will lead to increased computational expense.

There is also an increased "bumpiness" in the population curves for the LA phonons, which is a result of quantisation error associated with the use of the histogram. In figure 4.9 the difference between the analytical population calculation and the simulation population for LA phonons in a single cell can be seen. There is a point at which the discrete distribution matches the analytical curve; the fluctuations around this point are due to the residual phonon addition probability. This effect is reduced with decreased scaling, hence the effect cannot be seen in the TA population curve. The smoothing out is caused by averaging over the whole material.

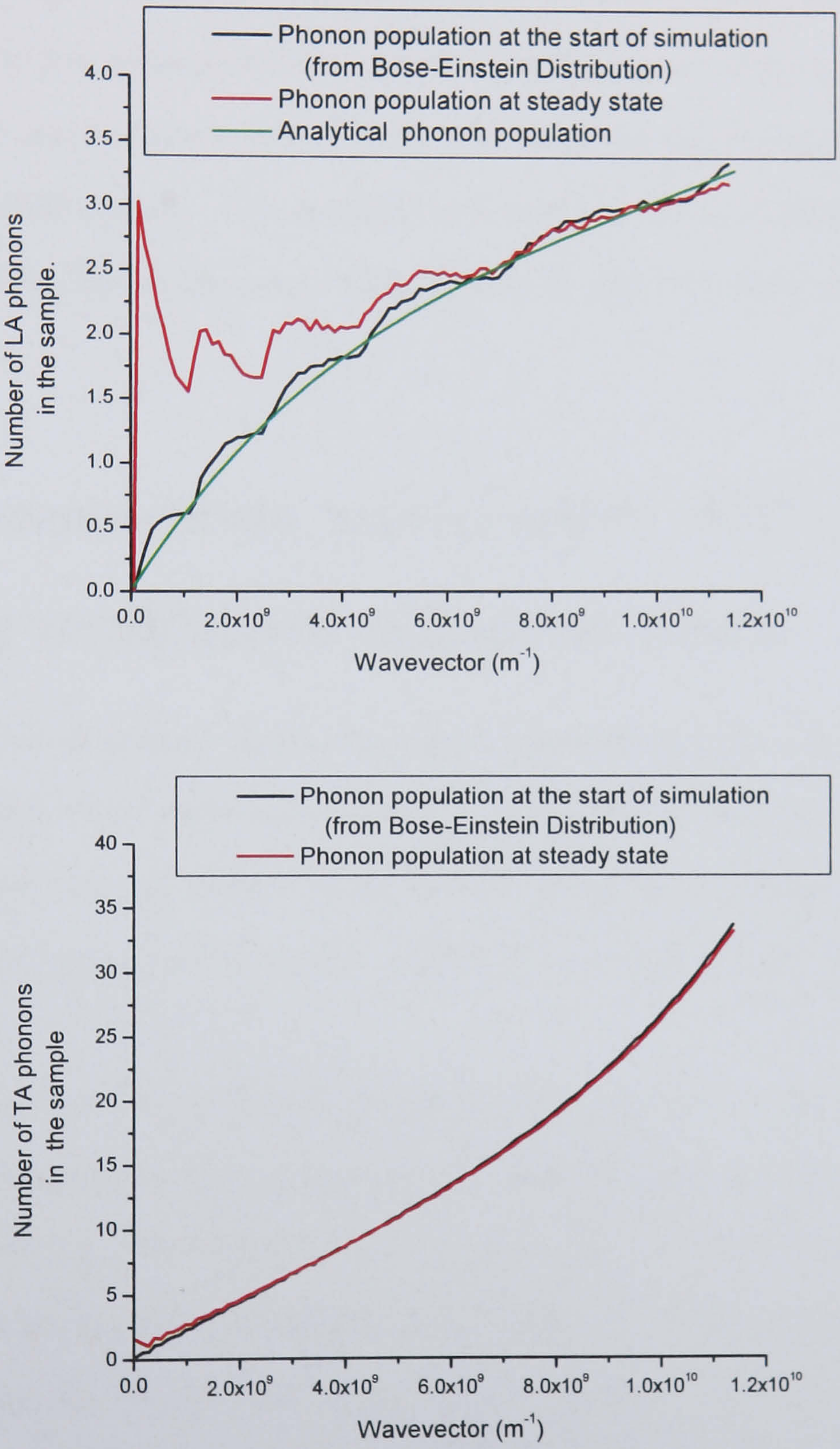

Figure 4.9: The change in phonon distribution from initial conditions to steady state in the re-engineered Mazumder Monte Carlo method.

4.5.3 Simulation usage

Using this method results in a trade-off between computational time and accuracy of the re-population method. With the use of some trial and error, the parameters for operation which would allow a sensible computational time and achieve an improvement over Mazumder's method were determined. The optimum discretisation of wavevector space was set at 100 spaces. The material cell size was set at $1.5625 \times 10^{20}\text{m}^3$ while $N_{precribed}$ was set at 500000 phonons. This equates to approximately 2500 phonons per material cell.

4.6 Non-momentum conservation MC simulation using recalculated relaxation times

As the calculations in chapter 3 show a greater agreement with experimental thermal conductivity values than Holland's relaxation time approximations, an attempt was made to use these phonon relaxation times with Mazumder's methodology. The relaxation times are calculated using the equations in section 3.5 and determined from equation 3.36.

As with Holland's relaxation times, which are calculated for an equilibrium distribution, this method uses the equilibrium phonon relaxation times applied to the calculated temperature of the cell. This approximation works if the simulation is initialised at an equilibrium state and a small time step is used. Small time steps result in minor deviations from equilibrium. With a sufficiently large stochastic sample distribution[6], small changes will not result in significant changes in the relaxation time calculation.

It is shown in the literature [23,29,49] that, in order to maintain equilibrium, a balance of creation and annihilation must occur. To maintain equilibrium a re-population scheme is developed using relaxation times. Using the approximation that relaxation

---

[6] Around 1000 sample particles per material cell are used to obtain these results.

times will be based on cell temperature we can apply this to the re-population probabilities. Therefore the probability of a phonon being created as a result of a scattering event is:

$$P_{create}(q, LA/TA) = \frac{n_{eq}(q, LA/TA)D(q)}{\tau(q, LA/TA)} \qquad (4.12)$$

In the re-population method of the scattering algorithm (section 4.4.4) we can rectify the mismatch described in section 4.4.6 by using the re-population probabilities described above.

Lacroix [77] applies a similar method to improve on the work that Mazumder does. This is done by using Holland's relaxation time and formula described above for re-population. Lacroix makes some additional changes to the way in which scattering occurs. This is discussed further in section 4.8.

4.6.1 Results

The re-population method undertaken here better illustrates the variation around equilibrium. When simulating equilibrium the overall distribution does not change significantly. Figure 4.10 shows that the phonon distribution changes in an isothermal block (300K with 3μm by 1μm by 1μm dimensions and $N_{prescribed}$ at a 100000). These graphs show that there is a change in the phonon distribution over time, but these changes do not significantly deviate from the initial distribution. This is a much better result than for either of the previous methods.

The test case of a 3D silicon adiabatic tube with isothermal boundaries of 500K and 300K respectively produces the steady state result shown in figure 4.11, which matches the linear approximation of Fourier's Law with far greater accuracy than the other MC simulations described above. The deviation from Fourier's Law is expected due to the change in thermal conductivity with temperature. At higher temperatures the thermal conductivity is lower, hence the higher thermal gradient.

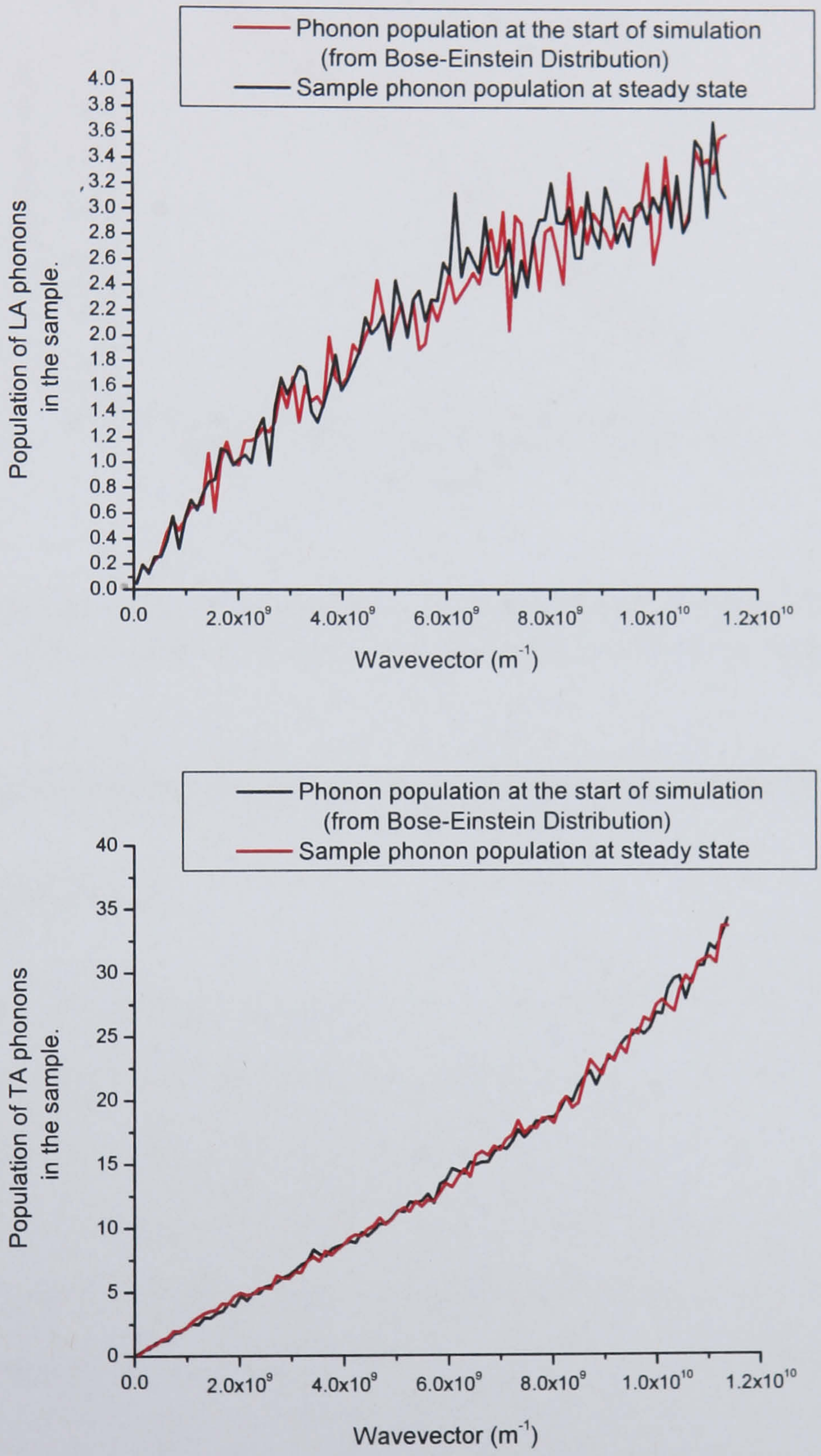

Figure 4.10: The change in phonon distribution from initial conditions to steady state in the MC method using the recalculated relaxation times.

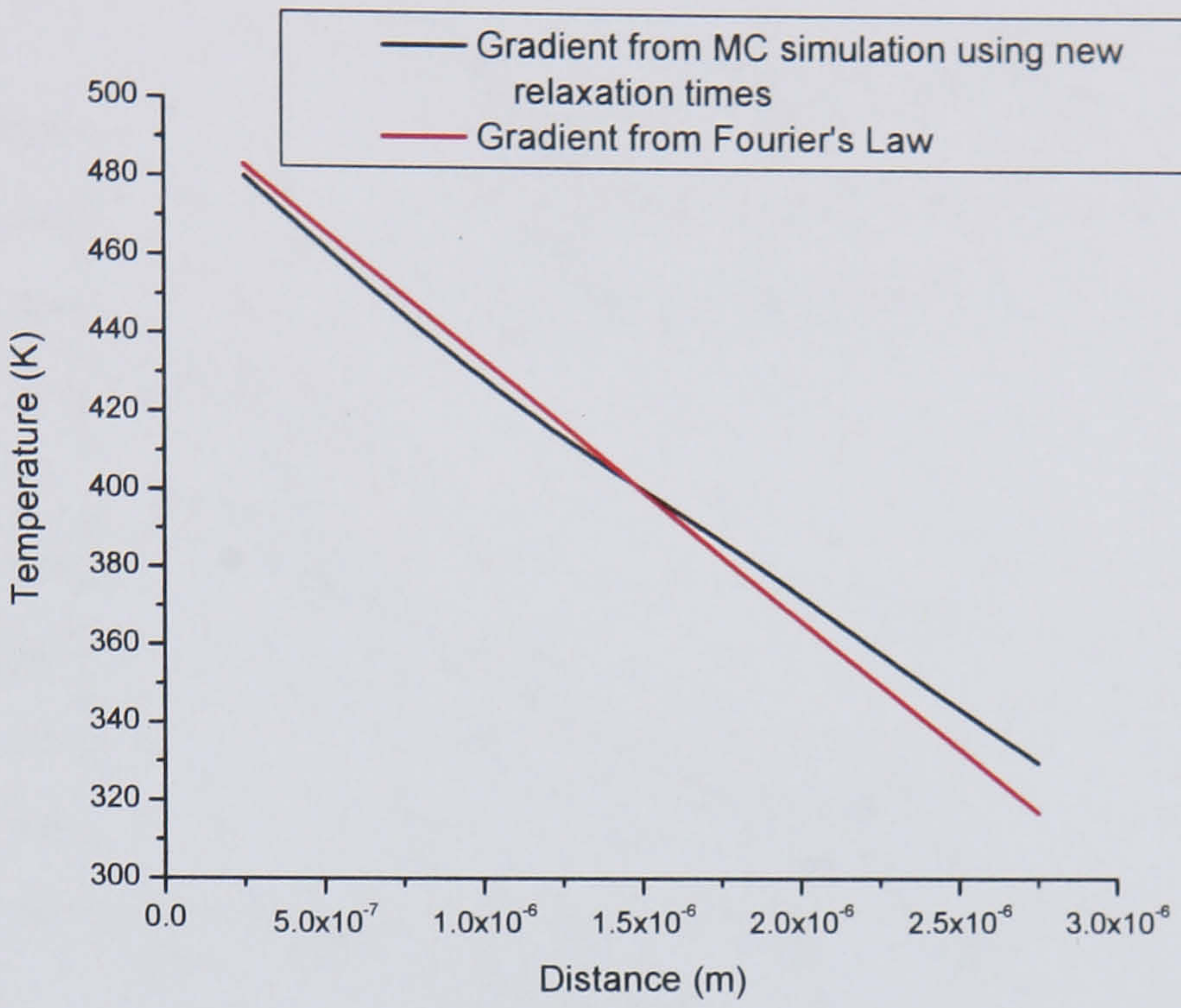

Figure 4.11: Thermal profile of a 3μm block of pure silicon with isothermal injection of 500K and 300K on opposing sides from MC simulation using re-calculated relaxation times.

4.7 Comparison of non-momentum conservation MC simulations.

Figure 4.12 shows the thermal conductivity values yielded by the various simulation algorithms; these values are evaluated once the simulation reaches steady state. The geometry used for these results is a 3μm by 1μm by 1μm block with fully reflective adiabatic boundaries except for the boundaries orthogonal to the 3μm length, which are isothermal boundaries. The injection conditions for the isothermal boundaries are set at a 20 degree difference. The thermal conductivity (κ) is calculated from

$$\kappa = \frac{L}{A\Delta T}\frac{\mathrm{d}Q}{\mathrm{d}t}, \tag{4.13}$$

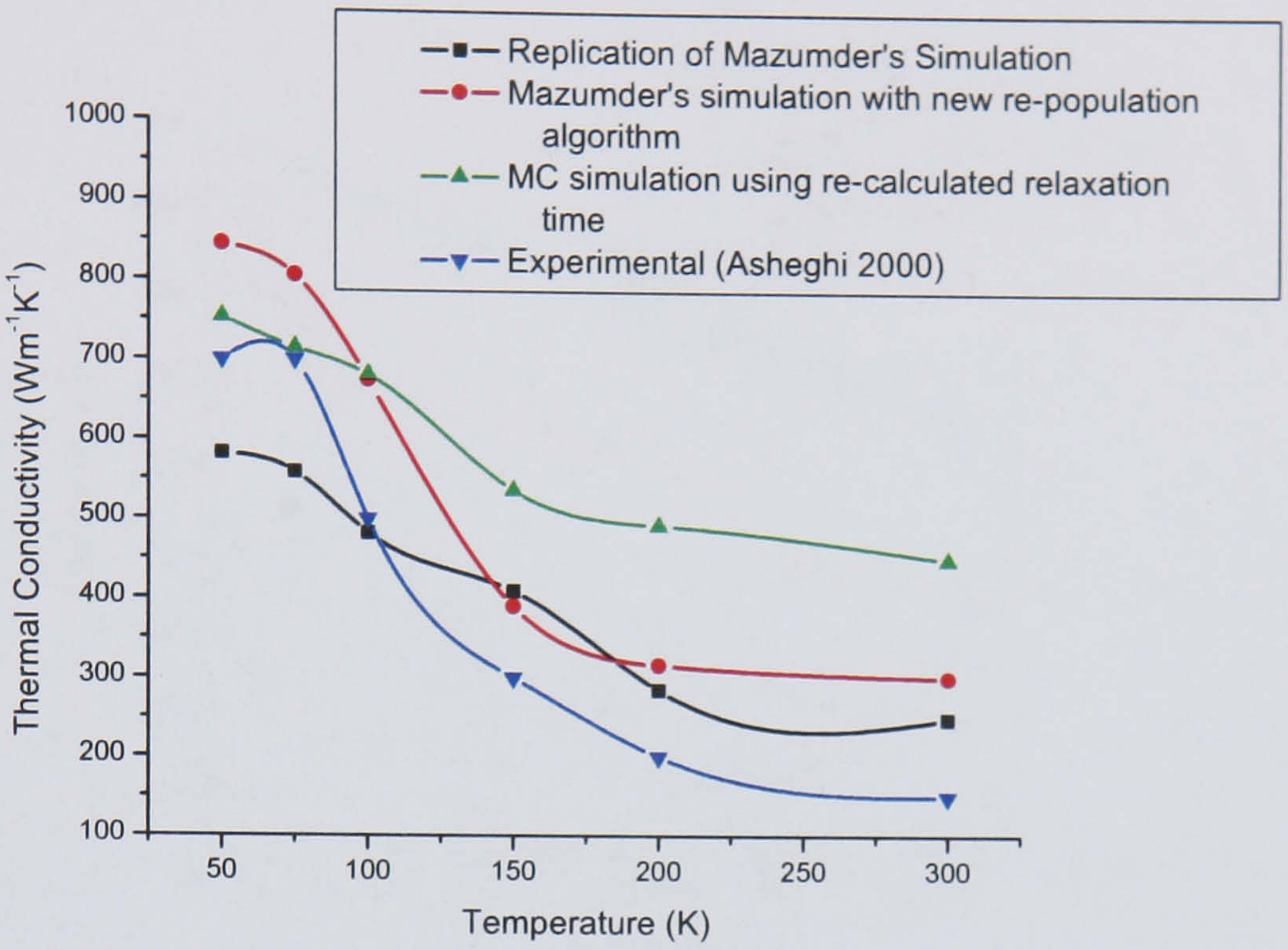

Figure 4.12: Thermal conductivity results for the different MC simulation algorithms.

where A is the cross sectional area, L is the length of sample, ΔT is the temperature difference between the isothermal walls, $\mathrm{d}Q/\mathrm{d}t$ is the heat flux calculated by

$$\frac{\mathrm{d}Q}{\mathrm{d}t} = \frac{(E_{b1,in} - E_{b1,out} - (E_{b2,in} - E_{b2,out}))}{t}, \tag{4.14}$$

where $E_{i,j}$ is the energy crossing the boundary bi which is when $b1, b2$ are the parallel isothermal boundaries, *in* represents the energy introduced to the simulation from the isothermal boundary, and *out* is the energy removed by this boundary.[7]

The thermal conductivity observed from the replication of Mazumder's simulation shows relatively good correlation with experimental values from Ashegi [8]. The replication of Mazumder's simulation has not yielded the same results shown in his paper [36], where the results reported are much closer to experiment. The reason for this discrepancy is unclear as the replication followed exactly the methodology described in this

---

[7] The 3μm length scale is outside of the ballistic limit for the relaxation time derived in chapter 3. Therefore to obtain a steady state result for thermal conductivity the simulation has to run for a larger number of time steps than the solutions based on Holland's relaxation times.

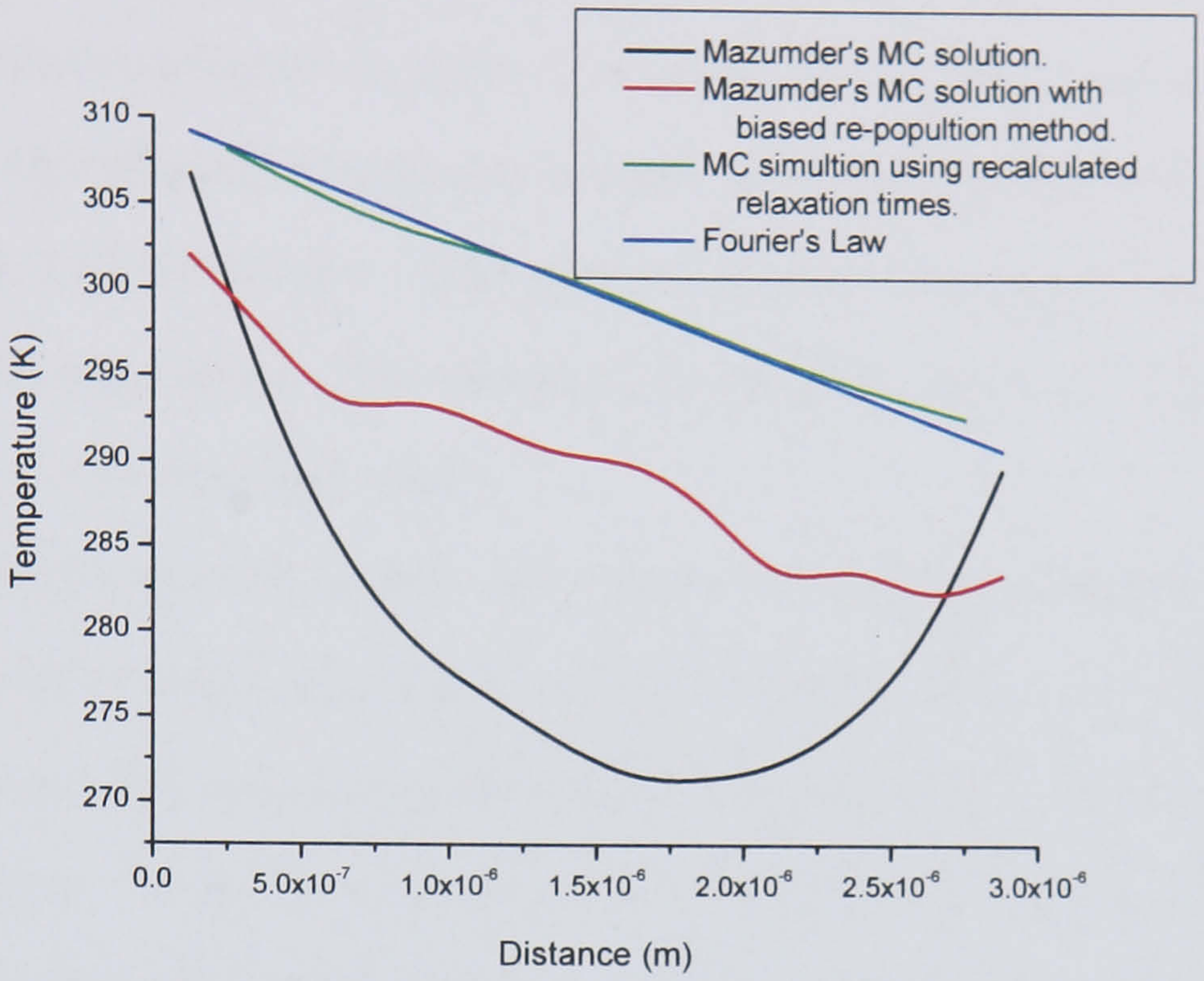

Figure 4.13: Thermal profile for the non-momentum conservation MC simulations for the case used for thermal conductivity calculation of 300K.

paper.

Figure 4.12 shows that all simulations produce results for thermal conductivity in the same order of magnitude and they show the correct trend, displaying a reduction in value at high temperatures. The thermal conductivity is overestimated in all the algorithms used. The changes to Mazumder's method cause further deviation from the experimental values. However the temperature profile produced for small temperature differences by the different simulation algorithms shows a different picture. Figure 4.13 shows the temperature profile for the simulation algorithms run with isothermal boundaries at either end of 310K and 290K respectively. The changes result in the temperature profile closer to expected steady state results. From figure 4.13 we can see that Mazumder's method does not predict a suitable temperature profile at all, despite the more reasonable result seen in figure 4.7. Obviously the accurate simulation of small temperature gradients is much more challenging but nonetheless essential for extracting thermal conductivity values.

In the simulations, when applying a small temperature difference across the material, the phonon population present should be that of the average temperature in the material. In figure 4.14, the phonon population present at steady state, which generates the results in figure 4.13 are shown. The phonon distribution produced by Mazumder's method are highly inaccurate. The altered methods produce a result with a much closer correspondence to the expected result.

Both Mazumder's method and the MC simulation with recalculated relaxation times have the advantage of being much more computationally simple, and also allows the use of a significantly smaller sample population as the re-population methods do not require population tracking. These simulations produce results within about a third of the time of the biased re-population MC algorithm. When simulating temperatures of about 300K, the biased re-population MC simulation time can take up to six times longer to reach steady state. The computational expense involved in using the biased re-population MC simulation far outweighs the improvement which is seen in the thermal conductivity and temperature profile results.

4.8 Discussion

The methods described in this chapter do not explicitly simulate the U-processes but instead cater for these processes by removing phonons from the simulation, when scattered, and replacing them with new phonons whose wavevectors are generated stochastically according to the appropriate probability distribution. This method, used originally by Mazumder [36], is designed to introduce a lack of momentum conservation which gives rise to a thermal resistance, but there is no guarantee that this somewhat arbitrary momentum non-conservation gives the same thermal resistance as results in practice from precisely defined mapping of phonon wavevectors into the first Brillouin zone. The results from the the thermal conductivity calculations seen in section 4.7 indicate that they do not. In addition to this, results in section 3.6.3 show that there is a temperature

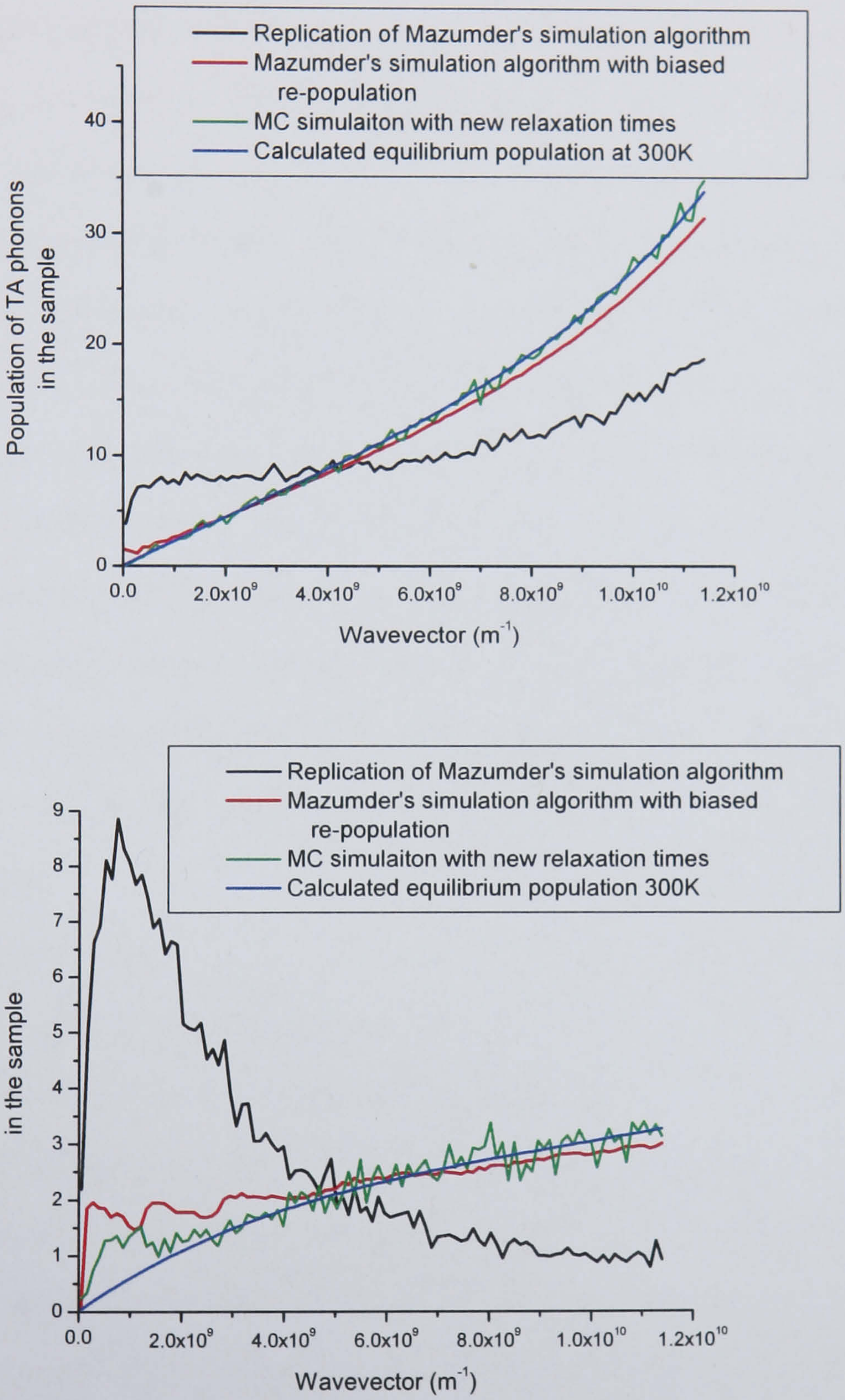

Figure 4.14: The steady state phonon population in a conducting material based on results from the various non-momentum conservation MC solutions.

dependence of the percentage of Umklapp processes. The randomising of the phonon population will not cater for this change.

In section 3.6.2 it is shown that U-process are the predominant scattering process at high frequencies(see section 3.6.2) while normal processes dominating low frequencies. Lacroix [77] tries to cater for this by altering the scattering method in Mazumder's algorithm. He regards the 3-phonon processes in terms of absorption and emission of a second phonon by another "test" phonon scattering. He assumes this second phonon will have the same wavevector as the phonon which scatters. This is because the rates of absorption and emission are approximately equal. In the mechanics of the simulation he then makes the approximation that whenever a phonon scatters with a N-process, the phonon remain unaffected. For U-processes he maintains the approximation that Mazumder introduces; however using the same principle as for the N-processes, the phonon experiences the random change in the direction of the wavevector. This does not seem like a particularly good approximation, and clearly does not give exact wavevector conservation for N-processes; nonetheless Lacroix appears to obtain reasonable results from his simulation.

Chen [78] also attempts to rectify the shortcomings in Mazumder's method by including a test to ensure a pseudo-momentum conservation. Chen has developed an algorithm which, during the re-population phase of the simulation, creates several sets of phonons for re-population, then using a genetic algorithm, tests for momentum and energy conservation. The set that is determined a best by the criteria of the algorithm is added to the simulation. Without replication of this algorithm, there is no way to test its validity, though Chen states the effect of the new algorithm in bulk silicon simulations, over Mazumder's original algorithm, is negligible. Chen's solution is still based on the relaxation times derived in Holland's [11] work which do not fully represent the 3-phonon process.

The use of equilibrium relaxation times in the models detailed in this chapter are a good approximation for bulk materials, however application of these models to small material geometries, where the phonon distribution can deviate significantly from equilibrium, will not cater for the changes in scattering rates. In section 2.5 we can see the effect that phonon distribution will have on phonon scattering. Implementation of a localised phonon scattering calculation could provide a more accurate simulation at these lower dimensions.

4.9 Summary

The replication of Mazumder's method brought to light some shortcomings in his algorithm. The result of testing his algorithm in an isolated equilibrium simulation shows a distinct shift of the phonon distribution into lower frequencies. Several attempts were made to fix this discrepancy using different re-population algorithms. These shortcomings were overcome leading to correct phonon distributions and temperature profiles, yet all methods overestimate thermal conductivity at higher temperatures. There is a reduction shown in thermal conductivity values derived from the simulation as temperatures increase, however the reduction does not increase in correspondence with the experimental values. This implies that with a better representation of scattering, more accurate values of thermal conductivity can be derived.

Chapter 5

Momentum conservation Monte Carlo simulation

In chapter 4 the analysis and development of several Monte Carlo methods for phonon transport was discussed. Though these methods have had some degree of success, the fundamental flaw in their construction is that these methods do not conserve momentum and thus do not model thermal resistance accurately. This chapter will describe an attempt at an implicit momentum conservation MC solution.

5.1 New algorithm

The new method uses a similar methodology to the methods described in chapter 4; the material parameters are the same and the same spline parameters are used. This method also uses spatial, temporal and wavevector discretisation. There are some significant differences due to the nature of the new scattering method. The main difference is that we no longer discard wavevector information after a scattering event: additionally, when scattering of a phonon is determined to be a merge process, a partner phonon must be selected from the simulation.

The initialisation of the simulation algorithm, the drift movement of the phonons and the boundary conditions applied are implemented in the same way as for the simulations seen in chapter 4. The simulation changes are outlined in figure 5.1 and will be discussed in detail in the following sections.

5.1.1 Scattering changes

Due to the scaling done in the initialisation of the simulation population to create a representative phonon population (see section 4.4.2) and the assumption of a phonon being a particle, simulating phonon collisions by monitoring phonon positions would be a complex problem. In an MD or ideal gas simulation, particle size could be used to provide an interaction volume. As phonons are only quasi-particles that do not actually exist in real space, it is difficult to define a size. To use momentum and energy conservation in a MC scheme which would cater for the reduced population, a "sphere of influence" must be determined. A phonon selected for scattering can then be allowed to scatter with all other phonons present within this volume. This volume would, in this case, be independent of phonon size. As the material is already divided into cells to monitor local temperature, these material cells were used to define this "influence" volume. The scatting method then used is shown in figure 5.2.

For each cell the relaxation time calculation is calculated as in chapter 3 at each time step. A histogram of the phonon population is recorded for each cell and used to determine the phonon distribution in that cell. This is calculated by using the phonon population per wavevector step ($N(q,p)$) and the relation

$$\langle n(q,p) \rangle = \frac{N(q,p)}{D(k)}. \tag{5.1}$$

When a phonon is allowed to scatter (the same scheme as used in section 4.4.4 for testing whether a phonon scatters), a table of probabilities associated with scattering events is built using the phonon distribution in the cell. Phonons can then scatter in

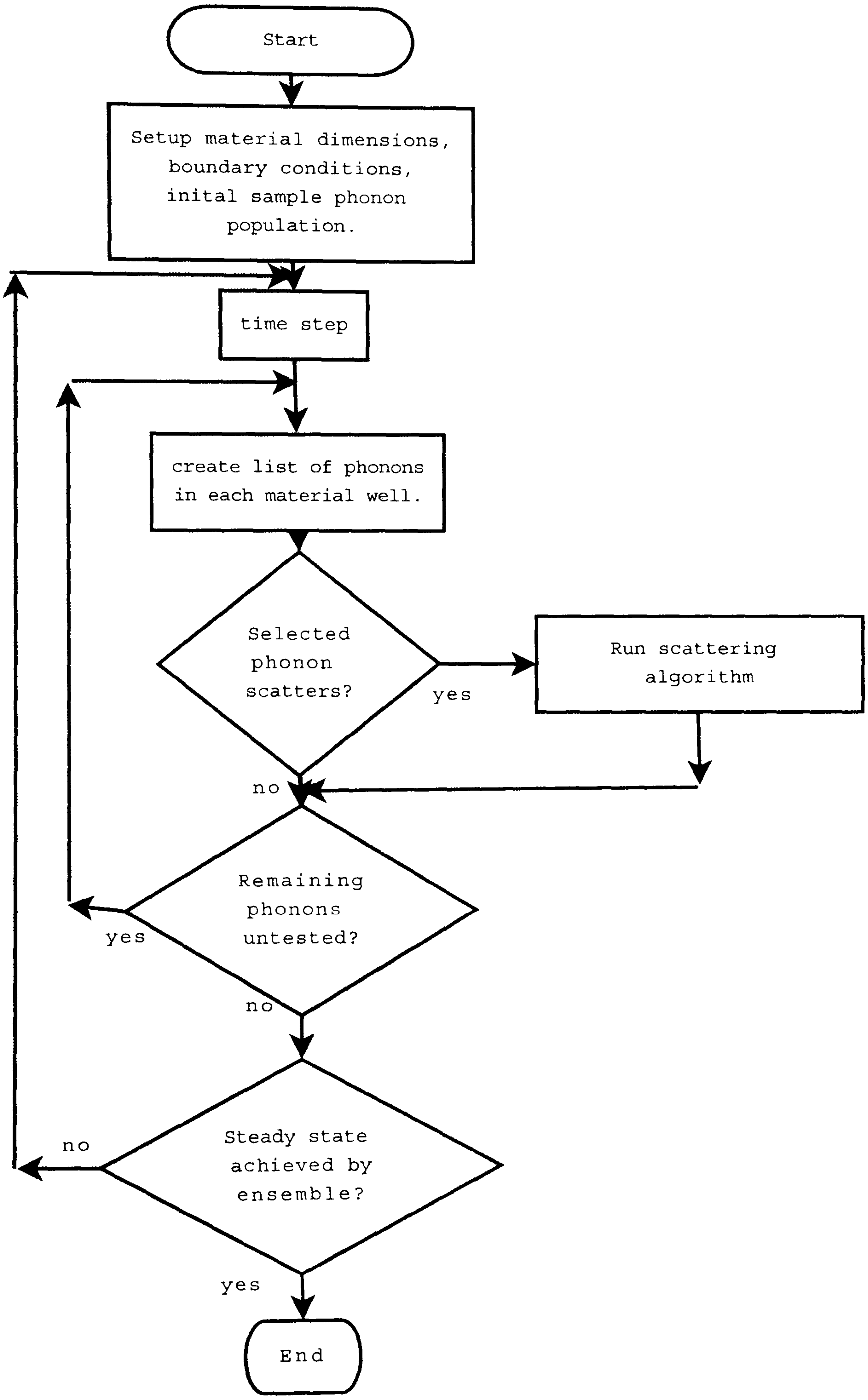

Figure 5.1: Flow chart for the momentum conservation MC simulation.

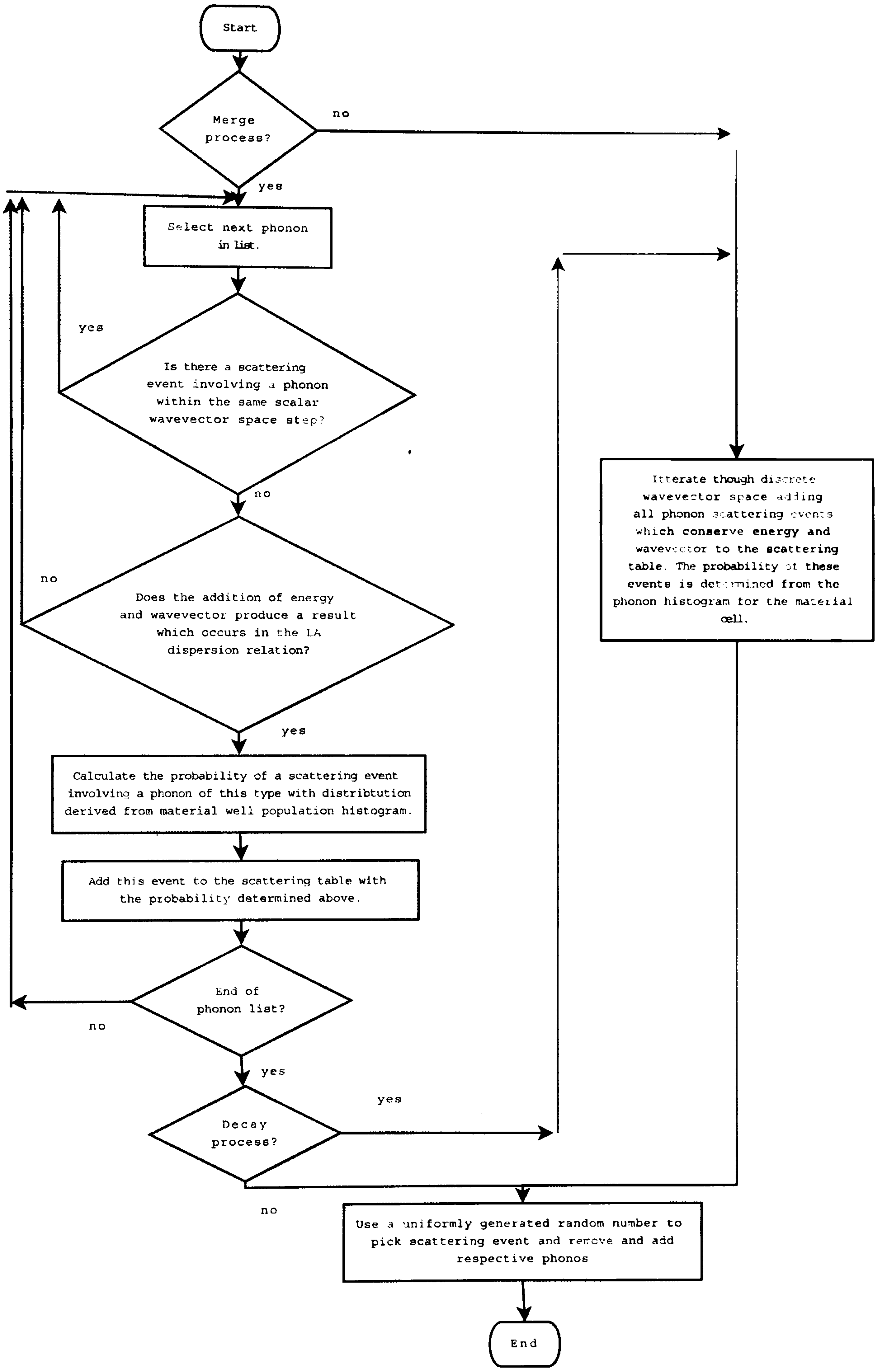

Figure 5.2: Flow chart for the scattering mechanism used in the momentum conservation MC method.

two ways according to the three phonon processes: either a merge process, whereby the phonon which will scatter merges with another phonon in the cell to create a higher energy phonon, or a spontaneous decay process, whereby the phonon will split into two lower energy phonons (see section 2.4.1), the second only being applicable to LA phonons due to energy conservation.

To ensure all scattering events are included, the relaxation times of the phonons are evaluated as

$$\tau_T^{-1} = P_{TA+TA\rightarrow LA} \tag{5.2}$$

$$\tau_{L,merge}^{-1} = P_{LA+TA\rightarrow LA} \tag{5.3}$$

$$\tau_{L,decay}^{-1} = P_{LA\rightarrow LA+TA} + P_{LA\rightarrow TA+TA}. \tag{5.4}$$

The $LA+TA \rightarrow LA$ processes is not included in the TA relaxation time to avoid double counting of the scattering events. In the scattering algorithm the partner phonon is selected freely from all phonons in the cell and so $LA + TA \rightarrow LA$ processes will be fully catered for in the LA merge scattering. This problem would also be encountered if the relaxation times used were from Holland's [11] work.

When determining whether a LA phonon will scatter, the calculation to evaluate scattering (equation 4.8) is done twice: firstly to test for a decay process using the relaxation time $\tau_{L,decay}$, and then to test for a merge with the relaxation time $\tau_{L,merge}$. The opportunities for decay and merge processes are evaluated separately in order to ensure that decay processes are not overestimated. Figure 5.3 shows the difference between the merge and decay scattering rates: at low frequencies the merge process occurs at a much higher rate than decay. In a situation where the distribution of phonons deviates significantly from equilibrium, a combined relaxation time would overestimate the decay rates for low energy phonons and vice versa for high energy phonons. Even though the merge and decay processes are evaluated separately, a LA phonon can be

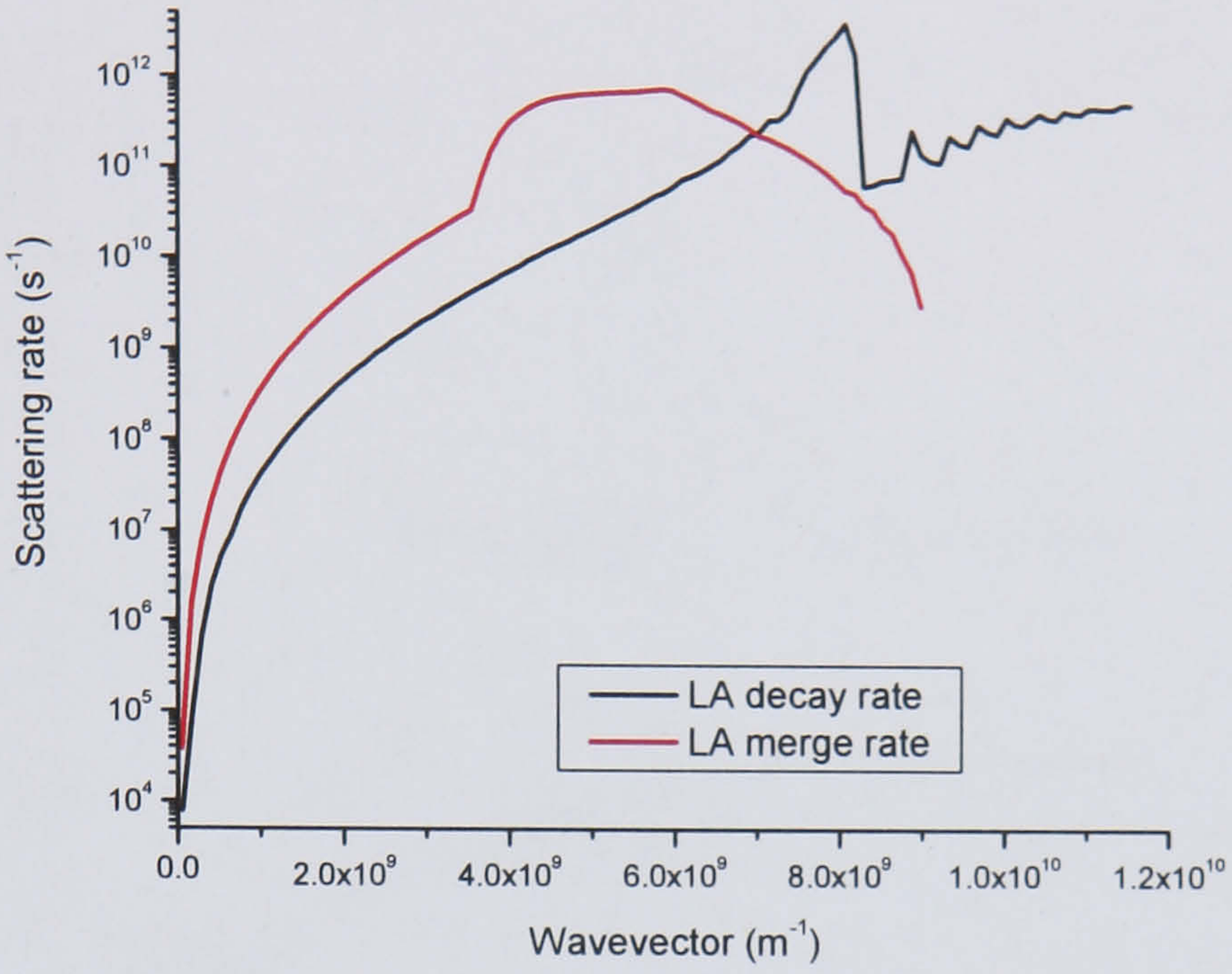

Figure 5.3: Comparison of LA phonon merge and decay scattering rate at 300K calculated at equilibrium.

allowed to scatter both ways in a time step. When this situation occurs the phonon scattering table is populated with both merge and decay processes.

When building the probability table, the merge process requires selecting a partner for each phonon to scatter with. The partner is selected by ensuring energy and momentum conservation within an energy conservation tolerance. The tolerance is required due to the discretisation in wavevector space and the scaling of the phonon population. Without any tolerance, exact conservation of energy and momentum would not occur in the simulation, and so phonon scattering would be grossly underestimated. The energy conservation tolerance is determined by the energy space step size of the resultant discrete wavevector as shown in figure 5.4. If the sum of the energies of the two chosen phonons is within the tolerance, then the scattering event will be added to the scattering table. One partner is selected per wavevector step for each acoustic dispersion curve and the probability associated with the scattering event is added to a scattering table. The probability is calculated with the formulation given in chapter 3 using the phonon distribution of the cell.

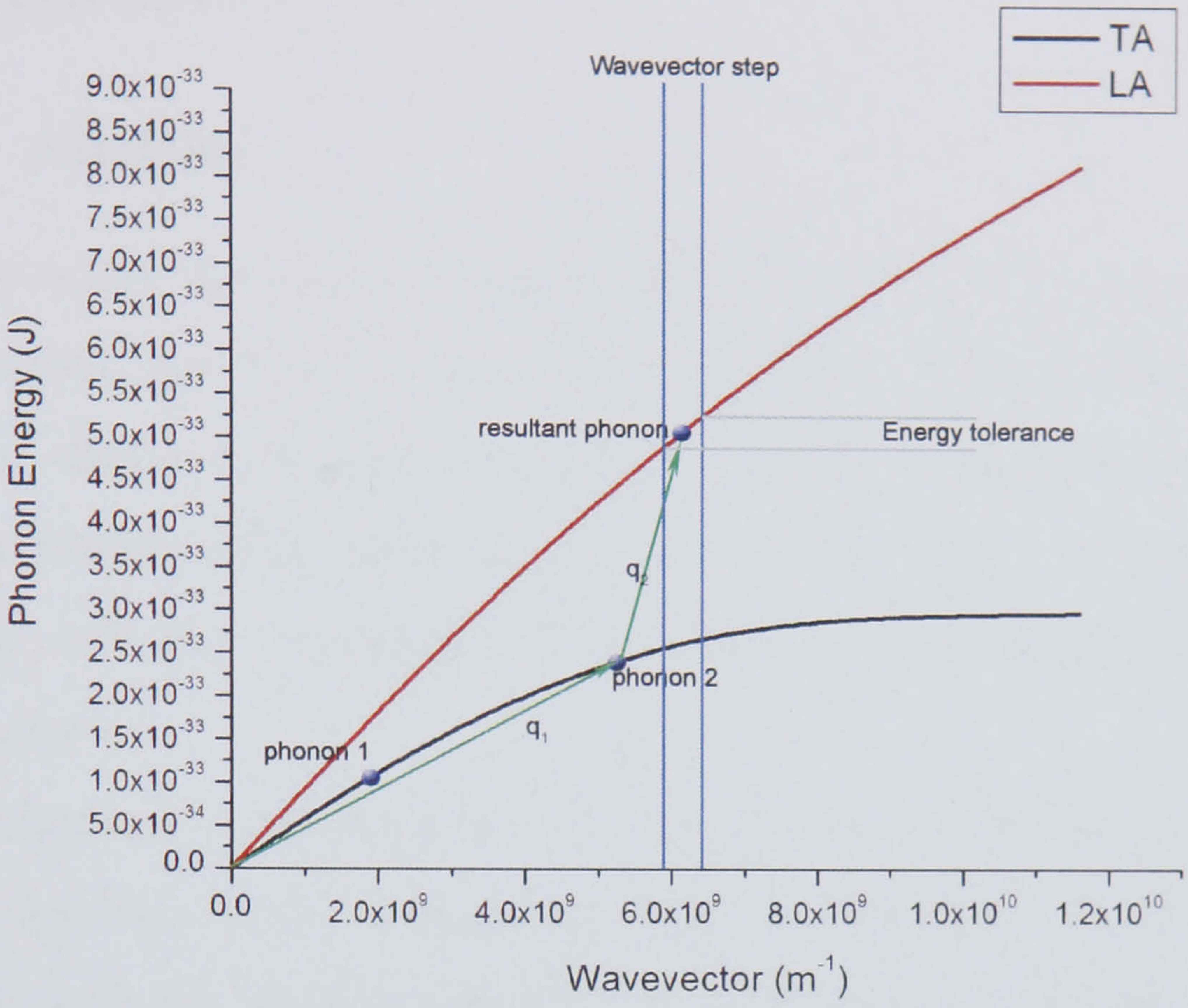

Figure 5.4: Illustration of the energy tolerance in merge scattering events.

As the decay process is spontaneous and does not require the use of nearby phonons, scattering events of this sort are added to the scattering table without explicit testing of energy and momentum conservation. The rates of these events are determined by the phonon distribution in the cell which the phonon occupies.

The scattering event that occurs is chosen stochastically. In the case of a decay event of an LA phonon, the phonon that scatters is replaced by two phonons. These phonons have the same position vector as the original phonon. A merge event removes the two phonons selected for scattering and replaces them with a phonon which has the combined energy and wavevector of the original phonons. The position vector assigned to the new phonon is that of the of the phonon for which the scattering table has been created. The resultant position in the cell should not contribute significantly to the simulation results as the redistribution of energy caused by a number of these processes should even out.

5.2 Results

5.2.1 Analysis

The 3-phonon momentum conservation algorithm does bring to light some limitations of the scaling method used in this Monte Carlo solution. When searching for a partner phonon to interact with, the momentum, and energy conservation procedures limit interaction between all the phonons in a material cell. Unlike with the decay processes, there are no degrees of freedom for the geometrical vector calculations required for a merge process.

The already low population of low energy phonons is reduced by the scaling factor in the stochastic particle representation. When simulating an equilibrium system, the scattering table will not have sufficient scattering events to represent low energy phonon interactions without using a large sample of stochastic particles in a material cell. Figures 5.6 and 5.5 show the difference in the scattering probabilities with the number of stochastic samples in a material cell.

Typically in previous Monte Carlo simulations a sample population of approximately 1000 particles per cell was used (section 4.4), whilst in the biased re-population method used in section 4.5 a population of about 2500 per cell was used. In figure 5.5 the scattering table probabilities for the simulation with 2500 particles per cell show a distinct underestimation for both N and U processes, with the deviation from the analytical results being larger for the N-processes. Figure 5.6 shows that, with 100000 phonons in the sample, there is an accurate representation of the possible scattering events. The energy and momentum tolerance was increased in an attempt to reduce this effect, but this resulted in a much noisier simulation which did not converge.

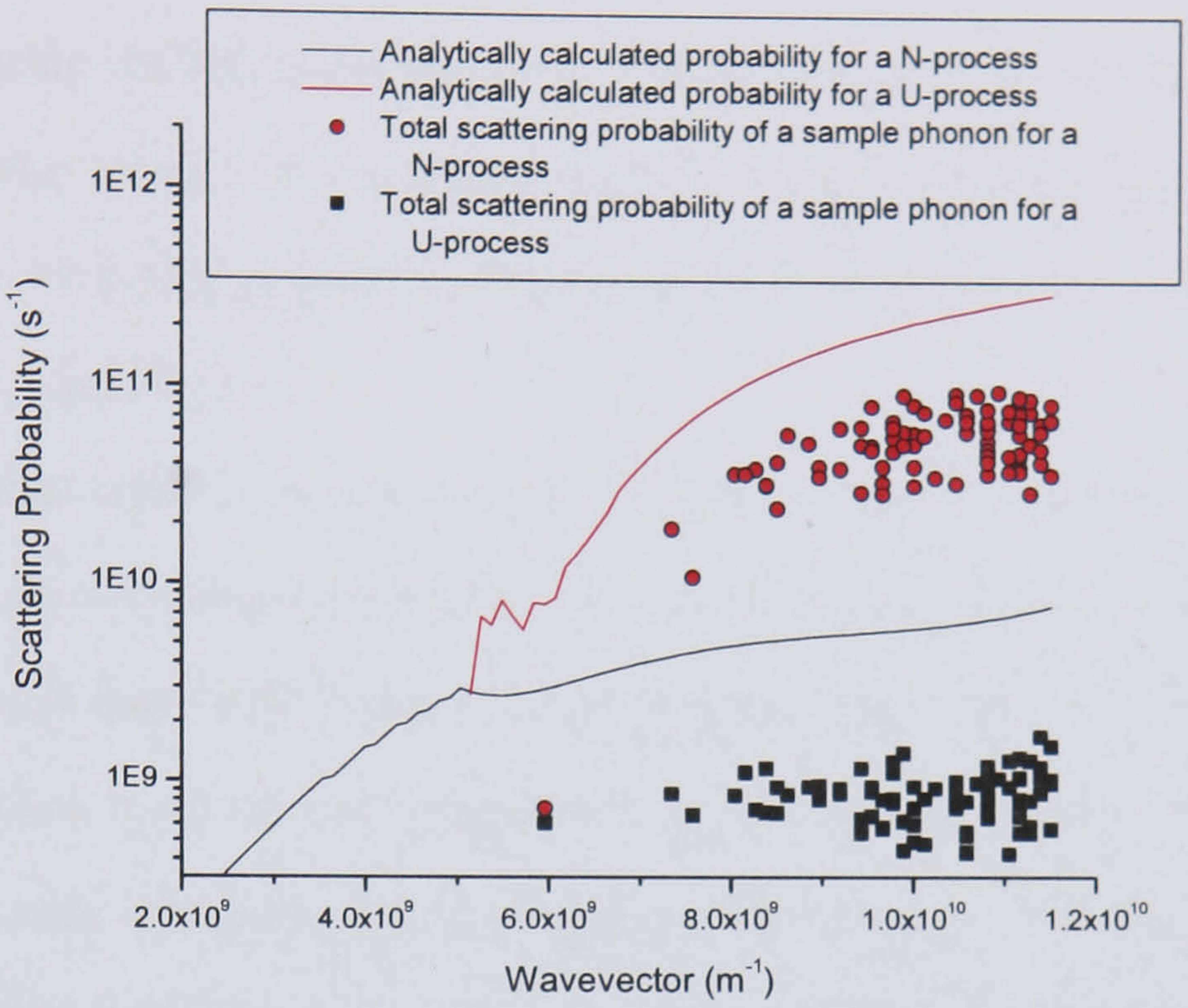

Figure 5.5: Scattering probabilities of the $TA + TA \rightarrow LA$ transitions at 300K for a sample of TA phonons with 2500 stochastic particles in a cell.

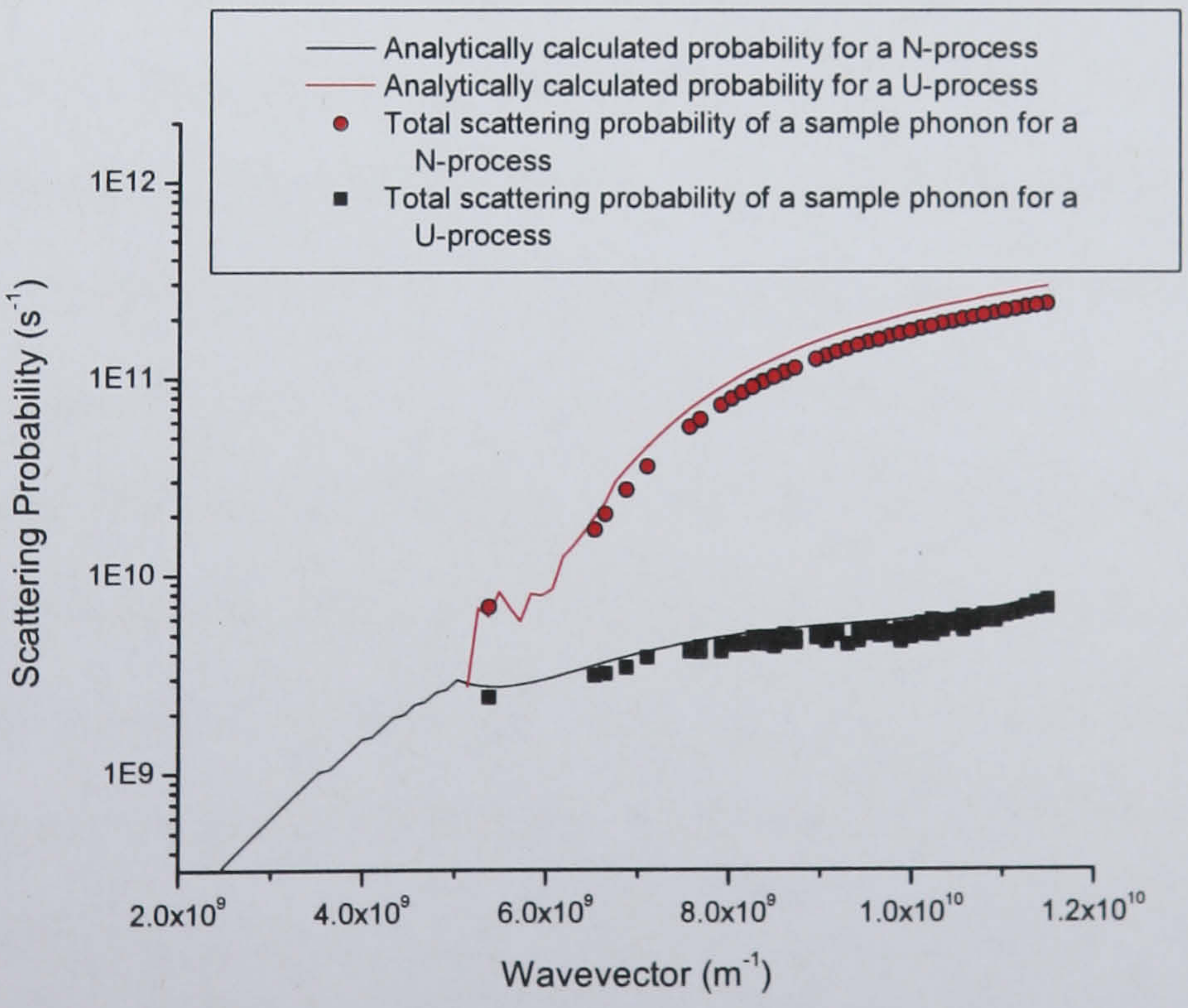

Figure 5.6: Scattering probabilities of the $TA + TA \rightarrow LA$ transitions at 300K for a sample of TA phonons with 100000 stochastic particles in a cell.

5.2.2 Testing

Using approximately 33,000 particle per material cell, we can provide sufficient samples for a reasonably accurate scattering ladder. The discrepancy described above still remains; however with this population the ratio of U-processes to N-process is approximately correct at equilibrium.

The method was applied to a rectangular block of 3μm by 1μm by 1μm with reflective boundaries. Simulations carried out for a uniform temperature of 300K showed a significant deviation from equilibrium in the steady state. Table 5.1 shows the relative contributions of each type of scattering event in the simulation, both at the beginning of the simulation run, when the phonon distribution is known to be in equilibrium, and after convergance to a steady state. These values are dominated by scattering of high energy phonons since they have much shorter lifetimes

It is shown that, at the start of the simulation there is an expected dominance of the $TA + TA \leftrightarrow LA$ U-process transitions (see section 3.6.2). As the simulation progresses the population shifts increasingly to higher energies, thereby increasing the overall scattering rate and increasing the influence of the $TA + TA \leftrightarrow LA$ U-process. The larger the number of particles used in the simulation, the longer it takes for this effect to occur. In theory, with sufficient particles in the cell, this effect would not occur.

A simulation was also carried out for a uniform temperature of 30K. At this low temperature the relatively small effect that anharmonic interactions have on the material is apparent, with the result that the simulation does not deviate significantly from equilibrium within a typical simulation time frame. Figure 5.7 shows the change in phonon distribution over a simulation time of 3×10^{-8} seconds, which has been long enough for the simulation to reach steady state in other MC algorithms reported above.

The results shown in figure 5.6 imply that the discrepancy mentioned above can be avoided using a larger ensemble ($\geq$100,000 particles per cell). However, this simulation could not be performed since the simulation time would be far too long.

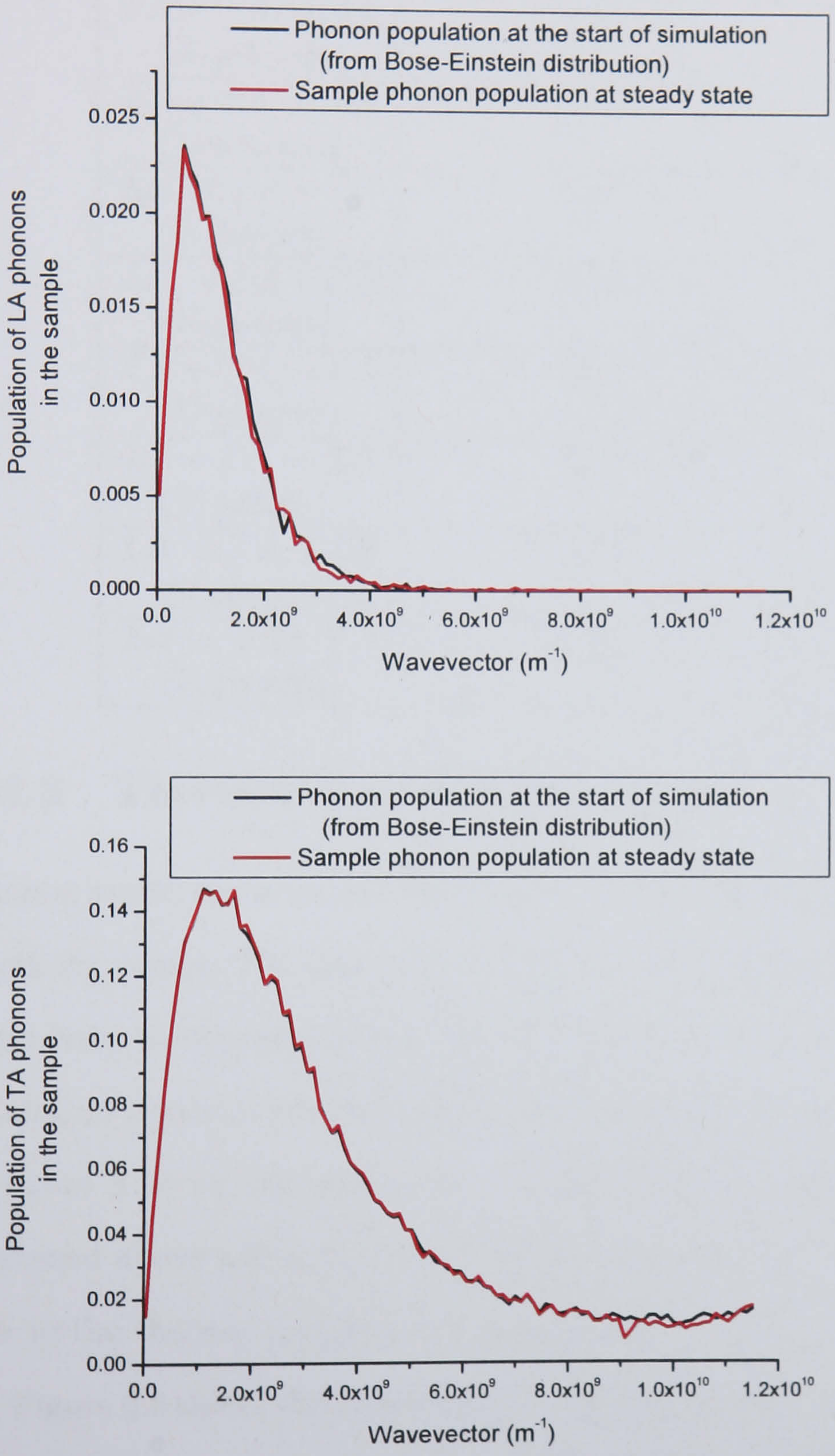

Figure 5.7: Phonon distributions extracted from the momentum conservation MC simulation for a silicon sample at a uniform temperature of 30K.

Table 5.1: Change in phonon-phonon rates in momentum conservation simulation

Scattering Event	Percentage Occurrence at equilibrium(%)	Percentage Occurrence at steady state(%)
$TA + TA \rightarrow LA$ (N-process)	1.15	0.3
$LA + TA \rightarrow LA$ (N-process)	1.31	0.11
$LA \rightarrow TA + TA$ (N-process)	1.78	0.8
$LA \rightarrow LA + TA$ (N-process)	1.79	0.01
$TA + TA \rightarrow LA$ (U-process)	44.2	19.6
$LA + TA \rightarrow LA$ (U-process)	2.21	0.001
$LA \rightarrow TA + TA$ (U-process)	45.8	49.1
$LA \rightarrow LA + TA$ (U-process)	1.67	0.004

5.2.3 Thermal conduction analysis

Phonon transport in an adiabatic tube was simulated in order to generate thermal conductivity values. The dimensions of the tube were 3μm by 1μm by 1μm with isothermal boundaries at opposite ends of the tube which differ in temperature by 20K. Using 33000 stochastic particles per material well and with the results for the mean free path shown in figure 3.13 we can state that, even though the change of the phonon distribution discussed above will occur, it will be partly negated by the phonon population being in flux in the thermal conductivity calculations.

Figure 5.8 shows the results for the thermal conductivity derived from the momentum conservation simulation. Thermal conductivity is extracted from the simulations using the same calculation used in section 4.7 at steady state. The continued scattering of phonons into high energy states at high temperatures ($<$ 100K) results in the phonon distribution having a large increase in low mobility phonons. This result in an ever increasing phonon population within the material. The simulation cannot the reach

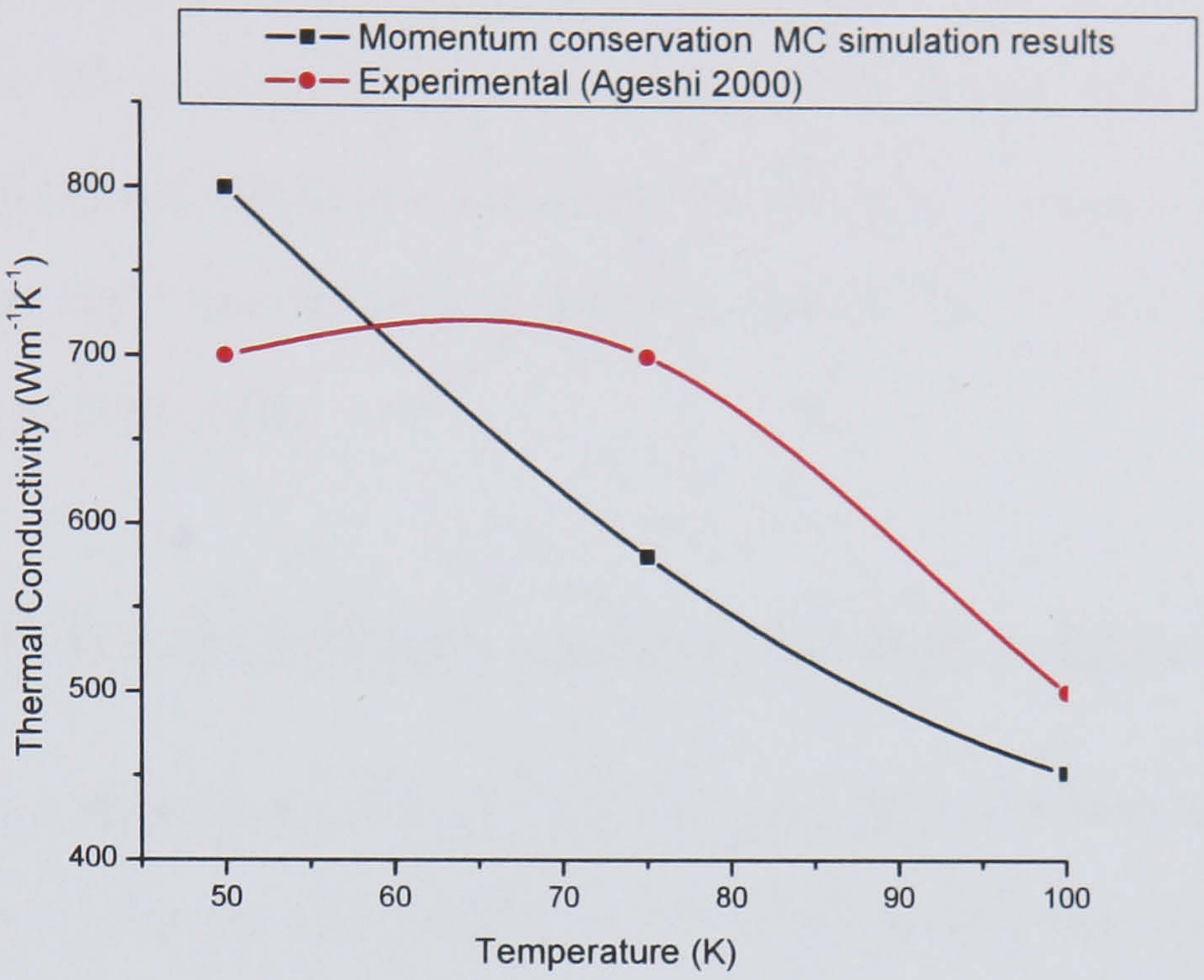

Figure 5.8: Comparison of thermal conductivity results from the momentum conservation MC simulation to Ashegi's [8] experimental results.

steady state under these conditions, however at low temperatures this effect is not significant enough to prevent steady state and, therefore, thermal conductivity values can be obtained.

Figure 5.8 shows the low temperature thermal conductivity results derived from this MC solution. The results shown are within acceptable error margins. The graph shows the simulation does slightly underestimate thermal conduction as expected from the tests above and the approximations made in the simulation of the Umklapp prosesses, but the overall trend of the change is correct. This method could be used for simulation at very low temperatures.

5.3 Review of solution

There is a massive computational expense involved in running this simulation. The results discussed above have taken months to achieve. In order to extract points for a thermal gradient which will accurately represent the material, six or more cross sectional points are required and, as shown above, at least 100,000 samples per well. This means a minimum of 6×10^5 particles must be simulated, which will result in an estimated 6 months of computational time on a standard PC CPU for a simple bulk simulation to reach steady state. Any advantage to using this method will be lost due to the greatly increased computational time.

5.4 Other momentum conservation algorithms

A number of other algorithms were developed and rejected during this work. A first attempt at this work was to use Holland's [11] relaxation times as used by [36, 77, 78]. The problem with this solution is that Holland's relaxation times do not differentiate between scattering processes and therefore cannot be used to build a scattering ladder. The approximations that Holland used will also cause misrepresentation of the scattering rates (discussed in section 3.2.1). The TA and LA relaxation times both incorporate the $LA + TA \rightarrow LA$ transitions, and so will result in double counting these transitions. In addition, Holland's relaxation times do not differentiate between decay and merge processes and this could result in an overestimation of either process (see section 5.1.1). This would also only offer an equilibrium solution; if the phonon distributions were to deviate significantly from the equilibrium Bose-Einstein form, the relaxation times would not reflect these changes.

Another algorithm used a MD-like approach. The spontaneous decay was handled explicitly in the same way as described in section 5.1.1; however the merge process was handled using a "sphere of influence" approach. The size of the cell was determined by the velocity of the phonon and the scale associated with the simulation. All phonons with in this cell were tested for energy and momentum conservation and a scattering tree built from those that satisfied the requirements. If no phonon was available to scatter then the phonon continued unscattered. This method was very computationally expensive since an interaction volume must be defined for each phonon at each time step.

In order to make this solution computationally feasible, an approximation of an average cell size was used. This approximation resulted in an overestimation of scattering rates at all temperatures. Steady state results were wildly inaccurate.

The first incarnation of the solution described in section 5.1.1 used a more explicit method of building the scattering table. Instead of using the phonon selection method to associate a probability for a transition to a paired phonon, the table was built by associating the probability of the scattering event being with that phonon such that

$$P = \frac{S}{n(q_2, j)} \times P(\mathbf{q}_1(i) + \mathbf{q}_2(j) \rightarrow \mathbf{q}_3(LA)) \tag{5.5}$$

where i and $j = TA/LA$. The more explicit dependence on the discrete population resulted in further exacerbation of the effect discussed in section 5.2.1.

5.5 Summary

It has been shown that the use of a momentum conservation simulation is incredibly computationally expensive. The computational requirement for any higher temperature simulation is very large and currently can only be done using large approximations which yield inaccurate results brought about by the phonon distribution shifting to a high energy states. The simulation does however seem to work well at low temperatures (<100K) providing reasonable thermal conductivity values and showing that the simulation can maintain an equilibrium distribution at temperatures of around 30K using a reasonable number of particles.

Chapter 6

Nanowire simulation

Nanowires are structures with a length to width ratio of 1000 or greater, where the width is of a nanometre length scale, hence they are commonly referred to as one dimensional systems. These structures have been synthesised in several materials including metallic (e.g. Ni [79]), semiconducting (e.g. Si [9]) and insulating (e.g. SiO_2 [80]). A semiconductor nanowire has a regular crystal structure with nanoscale boundaries unlike the nanotube [81].

Semiconductor nanowires are swiftly becoming an important component in the development of nanoscale semiconductor circuits. Their use in transistors can increase speed up to four times [82], while doping characteristics allow them to be used in passive diodes and complementary inverters [83]. As a result of growing interest in their potential applications they have received considerable attention in terms of electron transport [84], electrothermal phenomena [85,86] and heat transport [87].

6.1 Nanowire thermal conductivity

The classic method for calculating nanowire thermal conductivity is a derivative of Klemens' and Callway's techniques [32] (equation 3.4) seen in [87,88]. More recently the unique geometry of the nanowire has led to the use of MC simulations [77,78] using a derivative of Mazumder's [36] method which can include an explicit description of boundary scattering. This method is discussed further in section 6.3.1.

6.2 Analytical solutions

If we apply boundary conditions to the the thermal conductivity calculations shown in section 3.6.1 and those in Holland's work [11], we can see the effect of nanoscale geometries on the thermal conductivity. We start by making the assumption that the probability of boundary scattering in a nanowire is given by:

$$P_{bscatt} = \frac{F v_g C}{A}, \tag{6.1}$$

where v_g is the group velocity of the phonon, C is the circumference of the nanowire, A is the cross-sectional area and F is a roughness factor. This can be simplified to

$$P_{bscatt} = \frac{4 F v_g}{d} \tag{6.2}$$

where d is the diameter of the nanowire. Equation 6.2 corresponds to the boundary scattering term used by Holland, as described in section 3.2.1. The relaxation time is evaluated as

$$\tau^{-1}(q, LA) = P_{bscatt}(q, LA) + \tau_L^{-1} \tag{6.3}$$

$$\tau^{-1}(q, TA) = P_{bscatt}(q, TA) + \tau_T^{-1} \tag{6.4}$$

where τ_L and τ_T are calculated using equations in section 3.2.1 for Holland's relaxation times and section 3.6.1 for the recalculated phonon relaxation times.

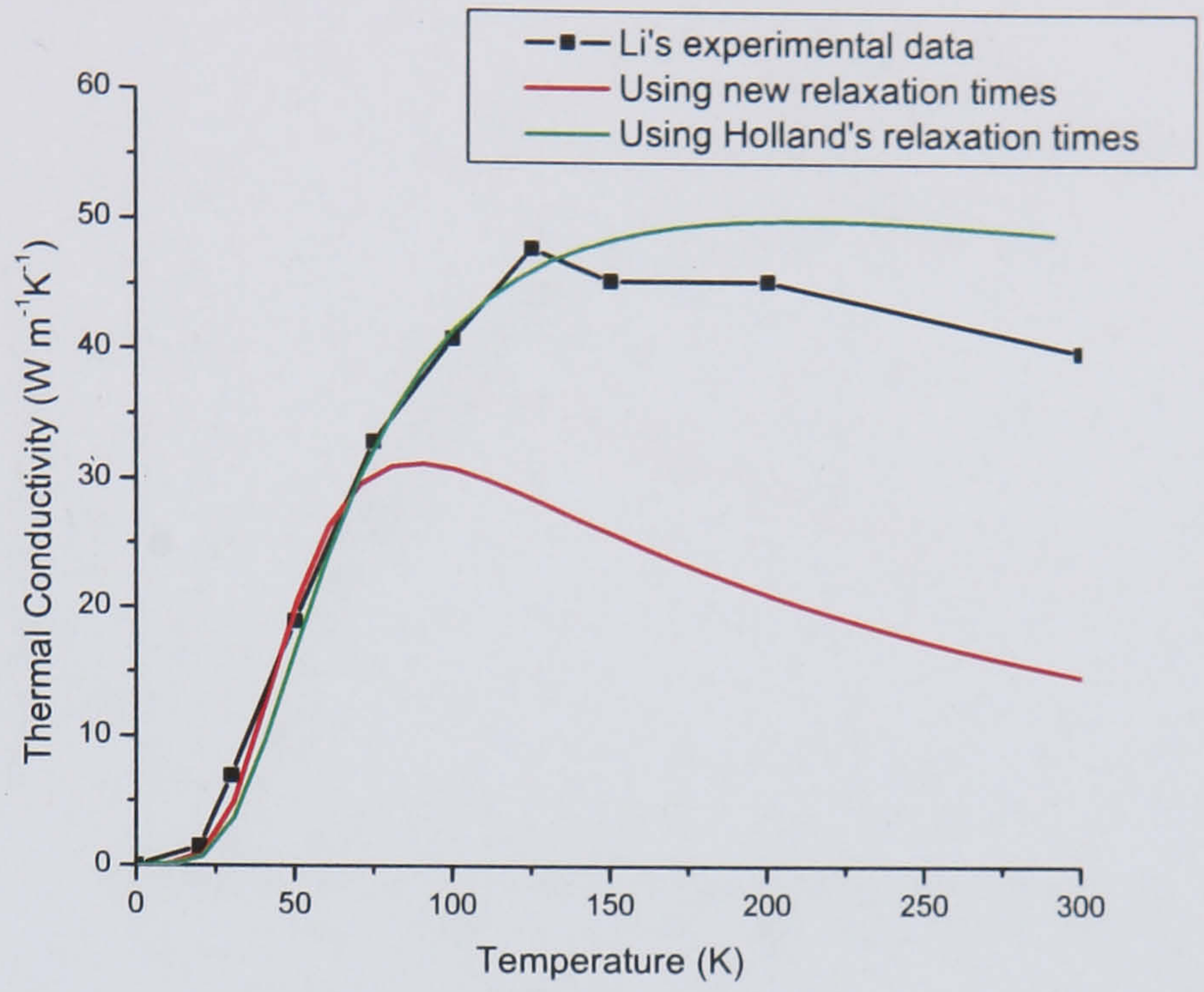

Figure 6.1: Thermal conductivity values from calculation and experiment for a nanowire of 115nm diameter.

6.2.1 Results

Figures 6.1, 6.2 and 6.4 show thermal conductivity for nano-wires of 115, 37 and 22 nm diameter. The equations are calculated using the dispersion curves shown in appendix E.2. F is a fitting parameter chosen to match the low temperature thermal conductivity, upon which anharmonic interactions have little effect. Agreement with experimental low temperature thermal conductivities was achieved by setting $F = 1/10$ for Holland's relaxation times and $F = 1/12$ for the recalculated relaxation time values. Experimental data was taken from Li [9].

Figures 6.1 and 6.2 show that by using Holland's [11] relaxation times, a good low temperature result can be derived. Figures 6.1 and 6.2 show that for the 115nm diameter nanowire, the results match the experimental results very well up to 100K. Above this temperature the calculation overestimates the thermal conductivity. The results for the 37nm diameter nanowire show similar characteristics. The model matches experimental values up to temperatures of 200K; above this temperature the model overestimates

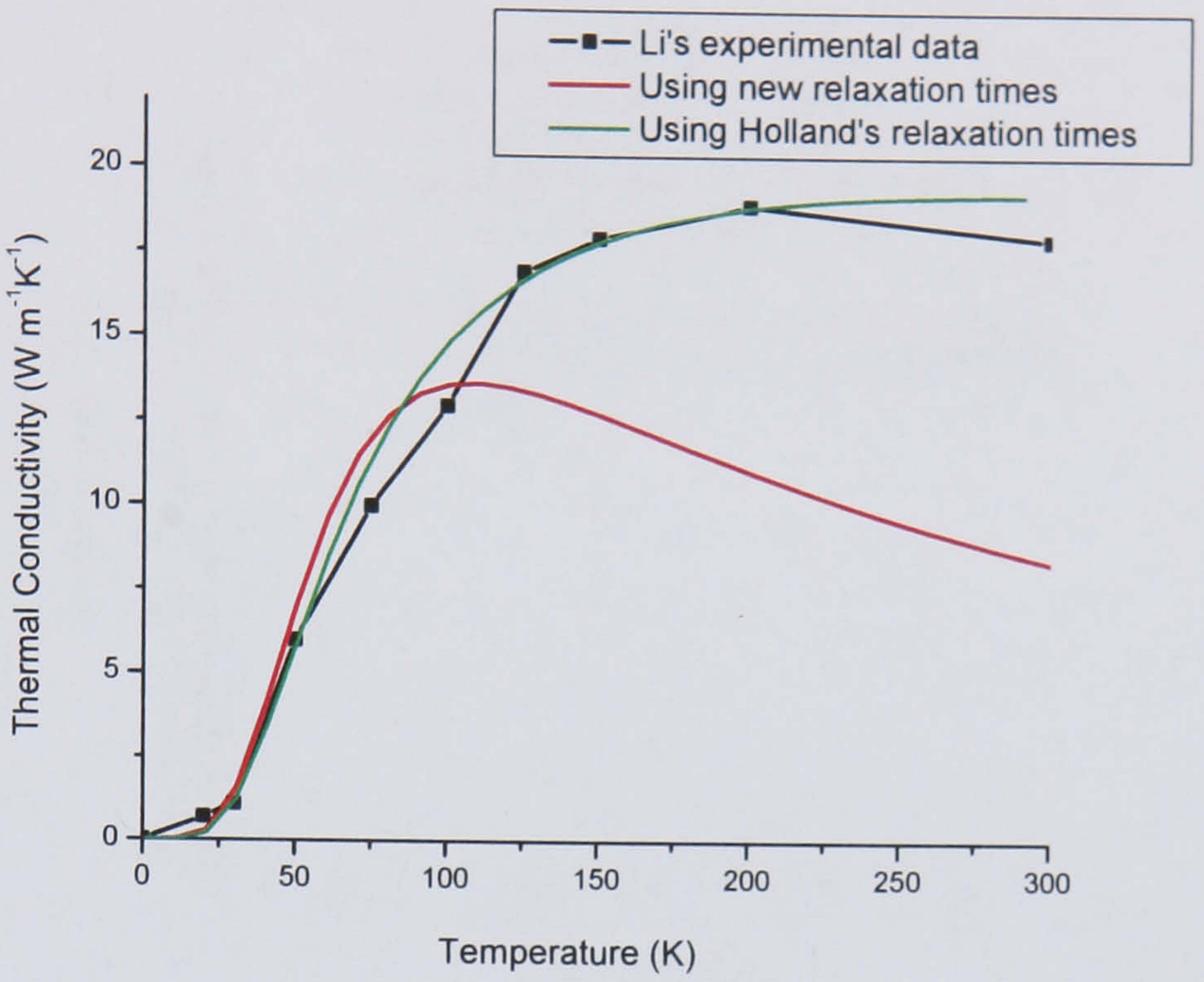

Figure 6.2: Thermal conductivity values from calculation and experiment for a nanowire of 37nm diameter.

thermal conductivity.

When using the relaxation times, derived in chapter 3, for the thermal conductivity calculation, the agreement with experiment applies only up to a much lower temperature. The validity of this model for a 115nm diameter wire only extends up to 70K. Above this temperature the thermal conductivity is underestimated. For the 37nm wire the upper limit of validity is only 50K.

In figure 6.3[1] we can see the effect of the different types of scattering at room temperature on LA phonons. As the diameter of the nanowire decreases, the boundary scattering rate increases. It has been shown in section 3.6.1 that the LA phonon branch is primarily responsible for heat transport above 100K. Figure 6.3 shows that the anharmonic scattering rates of the LA phonon branch at 300K, for both the Holland approximation and the new scattering rates calculated in chapter 3, compared to the boundary scattering rates. The effect of boundary scattering is more dominant when

---

[1] The boundary scattering shown in these graphs is for $F = 1/10$, boundary scattering will have less of an influence in the new relaxation time model.

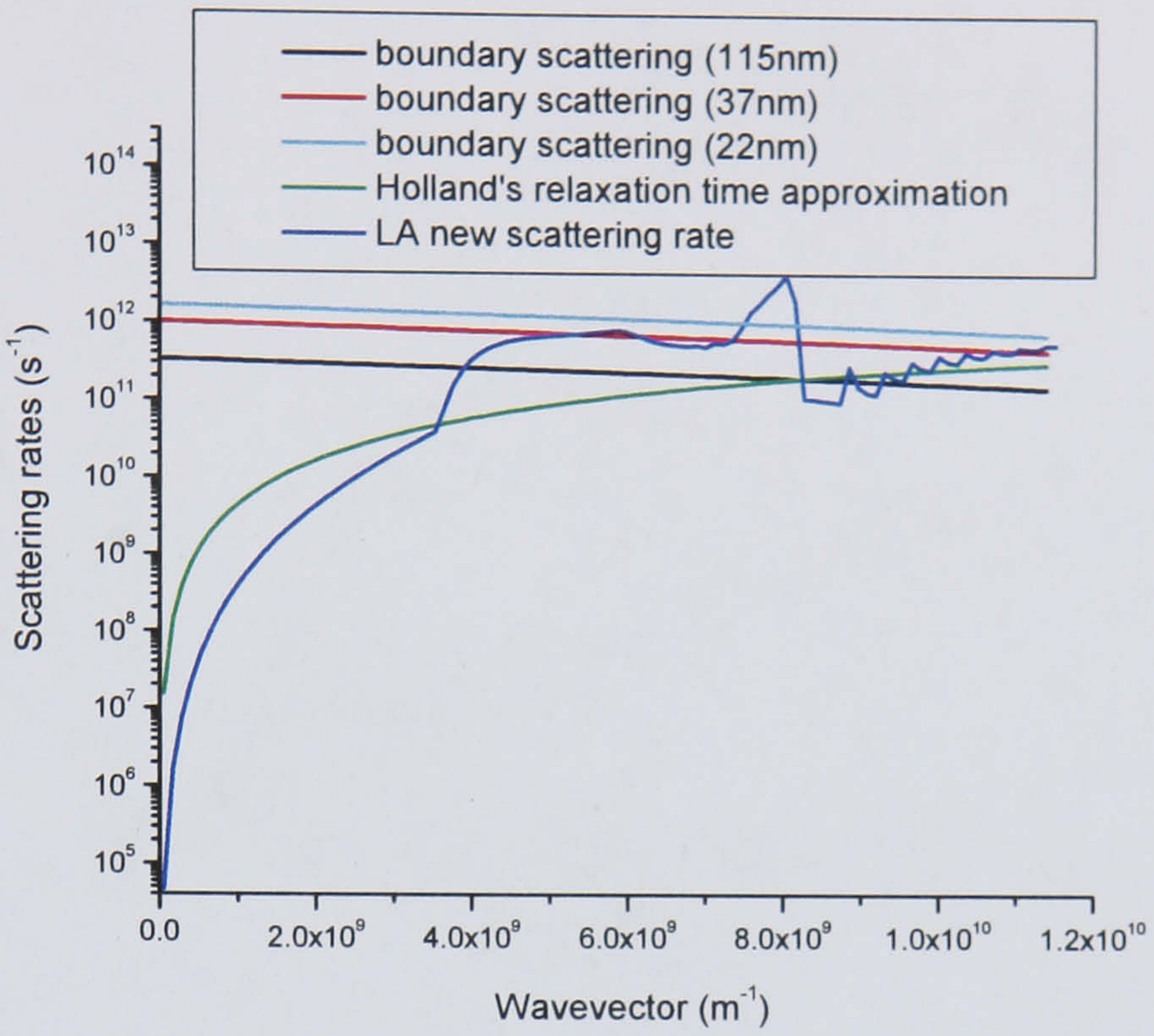

Figure 6.3: Scattering rates in a nanowire for LA phonons at 300K.

using Holland's scattering rates. The overestimation of thermal conductivity at this temperature is due to the fact that Holland's scattering rates do not cater sufficiently for anharmonic scattering (discussed in section 3.6.1). The underestimation in thermal conductivity in the calculations performed with the new relaxation times can be seen as a consequence of the the large influence that anharmonic interactions still have, despite the increased boundary scattering.

The constant temperature boundary scattering does not appear to work for the new relaxation times, but it does seem to work reasonably well when using Holland's relaxation times, although these lead to overestimation of thermal conductivity for bulk silicon (see section 3.6.1). It may be that the reasonable agreement with experiment shown by Holland's calculation for nanowires, is a coincidence.

Asheghi [89] has shown that using temperature independent boundary scattering methods cannot accurately predict the changes in thermal conductivity caused by boundary conditions in microscale thin films. The implication of his prediction is an underestimation of thermal conductivity at low temperatures. This may indicate that

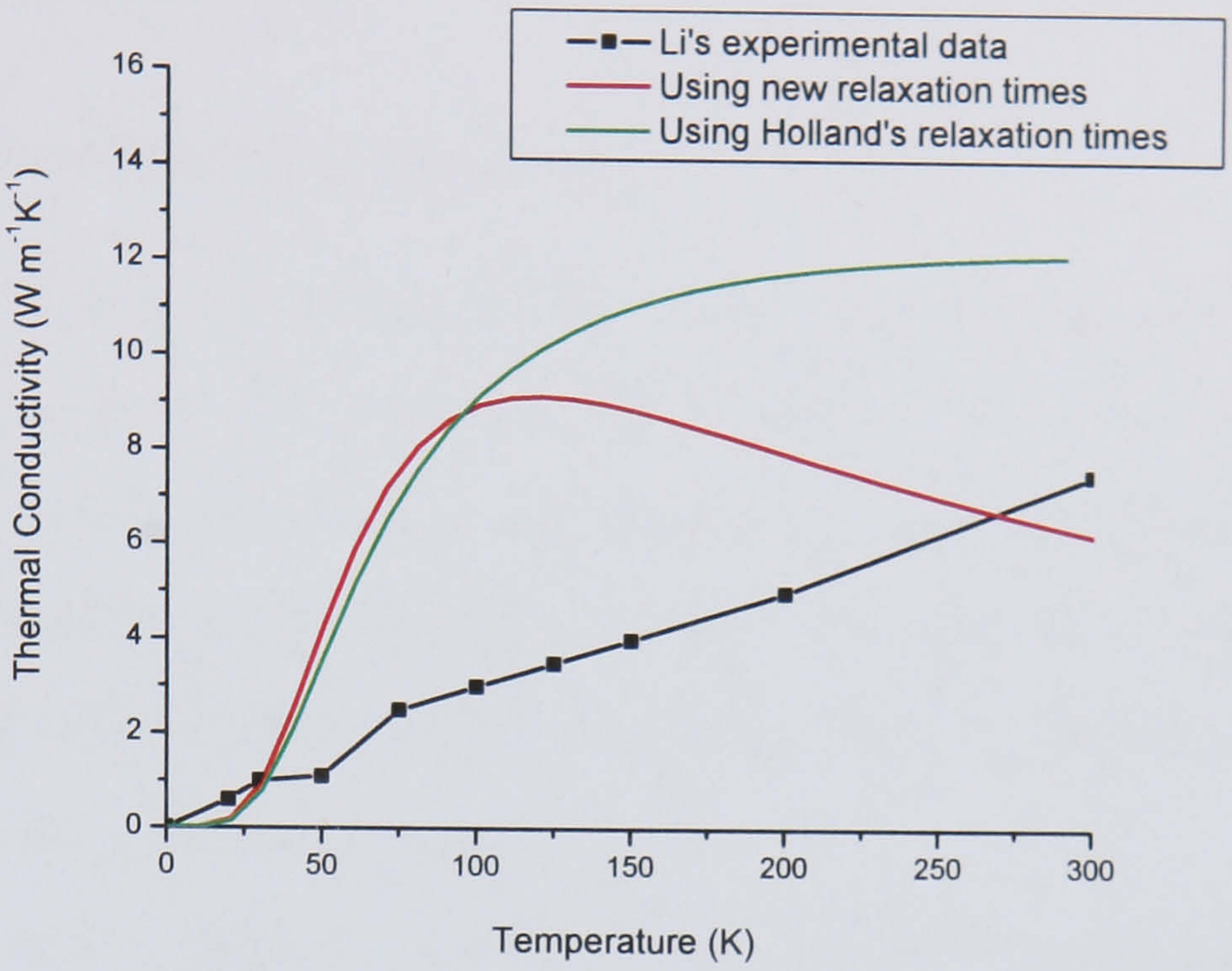

Figure 6.4: Thermal conductivity values from calculation and experiment for a nanowire of 22nm diameter.

there is a temperature dependence of boundary scattering that is not a direct result of the change in phonon distribution. Some investigation is being done on this possible relationship [90], however no published results are available.

Figures 6.1 and 6.2 show that for certain nanowire diameters, analytical models can provide a reasonable approximation to the thermal conductivity; however figure 6.4 shows, for a 22nm, a large disagreement with experiment. Both methods seem to produce significantly higher thermal conductivity values throughout the temperature range shown. This breakdown of traditional models, using bulk silicon dispersion curves, is expected for small nanoscale diameters, due to the onset of phonon confinement effects. Indeed Li [9] states that phonon confinement becomes significant at approximately 22nm. This issue is discussed further in section 6.4.

6.3 MC solution

6.3.1 MC boundary conditions

Zou [88] shows, using a modified Callaway model, that for nanowire geometries, anharmonic interactions are less important than boundary scattering. The application of Holland's model to nanowire geometries supports this conclusion although the method used to describe boundary scattering in the analytical models is still an approximation. Both Chen [78] and Mazumder [36] include a description for boundary scattering, which Chen goes on to use in nanowire simulation.

The common way to include boundary roughness scattering in a particle based simulation is to use a roughness variable set between zero and one [36,78]. When a collision with a boundary occurs a random number between zero and one is generated, if the number is greater then the roughness variable the particle is specularly reflected (as in section 4.4.5), however if the number is less, then a simple algorithm is employed where the particle is diffusively reflected with a random determination of the wavevector direction. This method was applied to the non-momentum conservation MC simulation developed for application to nanowires.

6.3.2 Results

A silicon nanowire was modelled using a cuboidal geometry, corresponding to the shape of the material wells discussed in section 4.4.2. The nanowires simulated had the same cross sectional areas as those measured by Li [9]. However it should be noted that, as a consequence, the perimeter of the cross section is approximately 20% larger then that of Li's cylindical wires. The length of the material simulated is only a fraction of the nanowire length that is used in Li's [9] experiments as the simulation of a full length nanowire would be extremely computationally expensive. The simulation uses isothermal walls on either end of the material and the difference in wall temperatures is set at

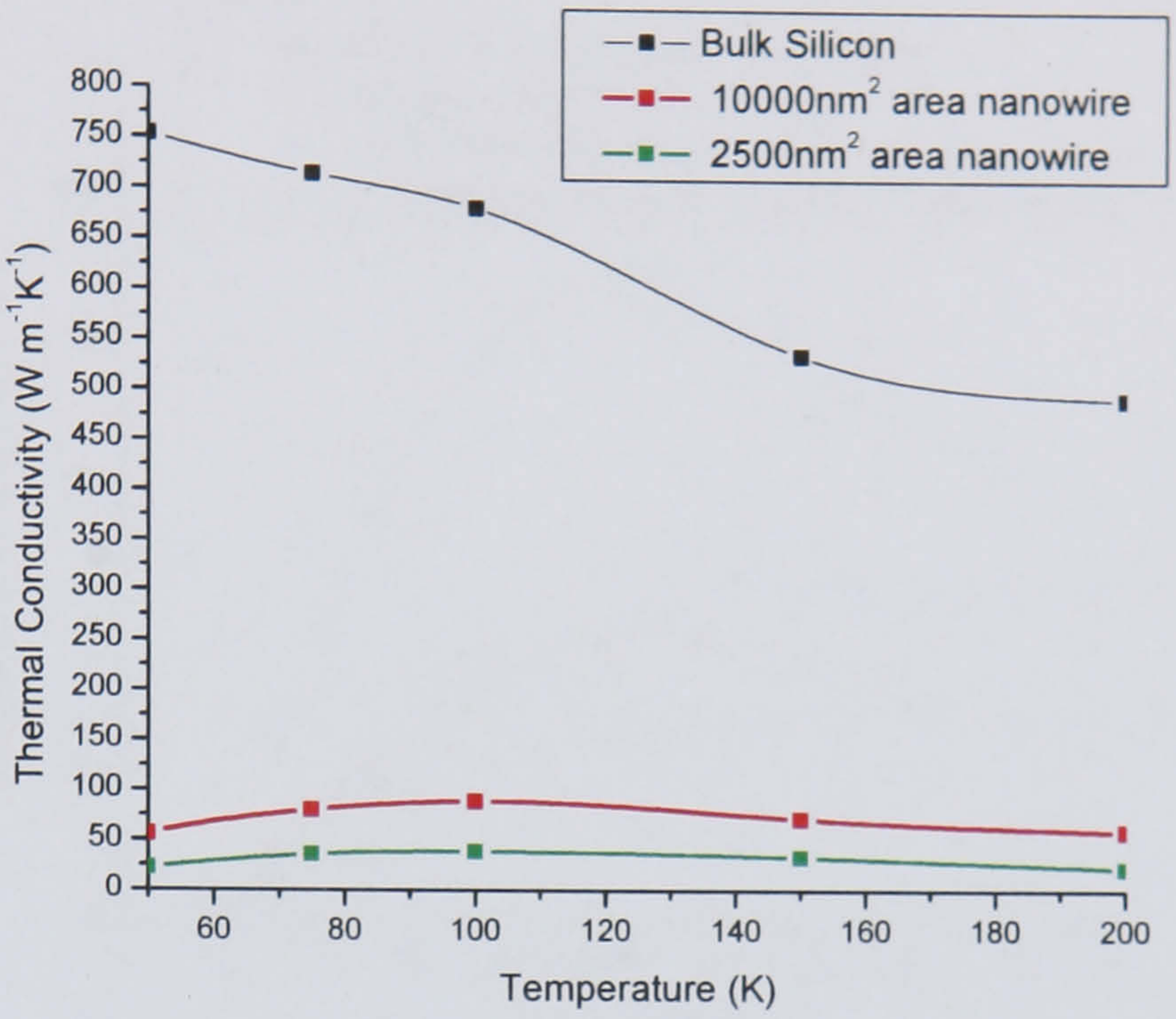

Figure 6.5: Thermal conductivity extracted from MC simulations of silicon at different material dimensions.

20K. The specular reflection coefficient is calibrated to 0.4 in order to give a reasonable match to Li's experimental results at 200K. The resulting thermal conductivity as a function of temperature is shown in figure 6.5.

6.3.3 Analysis

Figure 6.5 shows that results from the MC simulation developed in chapter 4 (which uses the relaxation times calculated in chapter 3) when applied to bulk silicon and to nanowires with the boundary conditions described above. This figure shows that the MC solution predicts correctly the reduction in thermal conductivity as nanowire shrinks in width.

Figure 6.6 compares the results achieved from the MC simulation seen in figure 6.5 to the experimental results that Li [9] reports. Though there is some discrepancy between MC results and the experimental results, the trend seen in the thermal conductivity verses temperature is correct. The MC simulation predicts that the change in thermal

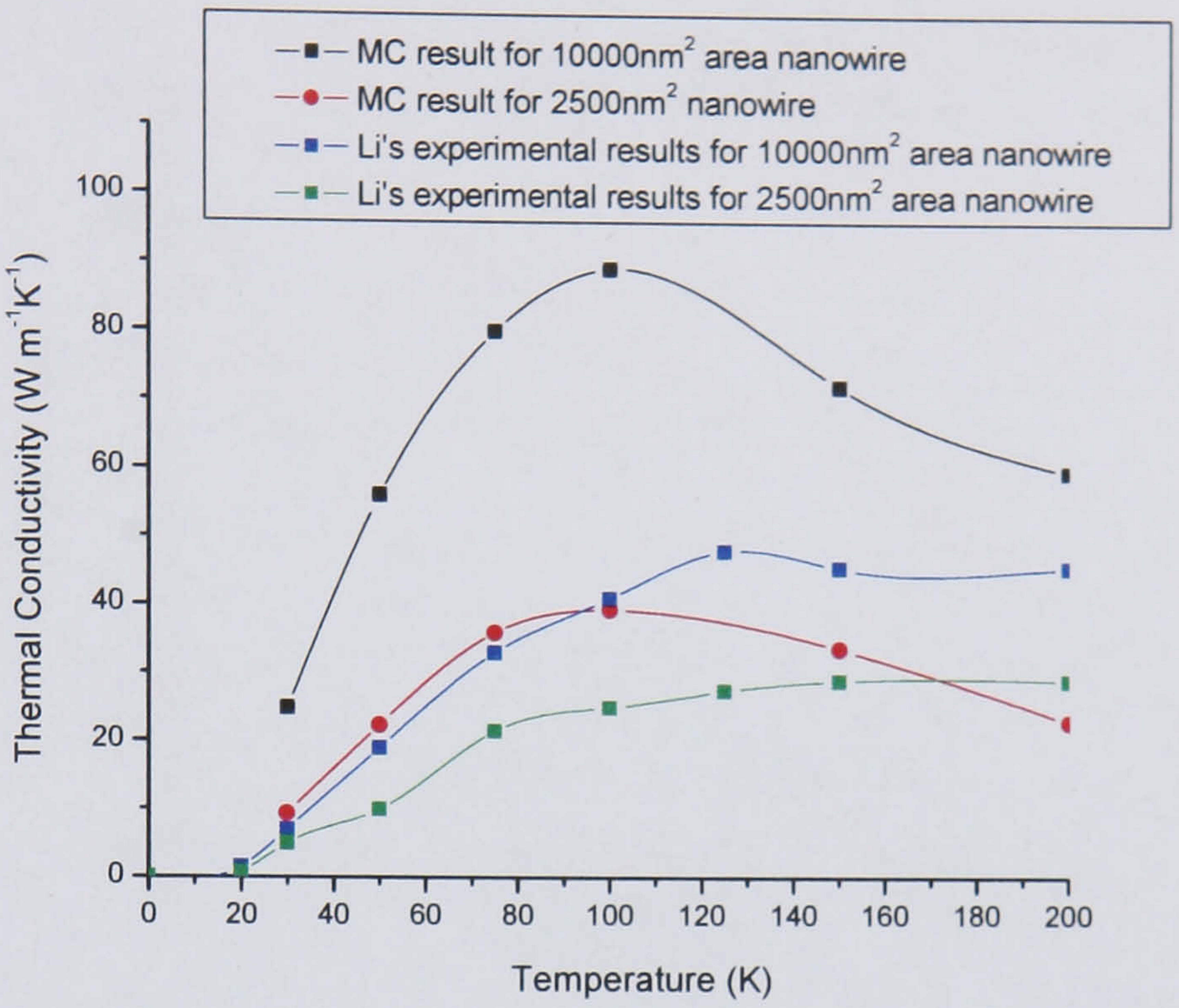

Figure 6.6: Nanowire MC simulation results for nanowires compared to Li's [9] experimental results.

conductivity will increase to a peak value at about 100K and decrease thereafter; the experimental results for the 10,000nm^2 cross-sectional area nanowire shows this effect clearly.

There is an overestimation of the peak thermal conductivity extracted from the simulation seen in figure 6.6 which leads to a variable error from the experimental results. The reason for this discrepancy is possibly the simplistic definition of boundary scattering that is temperature independent.

The Monte Carlo method in this case differs from the experimental values as with the use of the MC method in chapter 4. The use of calibrated boundary scattering to give a closer representation of the thermal conductivity values affects the thermal gradient. Though the thermal gradient is not expected to be linear at such small geometries, the result of the simulation at steady state deviates significantly. Figure 6.7 shows the thermal gradient from the 115nm simulation.

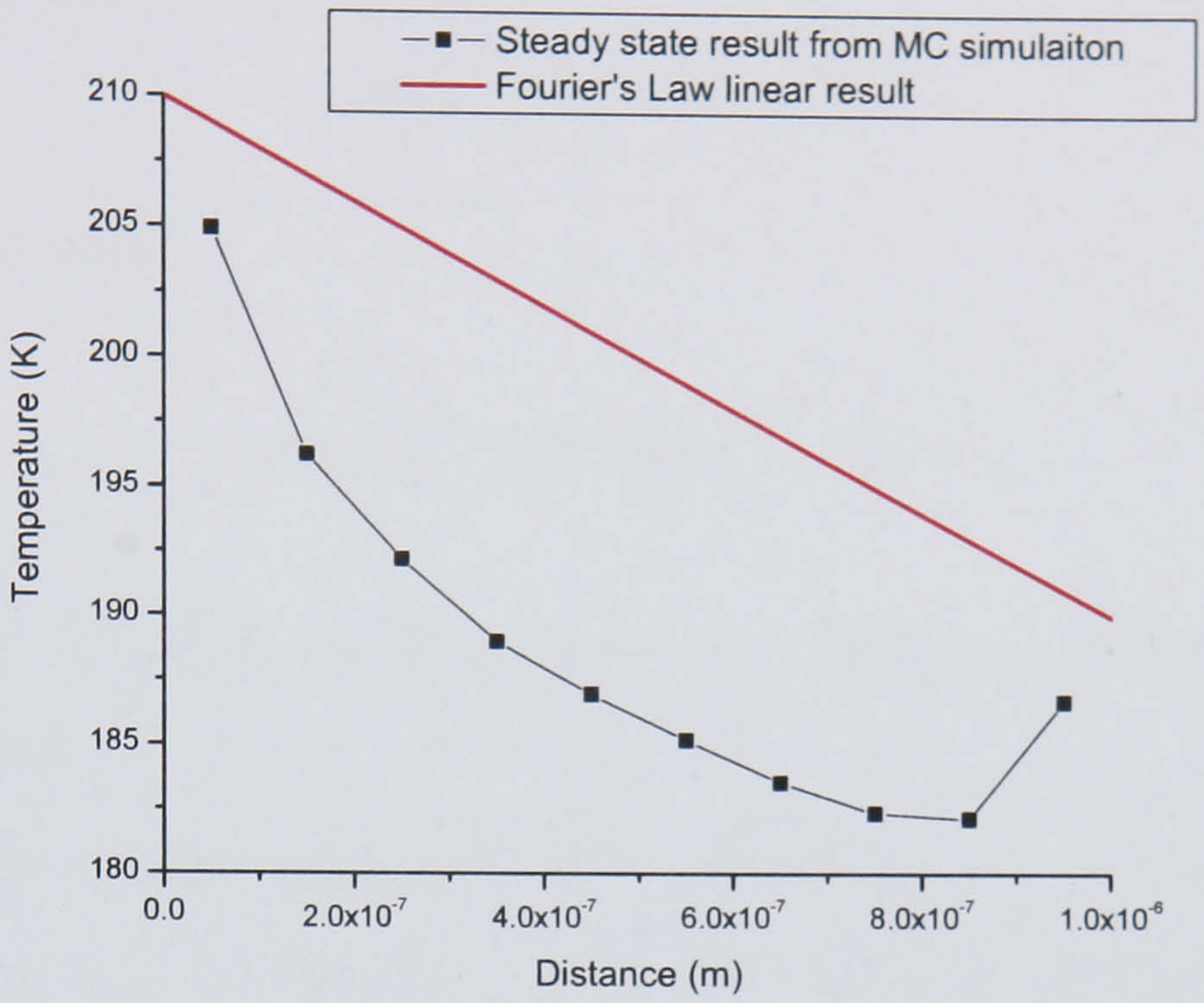

Figure 6.7: Thermal profile for 115nm nanowire simulation.

6.4 Confinement

As a nanowire diameter is reduced, phonon confinement comes into effect. This results in a change of the phonon dispersion relation and thus effects the thermal conductivity. Li [9] states that phonon confinement effects are not significant until the nanowire diameter is less than or equal to 22nm. The changes in dispersion are discussed in depth in [91].

The confined phonon modes include longitudinal, torsional and flexural. Chen [78] derives a simplified dispersion relation for nanowires using the method described in [92] for cylindrical acoustic waveguides, resulting in the equation

$$\omega_n = v_{l,t}\sqrt{q^2 + q_{(l,t)n}^2} \tag{6.5}$$

where the index n indicates the different phonon modes, $v_{l,t}$ is bulk phonon velocity for longitudinal and transverse modes respectively. q_l and q_t can be derived from

$$(q^2 - q_t^2)^2 \frac{(q_d R) J_0(q_d R)}{J_1(q_d R} - 2q_d^2(q_d^2 + q_t^2) + 4q^2 q_d^2 \frac{(q_t R) J_0(q_t R}{J_1(q_t R)} = 0 \tag{6.6}$$

for longitudinal modes,

$$q_t R J_0(q_t R) = 2J_1(q_t R) \tag{6.7}$$

for torsional modes and

$$J_1(q_d R) J_1^2(q_1 R)\phi(q_d, q_t, q, R) = 0 \tag{6.8}$$

for flexural modes. J_0 and J_1 are Bessel functions. The uses of these dispersion curves are set out in [93, 94].

Chen [78] states that at small wavevectors the velocity of the longitudinal phonon is the same as that for a LA phonon in bulk, however as the wavevector increases the group velocity becomes much smaller. The torsional and flexural branches have group velocities, for the most part, smaller than that of the TA branch. These changes lead to an overall decrease in thermal conductivity.

Zou [88] uses the above confinement dispersion curves to develop an analytical model, based on Callaway's [32] method, which is valid on the lengthscale where phonon confinement occurs. He also takes the effects of the smaller geometry into account with derivation of a "deviation in thermal conductivity" value which is determined from mean free path and wire diameter. This value is evaluated with a parameter that is tunable for diffusive boundary scattering. Zou experiences some success with modelling nanowire thermal conductivities though makes no clear comparison with experiment.

Chen applies the above dispersion relation calculation for use with his MC model in order to simulate small-diameter nanowires. Chen shows clearly that the application of these curves to his simulation make a clear difference to the thermal conductivity values extracted.

6.5 Discussion

In the structure of a nanowire, Holland's analytical methods still provide a good approximation of thermal conductivity for wire dimensions greater than those of the confinement regime. With the inclusion of confinement and the use of representative dispersion data, the application of these methods can be extended significantly into the nanoscale regime as shown by Zou [88].

Though Holland's methods provide a good approximation for nanowires, when applied with our new scattering times,the same approximation seems to show a significant error despite the closer match to experimental data in bulk silicon. This work seems to indicate that the traditional temperature independent boundary scattering terms are insufficient for use in nanoscale geometries and that the good agreement obtained from Holland's relaxation times must be somewhat fortuitous.

The current MC methods employed in this work do not exactly predict the experimental results shown by the work in Li's [9] measurements. The results shown in this chapter indicate that the MC solution does produce the correct trends for both the changes in thermal conductivity with nanowire diameter and the changes in thermal conductivity with temperature at these reduces sizes. With a more accurate MC model, investigation for these complex nanowire device structures could be attempted.

In nanowires the boundary effects seem to be so dominant that, in both cases (the analytical and the MC simulation) the simple models of boundary interactions are likely to be inadequate. In a real system there would be radiative heat transfer resulting in heat loss from the nanowire. In addition to this, surface roughness will not only cause simple diffusive or adiabatic reflection, presumably it will cause some phonon scattering (decay and merge).

The simple approximations used in the analytical calculations described above could not predict accurately heat transport in structures such a nanospheres, dots and shells due to the complexities of the boundary geometry. However, the incorporation of specific dispersion relations caused by phonon confinement in these different structures should allow an MC algorithm to predict their thermal transport.

Chapter 7

Conclusions

7.1 Summary of achievements

The work presented in this thesis shows the development of several Monte Carlo simulations to model heat transport in semiconductor materials. Although there are some shortcomings associated with these approaches, these models do provide a better description of heat transport.

7.1.1 Anharmonic interaction

In chapter 3, using techniques used in phonon imaging calculations [61, 69, 95], new scattering rates for acoustic phonons were calculated using a realistic dispersion relation. These techniques provide a more accurate picture than the more traditional scattering rates derived in previous works [11, 32, 34, 63, 96]. The derivation of these scattering rates are in terms of second and third order elastic constants from the Hamiltonian of the 3 phonon process.

This new scattering rate model predicts a significantly larger influence of the Umklapp processes than in previous work done by Holland [57], predicting a decline in influence only at very low temperatures. The model produces scattering rates for each individual type phonon-phonon interaction, hence providing more detail than his calculations. The new scattering rates were first used in an analytical calculation of thermal conductivity; these were found to give better agreement with experiment for bulk silicon then those rates obtained by Holland.

7.1.2 Monte Carlo simulation

Phonon transport does not have an associated drift current, unlike electron transport, and is a direct result of diffusion which is inherently more difficult to simulate using MC methods. Without the direct application of a bias on particle movement, such as an electric field on carriers, the movement of these particles is more erratic and hence the results produced are noisier. The importance of maintaining an equilibrium distribution in an isolated system is apparent due to this lack of a driving force in the simulation.

Non-momentum conservation Monte Carlo simulation

An investigation of Mazumder's MC technique was reported in chapter 4, in which some limitations of the methodology were discussed. The main shortcoming of Mazumder's method is the shift in the phonon distribution to lower frequencies, which is caused by the method used for re-introduction of phonons into the simulation after scattering.

Two attempts were made to rectify this shift with varying success. The first attempt uses a phonon histogram to bias the re-population method. This method does reduce the shift of the phonon distribution with some success; however there is still a small deviation from equilibrium. The benefits of this method were highly out-weighed by the additional computational expense involved. The second attempt uses Kirchhoff's law to ensure that the phonon distribution will always tend towards equilibrium. The relaxation times used for this method were determined from the third order potential energy expression (from chapter 3). This method solves the phonon shift problem and yields the best thermal gradient at low temperature differences.

All the methods investigated tend to overestimate the thermal conductivity, although Mazumder's [36] published results do not. The reason for this difference is unclear.

Momentum conservation Monte Carlo simulation

A MC method was developed using a momentum conservation scattering method described in chapter 5. This method simulates the 3-phonon process by monitoring the wavevectors of individual phonons and ensuring that momentum and energy will be conserved in any interaction. Merge processes requires selection of another phonon within a defined area. Phonon scattering rates are calculated based on the local phonon distribution defined within the allowed interaction area.

It has been previously postulated that such a solution will be too computationally expensive [78]. The method developed utilised simple algorithms in order to reduce computational expense (see section 5.1.1); however this reduction proved to be insufficient for high temperature simulations, given the computational power available.

The ensemble population required for this method is much larger then used in other MC simulations discussed in chapter 4. Without this increase in population the correct scattering opportunities are not available to accurately model phonon distribution changes. This was due to the requirement for energy and momentum conservation to be maintained between two existing particles in the 3-phonon merge process. The larger population increased computational time. At high temperatures (<100K) the computational power required to simulate the large quantity of scattering events is much higher than that for low temperatures.

Application of this method using an ensemble population which is computationally feasible produces results which are relatively good. It is shown that the method does maintain an equilibrium distribution at low temperatures and produces reasonable thermal conductivity values at temperatures below 100K for bulk silicon.

7.1.3 Nanowire

Application of recalculated phonon scattering rates, when applied to Holland's thermal conductivity calculations, shows a distinct deviation from experiment. There is a similar deviation shown in the application of the non-momentum conservation MC simulation.

The results produced show that the effect of the nanoscale boundaries produce the correct trends in the extracted thermal conductivity values. The MC simulation shows that as the diameter of a nanowire decreases so does the thermal conductivity across all temperatures. The simulation results also show that thermal conductivity values are significantly smaller for a nanowire than the bulk values. The temperature dependence of the thermal conductivity also shows that there is a peak thermal conductivity situated at approximately 100K.

Though these trends are correct, some fine tuning needs to be done on the simulation, including the implementation of boundary scattering. The application of temperature independent boundary scattering is shown to underestimate thermal conductivity at low temperatures where the influence of anharmonic interaction is negligible. It can also be assumed that at nanoscale dimensions, where the effect of boundary scattering is the dominant scattering method, simple diffusive and adiabatic scattering does not fully represent the effect on phonons. As a result more work needs to be done on a temperature dependent application of boundary scattering.

7.2 Further work

The results and method discussed in this work represent steps toward the development of more detailed heat transport models. Most of the problems encountered in this work are likely to be resolved with some further changes to the algorithmic methods which are outlined below and which have been discussed in other related works.

7.2.1 Anarmonic interaction rates

Chung [37] discusses how the accuracy of the dispersion curve can effect the thermal conductivity calculations. The spline approximation used does provide a substantially better approximation then the linear approximation used in Holland's [57] work. However dispersion is shown to have a temperature dependence [97]; a temperature dependent model of dispersion combined with the temperature changes to the elastic constants [10] should correct the underestimation of the thermal conductivity at temperatures above 250K. The isotropic spherical approximation of the Brillouin zone and the use of Tamura's [61] isotropic recalculation of the elastic constants may also cause some discrepancy.

Narumanchi [40] has shown that 3-phonon processes involving optical phonons may be important in the solution of the BTE for phonons. Though the effect may be small, due to the short lifetimes and low mobility of the optical branches, inclusion of these transitions is required in electrothermal coupling due to electron-phonon scattering.

Doping is an essential part of semiconductor device manufacture. The effect of impurity scattering in bulk material can have a significant effect based on the doping density. The presence of dopants will reduce the thermal conductivity by causing phonon collisions.

7.2.2 Monte Carlo techniques

Further investigation into the use of the MC methods for heat transport needs to be carried out as the methods investigated in the work show large deviations from experimental results. Improved momentum conservation algorithms need to be employed in order to provide a more accurate description of thermal conductivity, especially at nanoscale dimensions. Use of methods which directly cater for momentum and energy conservation have been proven to be incredibly computationally intensive, requiring further development to use with parallel computing resources or significantly higher powered machines than are currently available. To reduce the computational power required and to provide a more accurate representation of phonon scattering a middle ground needs to be found. Applications of indirect momentum conservation attempts have been used in Chen's [78] and Lacroix's [77] work. These methods introduce other errors and should be examined in more depth.

Improvements to the anharmonic scattering rate calculations discussed above can also be applied to the MC solutions with a different methodology. As stated optical phonons are important in electrothermal coupling; their inclusion in phonon transport simulations could have a much greater effect in nanoscale systems as, due to their low mobility, optical phonons will not be affected by boundary scattering. As the MC solution is most useful when applied to irregular geometries and small structures where the phonon distribution is in constant flux, the importance of simulating impurity scattering increases as this will cause further deviation from equilibrium.

Application to simple isolated structures is useful; however to model real devices, more realistic boundary conditions will need to simulated that will allow heat transport between material layers. Cahill suggests that an acoustic mismatch model (described in [26]), which will provide a thermal boundary resistance, can be used to simulate this. This will allow the simulation of multilayered devices such as HEMTs. For nanoscale structures where phonon confinement effects the MC algorithm must be further modified to account for the scattering rates and dispersion curves appropriate for the confined phonon modes. This issue has been investigated for nanowires [78], however further work will be required for other geometries.

7.2.3 Electrothermal integration

The ultimate aim of this work is the self-consistant nanoscale simulation of both electronic and thermal transport. In principle, this can be achieved straight-forwardly by simultaneously simulating phonons and electrons. In practice there will be a number of problems which will need to be overcome. In any semiconductor structure under normal operating conditions, the number of phonons will be much larger then the number of electrons. To simulate electron-phonon interaction directly, scaling should be the same across both populations; this will allow energy and momentum conservation to be taken into account. This would be completely impractical as the number of particles which would be required for an accurate model would be very large and will require substantial computational time and power. In addition to this the timescales for electronic and thermal transients are very different; synchronisation between the two populations will provide noise in both.

7.3 Outlook

With more complex structures and use of new materials thermal management is becoming increasingly important. Standard analytical models using the heat diffusion equation will not hold up as the dimensions of structures decrease and phonon confinement becomes more of an issue.

Though the models discussed in this work do require more investigation, the techniques described do hold merit. With more efficient algorithms and better approximations these models could provide a good description of a real system. The MC model can easily be adapted to smaller structures and to include confinement effects, providing a viable heat transport model for device investigation.

Appendix A

Tensor notation

Tensor notation simplifies writing complex equations involving multi-dimensional objects. This notation is based on a set of tensor rules.

A tensor of the order m is a set of n^m numbers identified by m integer indices, each index of the tensor changes between 1 and n. So for a 2nd order tensor A, it can be denoted as A_{ij} which in 3-dimensional space will be represented by $3^2 = 9$ components. The only allowed algebra operations in tensor expressions are addition, subtraction and multiplication.

The list of tensor indices can become inconveniently large with increased order; a simple replacement introduced by Voight [98] can be used such that

$$\begin{aligned} A_\rho &= A_{ij} + A_{ji}, i \neq j \\ & A_{ij}, i = j \end{aligned} \tag{A.1}$$

where the indices ρ is related to the tensor indices (i, j) as follows:

ρ	1	2	3	4	5	6
(i,j)	11	22	33	23(32)	31(13)	12(21)

Appendix B

Holland's calculation parameters

Symbol	Value
Piecewise linear dispersion variables	
v_T(low wavevector)	5.86×10^3ms^{-1}
v_L(low wavevector)	8.48×10^3ms^{-1}
v_T(high wavevector)	2.0×10^3ms^{-1}
v_L(high wavevector)	4.24×10^3ms^{-1}
Anharmonic scattering rate parameters	
B_T	9.3×10^{-13}deg^{-3}
B_{TU}	5.5×10^{-18}s
B_L	2.0×10^{-24}s deg^{-3}

Table B.1: Parameters for Holland's thermal conductivity calculations taken from [11].

Appendix C

Random numbers

MC simulations require generation of large quantities of random numbers. Truly random numbers are only available from hardware sources, which are not easily obtainable. Traditionally, pseudo-random numbers can be obtained through complex numerical algorithms. These are sometimes preferable due to the ability to replicate a situation in software and therefore allow the ability to find and resolve problems encountered during simulation development.

A large number of these algorithms are available varying in computational compexity, range and quality of randomness. In this work, the Mersenne Twister algorithm [99] was used, which is efficient and contains a very long unique sequence of numbers.

Appendix D

Generation of random unit vectors

The generation of random unit vectors is done using the following method

$$\begin{aligned} \phi &= r \times 2\pi \\ \theta &= \arccos(2r - 1) \\ \mathbf{a}_x &= \cos\phi \sin\theta \\ \mathbf{a}_y &= \sin\phi \sin\theta \\ \mathbf{a}_z &= \cos\theta \end{aligned}$$

where **a** is the unit vector, r is a random number between one and zero and the angles ϕ, θ are the angles illustrated below.

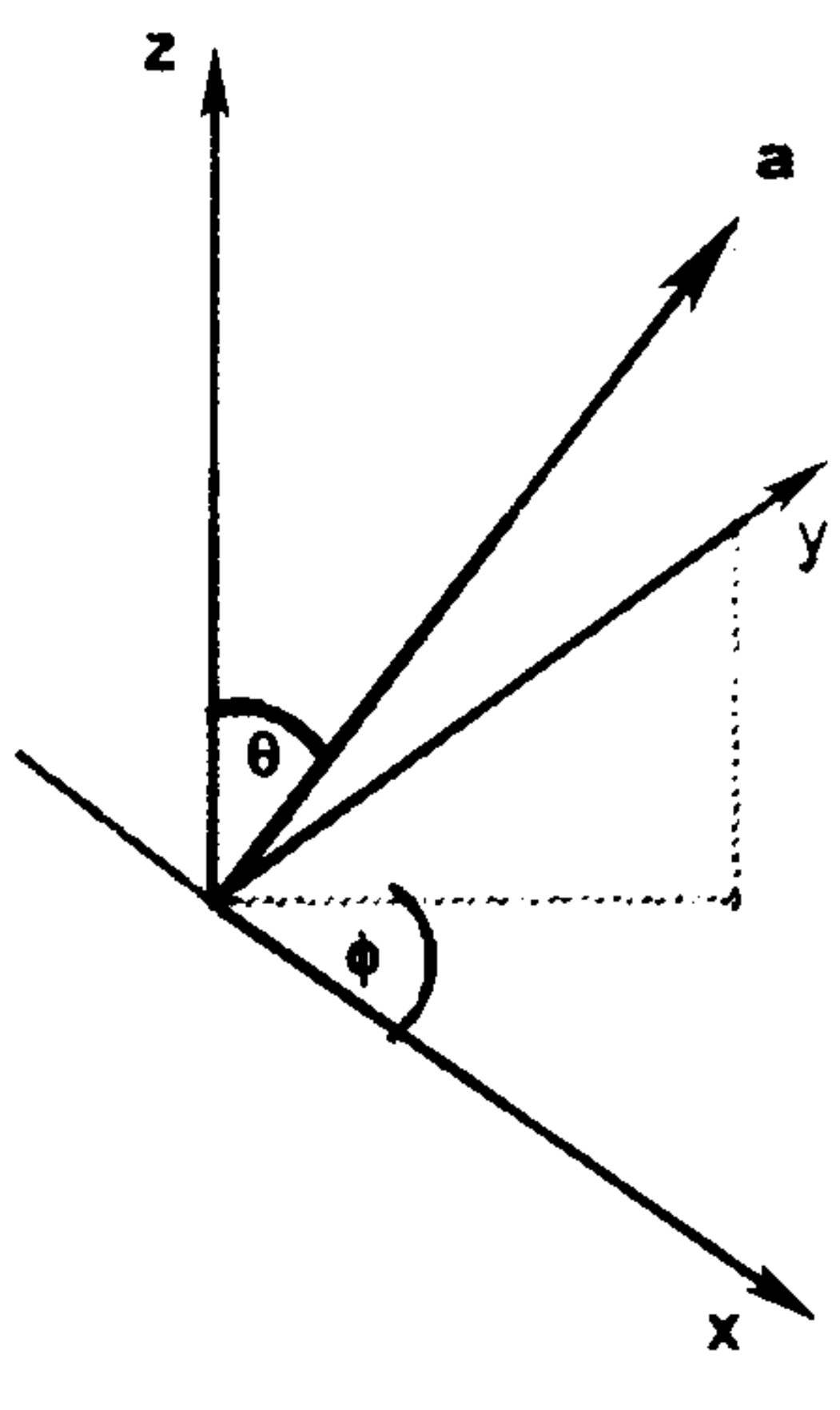

Appendix E

Spline parameters

The use of parabolic splines can reduce computational time when extracting data from complex analytical relations.

E.1 Thermal Approximation

At low temperatures, a parabolic spline cannot provide an accurate representation of the relationship between acoustic phonon energy and temperature without large percentage error. To determine the relationship below 130K, a table of values is used and the energy to temperature conversion is rounded to the nearest degree. The spline used above 130K consists of several allometric functions and a straight line above 300K. The parameters are seen below, where U is the acoustic phonon energy density and T is the temperature.

Spline curve formula	Temperature range	a	b
$U = aT^b$	130K - 180K	2712.08544	1.9841
	180K - 230K	8741.98569	1.75863
	230K - 270K	19227.3437	1.61347
	270K - 300K	17969.07721	1.62556
$U = a + bT$	300K -	-109703005.74626	996606.53191

Figure E.1 shows the spline compared to the calculated values from the equation

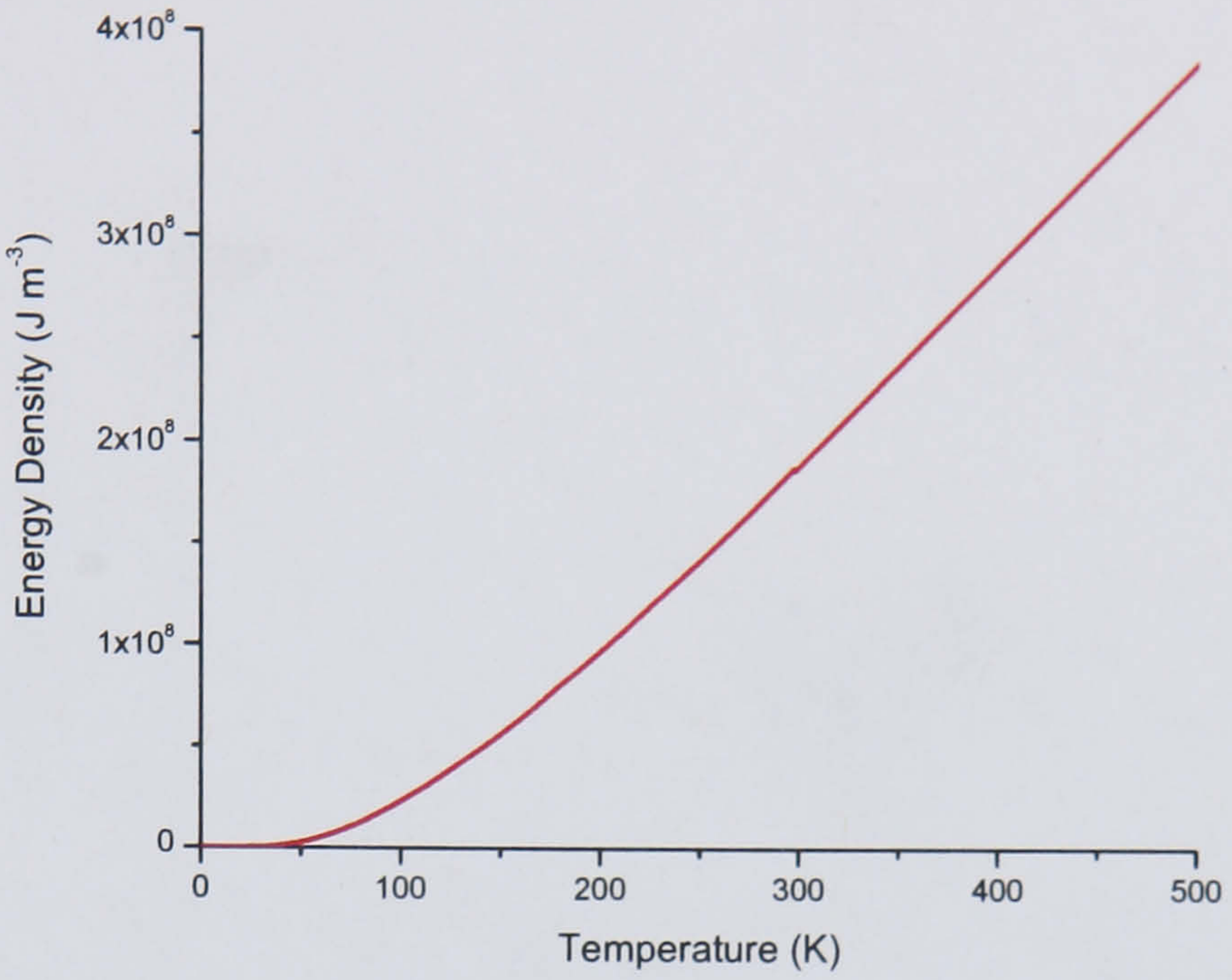

Figure E.1: The partial spline used in the the MC simulations between temperature and acoustic phonon energy density.

2.38. Figure E.2 shows the error percentage between the calculated values and the spline fitting. Though this seems to increase significantly at low temperatures, the result will only affect simulations at very low temperatures and can be easily rectified by increasing the table size below 130K.

E.2 Si dispersion curve

Figure E.3 shows the difference between the spline used for approximation and experimental values. There is a slight deviation in the TA spline, the error associated with the measurements that Dolling took could be used to justify this deviation. In these curves, each branch is approximated using only one parabolic curve such that

$$\omega(i) = aq^2 + bq \tag{E.1}$$

where the parameters are given in the following table Using these splines, we can calculate the derivative of the Dirac delta function referred to in section 3.4.3. This choice

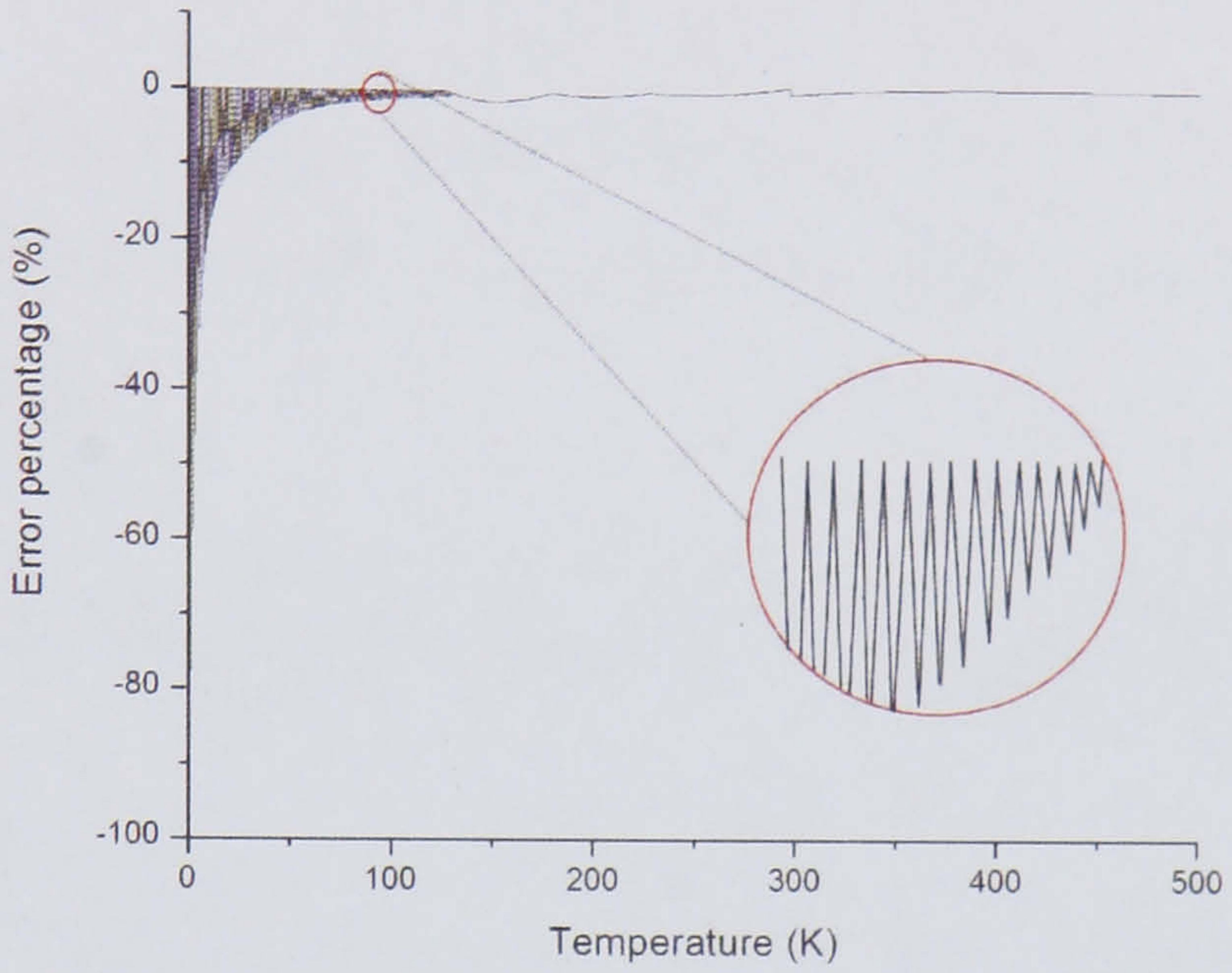

Figure E.2: The error associated with the spline used to relate temperature and acoustic phonon energy density.

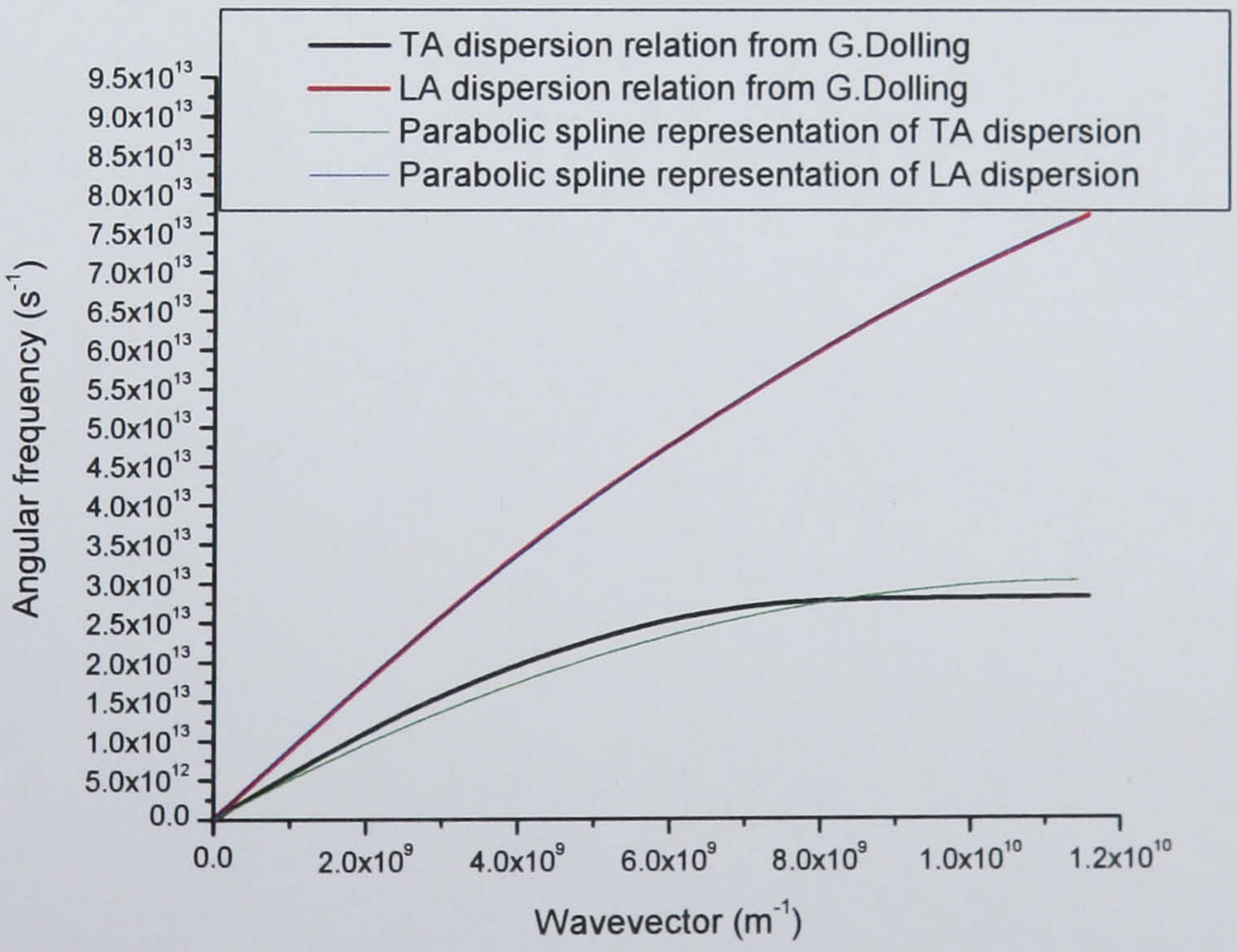

Figure E.3: Comparison of spline approximation used in calculations with Dolling's measurement in the [100] direction.

	a	b
LA	-2.2196×10^{-7}	9255.01393
TA	-2.2663×10^{-7}	5243.80552

of function is based on the polarisation of the $\mathbf{q}_3$ in the 3-phonon scattering calculation and is evaluated using the angle, ϕ, in the plain caused by $\mathbf{q}_1$ and $\mathbf{q}_2$. For TA or for normal LA scattering

$$g'(\phi) = \left(-2a\sqrt{q_1^2 + q_2^2 - 2q_1q_2\cos\phi} - b\right)\frac{2q_1q_2\sin\phi}{2\sqrt{q_1^2 + q_2^2 - 2q_1q_2\cos\phi}} \tag{E.2}$$

for LA U-processes

$$g'(\phi) = [-2a\left(G - \sqrt{q_1^2 + q_2^2 - 2q_1q_2\cos\phi}\right)]\frac{2q_1q_2\sin\phi}{2(G - \sqrt{q_1^2 + q_2^2 - 2q_1q_2\cos\phi})} \tag{E.3}$$

Appendix F

Dissemination

The following papers have been presented at scientific conferences:

A.M. Asokan and R.W. Kelsall, "Monte Carlo simulations of phonon transport in semiconductor materials.". Condensed Matter and Materials Physics Conference, University of Exeter, 2006.

A.M. Asokan and R.W. Kelsall, "Particle based simulations of phonon transport in Silicon". IWCE-11, International Workshop on Computational Electronics, Vienna University of Technology, May 25-27, 2006.

Bibliography

[1] "Intel developers forum," *http://www.intel.com/.*

[2] G. Chen, *Nanoscale Energy Transport and Conversion: A Parallel Treatment of Electrons, Molecules, Phonons, and Photons.* Oxford: Oxford, 2005.

[3] Y. S. Touloukian and T. P. R. Center, *Thermal Conductivity: Nonmetallic Solids.* Thermophysical properties of matter, New York: IFI/Plenum, 1970.

[4] H. Bilz and W. Kress, *Phonon Dispersion Relations in Insulators.* New York: Springer-Verlag, 1979.

[5] G. Dolling, "Lattice vibrations in crystals," *Symposium of Inelastic Scattering of Neutrons in Solids and Liquids*, 1963.

[6] C. J. Glassbrenner and G. A. Slack, "Thermal conductivity of silicon and germanium from 3k to the melting point," *Phys. Rev.*, vol. 134, pp. A1058–A1069, May 1964.

[7] M. G. Holland and L. Nueringer (Exeter, England), p. 474, 1962.

[8] M. Asheghi, *Thermal Transport Properties of Silicon Films.* 1999, Thesis (Ph. D.), Stanford University. Dept. of Mechanical Engineering.

[9] D. Li, Y. Wu, P. Kim, L. Shi, P. Yang, and A. Majumdar, "Thermal conductivity of individual silicon nanowires," *Applied Physics Letters*, vol. 83, pp. 2934–2936, 2003.

[10] J. J. Hall, "Electronic effects in the elastic constants of n-type silicon," *Phys. Rev.*, vol. 161, pp. 756–761, Sept. 1967.

[11] M. G. Holland, "Analysis of lattice thermal conductivity," *Physical Review*, vol. 132, p. 2461, Dec. 1963.

[12] G. Moore, "Cramming more components onto integrated circuits.," *Electronics*, vol. 38, Apr. 1965.

[13] "International technology roadmap for semiconductors website," *http://www.itrs.net/*.

[14] "Feeling the heat.," *Economist*, vol. 366, pp. 29–30, 2003.

[15] C. Biever, "Secret of 'strained silicon' chips revealed," *New Scientist*, Dec. 2003.

[16] F. Volkel, "Strip out the fans, add 8 gallons of cooking oil," *http://www.tomshardware.com/2006/01/09/strip_out_the_fans/*, 2006.

[17] "3m manufacturing and industry website: 3m fluorinert electronic liquids," *http://products3.3m.com/*.

[18] G. Solbrekken, K. Yazawa, and A. Bar-Cohen, "Chip level refrigeration of portable electronic equipment using thermoelectric devices," (Maui, Hawaii, USA), July 2003.

[19] A. Pfahnl and H.-S. Liang, "Liquid cooling high power compact electronics," in *Inter Society Conference on Thermal Phenomena*, 2004.

[20] F. Volkel and B. Topelt, "5 Ghz project: CPU cooling with liquid nitrogen," *http://www.tomshardware.com/2003/12/30/5_ghz_project/*, Dec. 2003.

[21] J. W. Vandersande, R. Ewell, J.-P. Fleurial, and H. B. Lyon, "Thermoelectric devices and diamond films for temperature control of high density electronic circuits,"

in *The thirteenth international conference on thermoelectrics*, vol. 316, (Kansas City, Missouri (USA)), pp. 174–176, AIP, 1994.

[22] C. Evans, V. D. Jovanovic, D. Indjin, Z. Ikonic, and P. Harrison, "Investigation of thermal effects in quantum-cascade lasers," *IEEE Journal of Quantum Electronics*, vol. 42, pp. 859–867, Sept. 2006.

[23] C. Kittel, *Introduction to Solid State Physics*. Wiley, 3rd ed ed., 1966.

[24] N. J. Pilgrim, *Electrothermal Monte Carlo Simulation of Semiconductor Devices*. 2003. Thesis (Ph. D.), University of Leeds, School of Electronic and Electrical Engineering.

[25] E. Pop, S. Sinha, and K. Goodson, "Monte Carlo modeling of heat generation in electronic," *Proceedings of IMECE02*, Nov. 2002.

[26] D. G. Cahill, W. K. Ford, and K. Goodson, "Nanoscale thermal transport," *Applied Physics Reviews*, vol. 93, p. 793, 2003.

[27] J. Radovanovic, V. Milanovic, Z. Ikonic, D. Indjin, and P. Harrison, "Electron-phonon relaxation rates and optical gain in a quantum cascade laser in a magnetic field," *Journal of Applied Physics*, vol. 97, p. 103109, 2005.

[28] S. Kumar, B. S. Williams, Q. Hu, and J. L. Reno, "1.9 Thz quantum-cascade lasers with one-well injector," *Applied Physics Letters*, vol. 88, p. 121123, 2006.

[29] N. W. Ashcroft and N. D. Mermin, *Solid State Physics*. New York: Holt, Rinehart and Winston, 1976.

[30] R. Orbach and L. A. Vredevoe, "The attenuation of high frequancy phonons at low temperatures," *Physics*, vol. 1, pp. 91–94, 1964.

[31] R. Peierls *Ann. Physik*, vol. 3, p. 1055, 1929.

[32] J. Callaway, "Model for lattice thermal conductivity at low temperatures," *Phys. Rev.*, vol. 113, pp. 1046–1051, Feb. 1959.

[33] P. G. Klemens *Solid State Physics*, vol. 7, 1958.

[34] P. G. Klemens, "Decay of high-frequency longitudinal phonons," *Journal of Applied Physics*, vol. 38, pp. 4573–4576, 1967.

[35] P. Carruthers, "Theory of thermal conductivity of solids at low temperatures," *Rev. Mod. Phys.*, vol. 33, p. 92, 1961.

[36] S. Mazumder and A. Majumdar, "Monte Carlo study of phonon transport in solid thin films including dispersion and polarization," *J. Heat Transfer*, vol. 123, p. 749, 2001.

[37] J. D. Chung, A. J. H. McGaughey, and M. Kaviany, "Role of phonon dispersion in lattice thermal conductivity modeling," *Journal of Heat Transfer*, vol. 126, pp. 376 380, June 2004.

[38] X. Lu and J. Chu, "Lattice thermal conductivity in a silicon nanowire with square cross section," *Journal of Applied Physics*, vol. 100, p. 014305, 2006.

[39] S. V. J. Narumanchi, J. Y. Murthy, and C. H. Amon, "Submicron heat transport model in silicon accounting for phonon dispersion and polarization," *Journal of Heat Transfer*, vol. 126, pp. 946–955, 2004.

[40] S. V. J. Narumanchi, J. Y. Murthy, and C. H. Amon, "Comparison of different phonon transport models for predicting heat conduction in silicon-on-insulator transistors," *Journal of Heat Transfer*, vol. 127, pp. 713–723, 2005.

[41] G. D. Mahan, *Many-particle Physics*. Physics of solids and liquids, New York: Plenum, 1981.

[42] G. Chen, "Particularities of heat conduction in nanostructures," *Journal of Nanoparticle Research*, vol. 2, pp. 199–204, June 2000.

[43] R. Berman, *Thermal Conduction in Solids.* Oxford studies in physics, Oxford: Clarendon Press, 1976.

[44] W. Jones and N. H. March, *Theoretical Solid State Physics.* Interscience monographs and texts in physics and astronomy, New York: Wiley-Interscience, 1973.

[45] G. Chen, "Heat transfer in micro- and nanoscale photonic devices," *Annual REview of heat Transfer*, vol. 7, pp. 1–57, 1996.

[46] P. G. Sverdrup, S. Sinha, M. Asheghi, S. Uma, and K. E. Goodson, "Measurement of ballistic phonon conduction near hotspots in silicon," *Applied Physics Letters*, vol. 78, pp. 3331–3333, 2001.

[47] G. P. Srivastava, *The Physics of Phonons.* Bristol: Hilger, 1990.

[48] F. I. Fedorov, *Theory of Elastic Waves in Crystals.* New York: Plenum Press, 1968.

[49] J. W. Tucker and V. W. Rampton, *Microwave Ultrasonics in Solid State Physics.* Amsterdam: North-Holland Pub. Co, 1972.

[50] M. Born and K. Huang, *Dynamical Theory of Crystal Lattices.* International series of monographs on physics, Clarendon Press, Oxford, 1954.

[51] R. A. H. Hamilton and J. E. Parrott, "The third-order elastic constants of quasi-isotropic materials," *J. Phys. C*, p. 829, 1968.

[52] P. N. Keating, "Theory of the third-order elastic constants of diamond-like crystals," *Phys. Rev.*, vol. 149, pp. 674–678, Sept. 1966.

[53] P. N. Keating, "Effect of invariance requirements on the elastic strain energy of crystals with application to the diamond structure," *Phys. Rev.*, vol. 145, pp. 637–645, May 1966.

[54] D. Vanderbilt, S. H. Taole, and S. Narasimhan, "Anharmonic elastic and phonon properties of si," *Phys. Rev. B*, vol. 40, pp. 5657–5668, Sept. 1989.

[55] F. D. Murnaghan, *Finite Deformation of an Elastic Solid.* Applied mathematics series, Wiley; Chapman & Hall, 1951.

[56] J. A. Reissland, *The Physics of Phonons.* Wiley-Interscience, Chichester, 1973.

[57] M. G. Holland, "Phonon scattering in semiconductors from thermal conductivity studies," *Phys. Rev.*, vol. 134, pp. A471–A480, Apr. 1964.

[58] C. L. Tien, A. Majumdar, and F. M. Gerner, *Microscale Energy Transport.* Washington, D.C: Taylor & Francis, 1998.

[59] J. Ziman, *Electrons and Phonons: The Theory of Transport Phenomena in Solids.* Oxford: Clarendon Press, 2001.

[60] I. Pomeranchuk, "On the thermal conductivity of dielectrics," *Phys. Rev.*, vol. 60, pp. 820–821, Dec. 1941.

[61] S. Tamura, "Spontaneous decay rates of la phonons in quasi-isotropic solids," *Phys. Rev. B*, vol. 31, pp. 2574–2577, Feb. 1985.

[62] D. von der Linde, J. Kuhl, and H. Klingenberg, "Raman scattering from nonequilibrium lo phonons with picosecond resolution," *Phys. Rev. Lett.*, vol. 44, pp. 1505–1508, June 1980.

[63] C. Herring, "Role of low-energy phonons in thermal conduction," *Phys. Rev.*, vol. 95, pp. 954–965, Aug. 1954.

[64] R. Peierls, *Quantum Theory of Solids.* International series of monographs on physics, Oxford: Clarendon P, 1955.

[65] R. E. Nettleton, "Foundations of the callaway theory of thermal conductivity," *Phys. Rev.*, vol. 132, pp. 2032–2038, Dec. 1963.

[66] A. J. H. McGaughey and M. Kaviany, "Quantitative validation of the boltzmann transport equation phonon thermal conductivity model under the single-mode relaxation time approximation," *Physical Review B (Condensed Matter and Materials Physics)*, vol. 69, p. 094303, 2004.

[67] S. ichiro Tamura, "Anomalously long lifetimes of high-energy surface acoustic phonons," *Phys. Rev. B*, vol. 30, pp. 610–617, July 1984.

[68] S. Tamura and H. J. Maris, "Temperature dependence of phonon lifetimes in dielectric crystals," *Phys. Rev. B*, vol. 51, pp. 2857–2863, Feb. 1995.

[69] J. P. Wolfe, *Imaging Phonons: Acoustic Wave Propagation in Solids.* New York: Cambridge University Press, 1998.

[70] J. Drabble and M. Gluyas, *Lattice Dynamics.* Oxford, Pergamon Press, 1966.

[71] P. Glasserman, *Monte Carlo Methods in Financial Engineering.* Springer, 1 ed., Aug. 2003.

[72] W. E. Back and L. C. Bell, "Monte Carlo simulation as tool for process reengineering," *Journal of Management in Engineering*, vol. 11, pp. 46–53, 1995.

[73] N. V. Peskov, "Microcomputer Monte Carlo simulations of iii-v semiconductor growth during molecular beam epitaxy," *Computer Physics Communications*, vol. 77, pp. 64–68, Sept. 1993.

[74] C. Jacoboni and P. Lugli, *The Monte Carlo Method for Semiconductor Device Simulation.* Springer, July 1990.

[75] T. Klitsner, J. E. VanCleve, H. E. Fischer, and R. O. Pohl, "Phonon radiative heat transfer and surface scattering," *Phys. Rev. B*, vol. 38, pp. 7576–7594, Oct. 1988.

[76] R. Peterson, "Direct simulation of phonon-mediated heat transfer in a debye crystal," *Journal of heat transfer*, vol. 116, pp. 815–822.

[77] D. Lacroix, K. Joulain, and D. Lemonnier, "Monte carlo transient phonon transport in silicon and germanium at nanoscales," *Physical Review B (Condensed Matter and Materials Physics)*, vol. 72, p. 064305, 2005.

[78] Y. Chen, D. Li, J. R. Lukes, and A. Majumdar, "Monte carlo simulation of silicon nanowire thermal conductivity," *Journal of Heat Transfer*, vol. 127, pp. 1129–1137, 2005.

[79] Y. Wu, J. Xiang, C. Yang, W. Lu, and C. M. Lieber, "Single-crystal metallic nanowires and metal/semiconductor nanowire heterostructures," *Letters to Nature*, vol. 430, pp. 61–66, July 2004.

[80] D. A. Dikin, X. Chen, W. Ding, G. Wagner, and R. S. Ruoff, "Resonance vibration of amorphous SiO_2 nanowires driven by mechanical or electrical field excitation," *Journal of Applied Physics*, vol. 93, pp. 226–230, 2003.

[81] D. Tománek and R. J. Enbody, *Science and Application of Nanotubes*. New York: Kluwer Academic/Plenum, 2000.

[82] K. Bullis, "Technology review: Nanowire transistors faster than silicon."

[83] Y. Cui and C. M. Lieber, "Functional nanoscale electronic devices assembled using silicon nanowire building blocks," *Science*, vol. 291, pp. 851–853, Feb. 2001.

[84] A. Ghetti and D. Rideau, "3d monte carlo device simulation of nanowire mosfets including quantum mechanical and strain effects," in *Simulation of Semiconductor Processes and Devices, 2006 International Conference on*, pp. 67–70, 2006.

[85] E. Pop and K. E. Goodson, "Thermal phenomena in nanoscale transistors," *Journal of Electronic Packaging*, vol. 128, pp. 102–108, June 2006.

[86] A. Salles, B. Estibals, and C. Alonso, "Electro-thermal study of nano-inductors for integrated low power converters," in *Circuits and Systems, 2004. ISCAS '04. Proceedings of the 2004 International Symposium on*, vol. 3, pp. III- 717-20 Vol.3, 2004.

[87] S. Volz, D. Lemonnier, and J.-B. Saulnier, "Clamped nanowire thermal conductivity based on phonon transport equation," *Nanoscale and Microscale Thermophysical Engineering*, vol. 5, pp. 191–207, July 2001.

[88] J. Zou and A. Balandin, "Phonon heat conduction in a semiconductor nanowire," *Journal of Applied Physics*, vol. 89, pp. 2932–2938, 2001.

[89] M. Asheghi, Y. K. Leung, S. S. Wong, and K. E. Goodson, "Phonon-boundary scattering in thin silicon layers," *Applied Physics Letters*, vol. 71, pp. 1798–1800, 1997.

[90] C. Kimmer, "Phonon scattering by molecular dynamics: Temperature dependence and effect of structural disorder," *APS Meeting Abstracts*, p. 40008, Mar. 2005.

[91] O. M. Mukdadi, S. K. Datta, and M. L. Dunn, "Acoustic-phonon dispersion in nanowires," *Journal of Applied Physics*, vol. 97, p. 074313, 2005.

[92] B. A. Auld, *Acoustic Fields and Waves in Solids*. New York: Wiley-Interscience, 1973.

[93] N. Bannov, V. Aristov, V. Mitin, and M. A. Stroscio, "Electron relaxation times due to the deformation-potential interaction of electrons with confined acoustic phonons in a free-standing quantum well," *Phys. Rev. B*, vol. 51, pp. 9930–9942, Apr. 1995.

[94] A. Svizhenko, A. Balandin, S. Bandyopadhyay, and M. A. Stroscio, "Electron interaction with confined acoustic phonons in quantum wires subjected to a magnetic field," *Phys. Rev. B*, vol. 57, pp. 4687–4693, Feb. 1998.

[95] S. Tamura, J. A. Shields, and J. P. Wolfe, "Lattice dynamics and elastic phonon scattering in silicon," *Phys. Rev. B*, vol. 44, pp. 3001–3011, Aug. 1991.

[96] Y.-J. Han and P. G. Klemens, "Anharmonic thermal resistivity of dielectric crystals at low temperatures," *Phys. Rev. B*, vol. 48, pp. 6033–6042, Sept. 1993.

[97] M. T. Dove, *Introduction to Lattice Dynamics.* Cambridge topics in mineral physics and chemistry, Cambridge: Cambridge University Press, 1993.

[98] W. Voigt, *Lehrbuch der kristallphysik (mit ausschluss der kristalloptik).* Leipzig, Berlin: B.G. Teubner, 1910.

[99] M. Matsumoto and T. Nishimura, "Mersenne twister: A 623-dimensionally equidistant uniform pseudorandom number generator," *ACM Trans. on Modelling and Computer Simulation*, vol. 8, pp. 3–30, 1998.